A measurement of the inclusive branching ratio for $b \to s\gamma$ with the ALEPH detector at LEP

Mark Ian Williams, *B.Sc.(Hons) M.Phil*

Lancaster University

September 1997

Thesis submitted in partial fulfillment of the requirements for the degree of Doctor of Philosophy.

No part of this thesis has been, or will be, submitted elsewhere.

Abstract

In a data sample of approximately four million hadronic Z^0 decays, recorded by the ALEPH detector during the years 1991 to 1995, the inclusive branching ratio for $b \to s\gamma$ is measured to be:

$$Br(b \to s\gamma) = (3.14 \pm 0.83 \pm 0.53) \times 10^{-4},$$

where the first error is statistical and the second error systematic. This decay rate is consistent with that expected from Standard Model penguin diagrams.

Contents

1 The Standard Model and $b \to s\gamma$ **1**

1.1 Introduction 1

1.2 The Universe as we know it 1

1.2.1 The building blocks 2

1.2.2 The forces four 3

1.2.3 Bigger things 4

1.2.4 Gauging the weight of the world 4

1.2.5 The Standard Model and beyond 5

1.3 The **B**s and the birds 7

1.3.1 B-physics 7

1.3.2 $b \to s\gamma$ penguin decays 12

2 The ALEPH experiment **16**

2.1 Introduction 16

2.2 The LEP collider 16

2.3 The ALEPH detector 17

2.3.1 Overview of ALEPH 18

2.3.2 Tracking 18

2.3.3 Calorimetry 24

2.3.4 Luminosity 28

2.4 Triggering 29

2.5 Data Acquisition and Event reconstruction 30

2.5.1 Data aquisition 30

2.5.2 Event reconstruction 32

2.5.3 Energy flow 33

2.5.4 Photon identification 33

2.6 Monte Carlo detector simulation 35

2.6.1 The method 35

2.6.2 Simulating physics 35

2.6.3 Simulating the detector 35

2.7 ALEPH data-sets 36

2.8 Summary 36

3 Monte Carlo penguins **37**

3.1 Introduction 37

3.2 Two types of penguins 37

3.2.1 Resonant penguins 38

3.2.2 Non-resonant penguins 39

3.3 Inclusive signal Monte Carlo. 46

3.4 Model dependency 46

4 Event preselection: bs and γs **49**

4.1 Introduction 49

4.2 Hadronic event selection 49

4.3 Candidate photon selection 50

4.4 $b\bar{b}$ event selection 51

4.4.1 Tagging $b\bar{b}$ events 51

4.4.2 Measuring track impact parameters in 3D 53

4.4.3 The 3D impact parameter tag 55

4.5 Summary of the event preselection 59

4.6 Efficiencies and acceptances 60

5 Penguin b hadron reconstruction **63**

5.1 Introduction 63

5.2 $b \to s\gamma$ decay products 63

5.3 Track mass assignments 64

5.4 $b \to s\gamma$ track probabilities 65

5.5 Jet building 66

5.6 Jet selection 68

5.7 Resolutions and reconstructed spectra 72

6 Measurement of $Br(b \to s\gamma)$ **80**

6.1 Introduction 80

6.2 Final event selection 80

6.2.1 The story so far 81

6.2.2 Moments analysis of ECAL clusters 81

6.2.3 Topological selection variables 85

6.2.4 Optimising cuts using Monte Carlo events 85

6.2.5 Final efficiencies and acceptances 88

6.3 The main sources of background 92

6.4 Multivariate fit 94

6.5 Results 99

6.6 Statistical and systematic errors 105

6.7 Stability of the $Br(b \to s\gamma)$ measurement . . . 108
6.8 Supporting evidence . . . 110
6.8.1 "The smoking gun" . . . 110
6.8.2 Exclusive channels . . . 111
6.9 Summary . . . 113

7 Summary and conclusions **114**
7.1 Summary of the $b \to s\gamma$ analysis . . . 114
7.2 Theoretical implications of the result . . . 115
7.3 Future developments . . . 115

A VDET monitoring software **117**
A.1 Introduction . . . 117
A.1.1 Penguins aside . . . 117
A.1.2 VDET . . . 117
A.1.3 The need for a new VDET . . . 118
A.2 Out with the old and in with the new . . . 118
A.2.1 VDET II . . . 118
A.3 ALEPH online monitoring software . . . 119
A.4 VDET online monitoring software . . . 120
A.4.1 VDMON . . . 120
A.4.2 VDANL . . . 123
A.4.3 VDHOT . . . 123

List of Figures

1.1 *An example of a Feynman diagram.* 9

1.2 *The electromagnetic* $b \to s\gamma$ *penguin diagram* 13

1.3 *Electromagnetic penguin diagrams beyond the Standard Model.* . . 15

2.1 *The LEP collider* 17

2.2 *The* ALEPH *detector* 19

2.3 *The original* VDET 20

2.4 *The* TPC *subdetector* 22

2.5 *The electromagnetic calorimeter.* 25

2.6 *The composition of a layer of the electromagnetic calorimeter.* . . 26

2.7 *The* ALEPH *data acquisition architecture.* 31

3.1 *The* M_{X_s} *mass peaks and the corresponding* $E^{\star}_{\gamma}$ *spectra for the four strange resonances produced by the* HVFL04 *penguin Monte Carlo.* 39

3.2 *The* M_{X_s} *and* $E^{\star}_{\gamma}$ *spectra for the five* $B_{u(d)} \to X_s\gamma$ *resonant penguin event samples generated with* HVFL05. 40

3.3 *The* M_{X_s} *and* $E^{\star}_{\gamma}$ *spectra for the five* $B_s \to X_s\gamma$ *resonant penguin event samples generated with* HVFL05. 41

3.4 *The* X_s *mass spectra and the resulting* $E^{\star}_{\gamma}$ *spectrum for the non-resonant penguin events generated with* HVFL05. 42

3.5 *The Ali-Greub inclusive $B \to X_s\gamma(g)$ photon spectrum for P_F = 265 MeV/c.* 44

3.6 *The Ali-Greub inclusive $B \to X_s\gamma(g)$ photon spectrum for three P_F values.* 44

3.7 *Reweighting non-resonant penguins.* 45

3.8 *The inclusive signal Monte Carlo X_s mass spectrum and corresponding $E^\star_\gamma$ spectrum.* 48

4.1 *The cosine of the polar angle of the thrust axis for all data events satisfying the* ALEPH *hadronic event selection and the impact parameter tag event selection.* 51

4.2 *The photon energy cut for candidate photons in hadronic events.* . . 52

4.3 *The cut to reduce the number of photons coming from π^0 mesons.* 53

4.4 *Schematic diagram of a b hadron decay.* 54

4.5 *The reconstruction of track impact parameters.* 56

4.6 *The signed impact parameter significance distribution for Monte Carlo simulated events.* 57

4.7 *The P^{opp}_{hem} distributions for background Monte Carlo photons.* . . . 59

5.1 *A schematic representation of a penguin event.* 64

5.2 *The $b \to s\gamma$ track probability distributions for charged tracks.* . . . 67

5.3 *Jet selection cuts.* 71

5.4 *Signal Monte Carlo reconstructed b hadron residual momentum distributions.* 73

5.5 *Signal Monte Carlo reconstructed b hadron residual polar angle distributions.* 74

5.6 *Signal Monte Carlo reconstructed b hadron residual azimuthal angle distributions.* 75

5.7 *Penguin b hadron resolutions.* 76

5.8 *Reconstructed* $b \to s\gamma$ $E^{\star}_{\gamma}$ *distributions.* 77

5.9 *Reconstructed* $b \to s\gamma$ M_{X_s} *distributions.* 78

5.10 *Reconstructed* $b \to s\gamma$ $E^{\star}_{\gamma}$ *resolutions.* 79

6.1 *An illustration of the difference between the energy distributions in electromagnetic clusters arising from photons and those from unresolved* π^0 *mesons.* 82

6.2 *The rms deviation along the major axis of the* ECAL *cluster energy distribution for each candidate photon in the standard (background) Monte Carlo which passes the cuts described in chapters* 4 *and* 5. . 84

6.3 *The final event selection cuts.* 87

6.4 *Comparing data and MC before the fit in each cut variable and fit variable.* 91

6.5 *The quantities used in the multivariate fit to separate signal events from FSR background.* 96

6.6 *The* $E^{\star}_{\gamma}$ *distributions in data and the standard background Monte Carlo — before the fit — for the first four, photon-enriched, sub-samples.* 97

6.7 *The* $E^{\star}_{\gamma}$ *distributions in data and the standard background Monte Carlo — before the fit — for the second set of four,* π^0*-enriched, sub-samples.* 98

6.8 *The* $E^{\star}_{\gamma}$ *distributions in data and the corrected background Monte Carlo — after the fit — for the first four, photon-enriched, sub-samples.* 101

6.9 *The* $E^{\star}_{\gamma}$ *distributions in data and the corrected background Monte Carlo — after the fit — for the second set of four,* π^0*-enriched, sub-samples.* 102

6.10 *A signal of* $b \to s\gamma$ *in* E^{*}_{γ}. 103

6.11 *Comparing data and Monte Carlo events after the fit in each cut variable and fit variable.* 104

6.12 *The stability of the branching ratio measurement.* 109

6.13 *The smoking gun plots.* 112

A.1 *The* ALEPH *online monitoring system* 120

A.2 *The* VDET II *shift page* 122

List of Tables

1.1 *Lepton classification* 2

1.2 *Quark classification* 3

3.1 *Inclusive signal Monte Carlo composition.* 47

4.1 *The numbers of $b \to s\gamma$ Monte Carlo events passing each stage of the event preselection.* 61

4.2 *The numbers of events in data and the background Monte Carlo passing each stage of the event preselection.* 62

5.1 *The numbers of $b \to s\gamma$ Monte Carlo events passing the jet selection.* 69

5.2 *The numbers of events in data and the background Monte Carlo passing the jet selection.* 70

6.1 *The numbers of $b \to s\gamma$ Monte Carlo events passing the final event selection.* 89

6.2 *The numbers of events in data and the background Monte Carlo passing the final event selection.* 90

6.3 *Defining the sub-samples for the multivariate fit.* 94

6.4 *Results of the four parameter fit to the data* 100

6.5 *Uncertainties on the $Br(b \to s\gamma)$ measurement.* 105

Where we came from

In a flash, with silent thunder, the void began to fill with wonders.

The violent dawn bore multitudes now desperate for their solitude
The simple things began to cool and deigned to form new unions
Hydrogen was quickly spawned, then the light came boldly forth.

Balanced once, the forces four, now conspired to do much more
Atoms burned to fuel the stars, which sought out others like themselves
Then in their explosive days they returned complex remains.

As time went on this rich debris was found in stellar nurseries.

One planet in position prime ripened as the fires died
An envelope of air to breathe and water making up the seas
Combined in time so there could be vibrant life in shades of green.

From the sea came things that walked, continually they changed their form.
Culminating nature's plan, proudly upright stood a man

And when the moon and he were full, he wondered where he came from.

Chapter 1

The Standard Model and $b \to s\gamma$

1.1 Introduction

This introductory chapter begins with a brief overview of the central ideas contained within our current theories of elementary particles — more detailed accounts may be found in [1, 2, 3]. The chapter then focuses upon the physics related to decays of the b quark, and, in particular, the physical process which is the subject of this thesis: the electromagnetic penguin decay $b \to s\gamma$. It then goes on to explain the motivation behind a search for this rare decay. Later chapters will detail the tools used by the author in this search and the results obtained.

1.2 The Universe as we know it

In the last 100 years, Man, through the diligence and genius of scientists the world over, has pieced together a consistent picture which successfully models the physics of the universe around us. Within this picture the universe is said to be made up of a combination of well defined, elementary particles which interact with one another through four fundamental forces. The theoretical framework for three of these forces in encapsulated in the 'Standard Model', while the fourth, gravity, is described by Einstein's theory of General Relativity. The two models have been amazingly successful at predicting all measurable physical effects from elementary particle interactions to black holes. Theorists, however, hope that one day they will have a single theory which explains all the forces of nature. Thus, a major aim of experimental particle physics is to find evidence of physics beyond the Standard Model which will aid theorists in their quest for a 'Theory of Everything'.

1.2.1 The building blocks

In the Standard Model, all matter in the 'universe as we know it' is made up of elementary particles, of which there are three types. There are two basic building blocks, called quarks and leptons, and the particles by which the building blocks interact, called mediators. There are six leptons (ℓ), classified according to their electric charge (Q), electron number (L_e), muon number (L_μ), and tau number (L_τ). They fall naturally into three families, or 'generations' — see table 1.1. There are also six antileptons, with all the signs reversed. The positron (e^+), for example, carries a charge of +1 and electron number −1. Hence there are really 12 leptons, all told.

	ℓ	Q	L_e	L_μ	L_τ
First generation	e	−1	1	0	0
	ν_e	0	1	0	0
Second generation	μ	−1	0	1	0
	ν_μ	0	0	1	0
Third generation	τ	−1	0	0	1
	ν_τ	0	0	0	1

Table 1.1: *Lepton classification*

Similarly, there are six 'flavours' of quarks (q), which are classified according to their charge, strangeness (S), charm (C), bottom (B), and top (T) numbers — see table 1.2. Again, all signs would be reversed in the table of antiquarks. Finally, to further complicate the matter, each quark and antiquark comes in three 'colours', so there are 36 of them in all.

	q	Q	S	C	B	T
First generation	d	$-1/3$	0	0	0	0
	u	$2/3$	0	0	0	0
Second generation	s	$-1/3$	-1	0	0	0
	c	$2/3$	0	1	0	0
Third generation	b	$-1/3$	0	0	-1	0
	t	$2/3$	0	0	0	1

Table 1.2: *Quark classification*

1.2.2 The forces four

There are four forces which govern the interactions between the 'building blocks' of the universe, and hence allow the complex clumps of matter we see around us to form. According to the Standard Model, three of these forces can be explained by the exchange of mediators between interacting quarks and/or leptons.

The Standard Model is based on Quantum Field Theory which combines quantum mechanics and special relativity, and is used to compute various physical quantities for comparison with experiment. A mediator is seen as a quantum of the field produced when two particles interact. The electromagnetic force between charged particles is viewed, according to the theory of Quantum Electrodynamics (QED), as the result of the electromagnetic field between them, which is mediated by photons (γ). The strong nuclear force between coloured quarks, described by Quantum Chromodynamics (QCD), is mediated by gluons (g), which, unlike photons, may also interact with one another. Finally, the weak nuclear force, by which, for example, lepton/quark flavours can decay to other lepton/quark flavours, is mediated by the intermediate vector bosons ($W^{\pm}$, and the Z^0). The electromagnetic and weak forces have been unified into one electroweak theory, but attempts to unify these with the strong force of QCD have yet to meet with success.

The force of gravity is negligible at the microscopic scales which particle physics experiments are built to examine, so it can be safely ignored when dealing with physical processes such as $b \to s\gamma$.

1.2.3 Bigger things

Progressively bigger, more complex things are made from elementary particles. The strong nuclear force 'glues' quarks together, forming bound states called hadrons. There are two types of hadrons: mesons, which are quark-antiquark pairs; and baryons in which quarks congregate in groups of three. The baryons most prevalent in nature are protons (uud) and neutrons (udd) which dominate the matter universe because heavy quarks decay to light quarks through the weak nuclear force. The protons and neutrons combine further to produce positively charged nuclei which in turn attract clouds of electrons through the electromagnetic force so creating atoms. The nuclei of heavy elements are manufactured within stars which are the work of gravity. Finally, chemical processes cause atoms to bond, forming solids, liquids, gases, and occasionally living things.

1.2.4 Gauging the weight of the world

Gauge theory

Certain physical quantities, such as charge, seem to be conserved everywhere in space-time. Now the presence of a symmetry in a physical system implies the existence of such a conserved quantity. The invariance of a system under spatial rotations, for example, leads to the conservation of rotational angular momentum. Thus, for a physical theory to truly describe a fundamental force of nature, its dynamics must originate from a symmetry. That is, the formulae describing the theory (in particular, the Lagrangian, which is essentially the difference between the kinetic energy and potential energy of the system) are unchanged under certain symmetry transformations, called 'gauge' transformations. In QED, for example, this "gauge invariance" results from the addition of an electromagnetic field to the Lagrangian describing the wave function of a charged particle. The symmetry requires the quantum of the field (the photon) to be massless and the physical manifestation of the symmetry is charge conservation.

The origin of mass

In the Standard Model there are further fields, called Higgs fields, which are believed to be responsible for the origin of mass. Without the addition of Higgs fields to the Lagrangian describing weak interactions, electroweak theory, with its massive intermediate vector bosons, would not be gauge invariant. However, the state of minimum energy introduced by these fields breaks the local gauge symmetry, generating masses for $W^{\pm}$ and Z^0 bosons, and giving rise to a single real, observable neutral Higgs boson (H). This Higgs boson couples to quarks and leptons with a strength proportional to their masses. Thus, the Higgs boson is fundamental to the Standard Model and a dedicated particle accelerator, the Large Hadron Collider (LHC), is currently being built to find it.

1.2.5 The Standard Model and beyond

The good, the bad, and the ugly

The Standard Model has been remarkably successful in accounting for all the phenomena observed in high energy physics experiments. There is as yet no irrefutable evidence that the theory is wrong or breaks down at any level. However, the model is unsatisfactory; it is very complex and leaves many questions unanswered. It fails to explain, for example, the quantisation of charge and why the charge on the electron is exactly opposite to the charge on the proton (and so an exact multiple of the $\frac{1}{3}$ charges on the quark). It includes 19 'free' parameters (such as charges, masses, and mixing angles) which have to be determined experimentally. It also fails to account for the strong resemblance between quarks and leptons; that both are seemingly point-like objects, arranged in three generations, with forces between them described by gauge theories. Furthermore, these gauge theories seem to predict that the strengths of the four forces of nature converge at high energies; that they are merely low-energy manifestations of a single grand unified force. A more compelling and beautiful theory would contain a unified description of quarks and leptons, and a unified formulation of the strong and electroweak interactions, reflecting the still deeper symmetries of nature.

In short, the Standard Model, though very successful, seems incomplete and frankly too ugly to be an ultimate theory of the microworld. For this reason, physicists are devising ever more stringent tests in an attempt to find experimental results which the model can not explain: The search is on for physics beyond the Standard Model.

Beyond the Standard Model

There are many competing theories waiting to usurp the Standard Model. One of the most attractive and promising theories is called 'supersymmetry'. Supersymmetry relates fermions (particles with half integer spin[1] such as quarks and leptons) to bosons (particles with integer spin such as the mediators described above). According to supersymmetry, every Standard Model particle has a companion particle — its 'superpartner' — different in spin by half a unit, but with otherwise identical couplings. Supersymmetric superpartners are usually denoted by a tilde ($\tilde{}$) above the appropriate symbol. Hence the spin-1 photon γ, for example, has a spin-$\frac{1}{2}$ superpartner called the photino, $\tilde{\gamma}$.

Supersymmetry is so attractive because if promoted to a local gauge symmetry, then the theory automatically incorporates general relativity. A further consequence of supersymmetry is the requirement of an extended spectrum of Higgs particles, including a charged Higgs. Other theories also require more than one Higgs particle.

[1]Spin, s, is a quantum number such that the intrinsic angular momentum possessed by a particle is given by $\sqrt{s(s+1)}\hbar$, where $\hbar = \mathrm{h}/2\pi$ and h represents Planck's constant (6.63×10^{-34} Js).

1.3 The Bs and the birds

The remainder of this chapter is devoted to the physics of b quarks and b hadrons, and, in particular, the electromagnetic penguin decay $b \to s\gamma$. More complete reviews of the subjects discussed below may be found in [4, 5, 6].

1.3.1 B-physics

Weak decays of the b quark

In the Standard Model a quark may decay to a lighter quark via the emission of a $W^{\pm}$ boson. Such a decay is called a flavour changing charged current. The mixing of flavours is expressed in terms of a 3×3 matrix, V_{CKM}, operating on the charge −e/3 quarks, d, s, and b. This operation is shown below, where the matrix elements are labelled by the quark flavours which they link:

$$\begin{pmatrix} d' \\ s' \\ b' \end{pmatrix} = \begin{pmatrix} V_{ud} & V_{us} & V_{ub} \\ V_{cd} & V_{cs} & V_{cb} \\ V_{td} & V_{ts} & V_{tb} \end{pmatrix} \begin{pmatrix} d \\ s \\ b \end{pmatrix}$$

The CKM matrix is named after its inventors, **K**obayashi and **M**askawa, who had built on the work of **C**abibbo. The nine individual V_{CKM} matrix elements are parameterised in terms of three angles and one phase in the Standard Model but the values for these four quantities have to be determined experimentally.

According to the Standard Model the CKM matrix is unitary which means there are no *direct* transitions between b quarks and s quarks so flavour changing *neutral* currents, through the emission of a Z^0 boson, are forbidden.

b hadrons

Measuring the V_{CKM} elements, or even quark masses, is not a straightforward task because, according to the standard theory of strong interactions (QCD), free quarks can never be observed. Quarks carry the colour quantum number, and

QCD suggests that only colourless states appear in nature so quarks are confined to exist only within colourless, composite hadrons. Thus, the phenomenology of hadronic weak decays is characterised by an intricate interplay between the weak and strong interactions, which has to be disentangled before any information about Standard Model parameters can be extracted.

When an energetic quark-antiquark pair is produced they will move apart but, due to QCD 'confinement', the quarks have to 'dress' themselves with other quarks to create observable meson or baryon states. These extra quarks are created in the colour force field between the primary quarks. If the energy of the primary quark is much larger than its mass, the quark pair creation can repeat many times resulting, ultimately, in 'jets' of hadrons, with the direction closely following the primary quark direction. This process is called *fragmentation or* hadronisation. The probability which describes what fraction $Z = E_{had}/E_{quark}$ of the primary quark energy is taken over by the hadron is called the quark fragmentation function. Now, for $b\bar{b}$ events, since the inertia of the heavy b quark is retained in the b hadron, the fragmentation function is expected to peak at high values of Z; that is: the resulting b hadron will carry a large fraction of the original b quark's energy.

Effective field theory

The Standard Model Lagrangian is formulated in terms of quark and gluon *fields*, whereas the physical hadrons are bound states of these degrees of freedom. The theoretical framework for describing weak decays of hadrons is the effective field theory for mass scales $\mu << M_W$, M_Z, and M_t. This framework brings in local operators which govern "effectively" the transitions in question. It is a generalisation of the Fermi theory of weak interactions as formulated by Feynman and Gell-Mann. Feynman diagrams are used to visualize all types of particle interactions, and, moreover, along with the "Feynman rules" are used to calculate the cross-sections for the processes. An example of a Feynman diagram is shown in figure 1.1 which illustrates the exchange of a W boson between a b and a c quark.

If QCD effects are ignored, the effect on the b quark may then be described — using the Feynman rules — by the simplest effective Hamiltonian operator:

$$H^0{}_{eff} = \frac{G_F}{\sqrt{2}} V_{cb} V_{cs}{}^* Q_2, \tag{1.1}$$

where G_F is the Fermi coupling constant; V_{cb} and V_{cs} are the relevant CKM matrix elements; and

$$Q_2 = (\bar{\psi}_c \gamma_\mu (1 - \gamma_5) \psi_b)(\bar{\psi}_s \gamma_\mu (1 - \gamma_5) \psi_c) \tag{1.2}$$

is a local operator representing the charged currents $b \to c$ and $c \to s$; where $\bar{\psi}_c$, ψ_b, $\bar{\psi}_s$ and ψ_c are four-component 'spinors' corresponding to the momenta $\vec{p}$ and energies E of the quarks; and γ_μ and γ_5 are the relevant Dirac matrices.

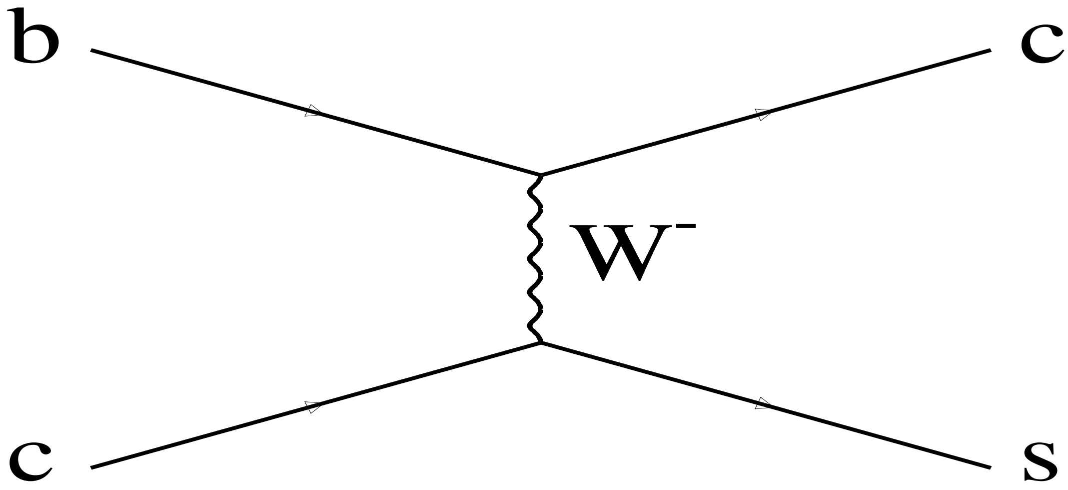

Figure 1.1: *An example of a Feynman diagram.*

The situation in the Standard Model is however complicated by the presence of additional interactions due to γ, g, Z^0 boson exchanges and internal top contributions which effectively generate new operators. Consequently the relevant effective Hamiltonian for B-meson decays involves several operators Q_i with various colour and Dirac structures which differ from that of Q_2. Moreover each operator is multiplied by a calculable coeficient $C_i(\mu)$ called a Wilson coefficient:

$$H_{eff} = \frac{G_F}{\sqrt{2}} V_{CKM} \sum_{i=1} C_i(\mu) Q_i, \tag{1.3}$$

Such an equation is an example of the Operator Product Expansion (OPE) technique used frequently in theoretical calculations. The Wilson coefficients describe the "effective" strength of the operators at a given mass scale μ. For B-physics the scale chosen is m_b, the mass of the b quark. The effective field theory relevant for B-physics is first formulated at a high energy mass scale $\mathcal{O}(M_W)$ and then the degrees of freedom heavier than the b quark are consecutively integrated out so they do not *explicitly* appear in the theory, but are 'hidden' within the effective gauge coupling constants, running masses, and, most importantly in the Wilson coefficients. This procedure is the essence of the renormalisation group approach, which, when combined with the OPE, allows the decay rates for processes to be calculated.

The amplitude for an exclusive decay $M \to F$ is written as:

$$A(M \to F) = \frac{G_F}{\sqrt{2}} V_{CKM} \sum_{i=1} C_i(\mu) < F|Q_i(\mu)|M >, \tag{1.4}$$

where M stands for the decaying meson, F for a given final state and V_{CKM} denotes the relevant CKM factor. $Q_i(\mu)$ denotes the local operator generated by QCD and electroweak interactions. The "short-distance" physics (corresponding to scales higher than μ) is contained in the Wilson coefficients $C_i(\mu)$ while the 'long-distance" physics (scales lower than μ) are contained in the matrix elements $< F|Q_i(\mu)|M >$. The $C_i(\mu)$ are calculated using the renormalisation group equations which govern the μ-dependence of these coefficients. However, the calculation of the matrix elements $< F|Q_i(\mu)|M >$ is more difficult as it requires the use of non-perturbative methods such as lattice QCD calcuations, QCD sum rules, or chiral perturbation theory. To calculate the full amplitude for a decay, the μ-dependence of $< Q_i(\mu) >$ has to cancel out that of the Wilson coefficients. Thus, the dominant theoretical uncertainties in the decay amplitudes reside in the matrix elements of Q_i.

Heavy quark symmetry

In the case of transitions between two heavy quarks, such as the semileptonic decay $b \to cl\nu$, heavy-quark symmetry helps to eliminate, or at least reduce, the hadronic uncertainties in the theoretical description. The physical picture underlying this symmetry is the following: In a heavy-light bound state such as a heavy meson or baryon, the typical momenta exchanged between the heavy and light constituents are of the order the confinement scale Λ. However, the fact that $1/m_Q << 1/\Lambda$, that is the Compton wavelength of the heavy quark, is much smaller than the size of the hadron, leads to simplification. To resolve the quantum numbers of the heavy quark would require a hard probe; soft gluons can only resolve distances much larger than $1/m_Q$. Therefore, the light degrees of freedom are blind to the flavour (mass) and spin of the heavy quark; they only experience its colour field, which extends over large distances because of confinement. It follows that, in the $m_Q \to \infty$ limit, hadronic systems which differ only in the flavour or spin quantum numbers of the heavy quark have the same configuration of their light degrees of freedom. This observation provides relations between the properties of such particles as the heavy mesons B, D, B^*, and D^*, or the heavy baryons Λ_b and Λ_c. These relations result from new symmetries of the effective strong interactions of heavy quarks at low energies. The configuration of light degrees of freedom in a hadron containing a single heavy quark with velocity v and spin s does not change if this quark is replaced by another quark with different flavour or spin, but with the same velocity. Most importantly, this symmetry relates all hadronic form factors in semileptonic decays of the B meson to a single universal form factor, the Isgur-Wise function. Heavy quark symmetry is an approximate symmetry, and corrections of order $\alpha_s(m_Q)$ or Λ/m_Q arise since the quark masses are not infinite. A systematic framework for analysing them is provided by the heavy quark effective theory (HQET).

The theoretical description of heavy-to-light ($b \to u$) decays is more model dependent than that for heavy-to-heavy ($b \to c$) transitions, because heavy-quark symmetry does not help to determine the relevant hadronic form factors. A variety of calculations for such form factors exist, based on QCD sum rules, lattice gauge theory, perturbative QCD or quark models.

Inclusive decay rates

Inclusive decay rates determine the probability of the decay of a particle into the sum of all possible final states with given quantum numbers. The theoretical framework to describe inclusive decays of heavy flavours is provided by the $1/m_Q$ expansion version of the OPE described above. The spectator model — where a free quark decay is assumed — has been shown to correspond to the leading order approximation in the $1/m_Q$ expansion. The starting point for inclusive decay rate calculations is again the effective Hamiltonian shown in equation 1.3, which includes the short distance QCD effects in $C_i(\mu)$. The actual decay described by the operators Q_i is then calculated using the spectator model corrected for additional virtual and real gluon corrections. The next corrections appear at the $\mathcal{O}(\Lambda/{m_Q}^2)$ level.

1.3.2 $b \to s\gamma$ penguin decays

Why "penguin"?

The Feynman diagram for the decay $b \to s\gamma$ reveals why one loop processes such as this are called penguins (see figure 1.2) [2]. A penguin process is defined as a "one loop flavour changing neutral current", where the flavour quantum number changes by one unit — that is ΔF = 1, unlike in box diagrams where ΔF = 2. Here, the b quark decays to an s quark through the emission and reabsorption of a $W^{\pm}$ boson, with the photon being emitted from any of the charged particles involved.

[2] The real reason why penguin diagrams are so named is recalled in [7]. It involved a game of darts between two theorists and a bet on the outcome. John Ellis of CERN lost the bet and had to put the word "penguin" into his next paper — in which this diagram first appeared.

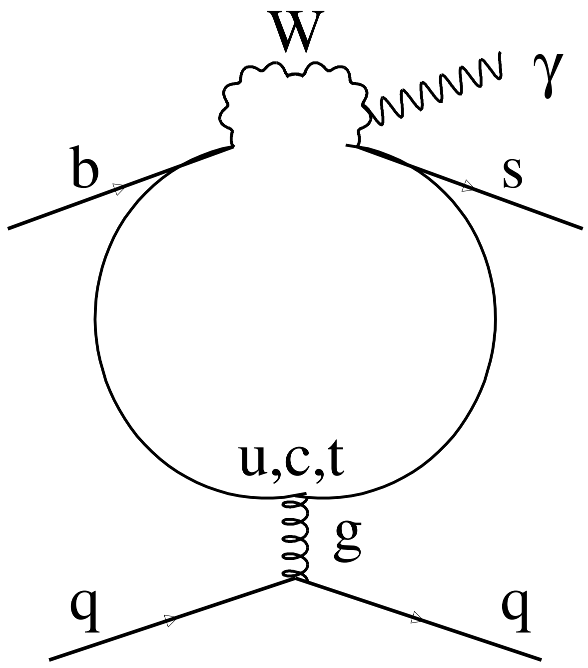

Figure 1.2: *The electromagnetic $b \rightarrow s\gamma$ penguin diagram: The photon may be emitted from any of the charged particles and the spectator quark (q) may exchange gluons with any other quark.*

The effective Hamiltonian describing this rare radiative decay at scales $\mu = \mathcal{O}(m_b)$ is given by:

$$H_{eff}(b \rightarrow s\gamma) = \frac{-4G_F}{\sqrt{2}} V_{ts}{}^{*} V_{tb} \left[\sum_{i=1}^{6} C_i(\mu) Q_i + C_7(\mu) Q_{7\gamma} + C_8(\mu) Q_{8G} \right] \quad (1.5)$$

where the term proportional to $V_{us}{}^{*}V_{ub}$ is neglected because $|V_{us}{}^{*}V_{ub}/V_{ts}{}^{*}V_{tb}|$ < 0.02 and the term proportional to $V_{cs}{}^{*}V_{cb}$ is included in the $V_{ts}{}^{*}V_{tb}$ term because of the Standard Model assumption of a unitary CKM matrix; that is $V_{us}{}^{*}V_{ub} + V_{cs}{}^{*}V_{cb} + V_{ts}{}^{*}V_{tb} = 1 \Rightarrow V_{cs}{}^{*}V_{cb} \simeq -V_{ts}{}^{*}V_{tb}$. The electromagnetic penguin loop is represented here by the operator $Q_{7\gamma}$, where:

$$Q_{7\gamma} = \frac{e}{8\pi^2} m_b \psi_s{}^{*} \sigma^{\mu\nu}(1+\gamma_5)\psi_b F_{\mu\nu} \quad (1.6)$$

in which, in the standard notation, $F_{\mu\nu}$ is the electromagnetic field tensor and $\sigma^{\mu\nu} = \frac{1}{2}[\gamma^\mu \gamma^\nu]$. The operator Q_{8G} represents the emission of a gluon along with the photon during the penguin decay and is defined along with the other operators and Wilson coefficients in [8].

Due to the large mass of the b quark, the properties of the electromagnetic penguin decay of a b hadron are mainly governed by the partonic $b \to s\gamma$ decay. Other quarks within the b hadron are referred to as a spectator quarks as they do not directly participate in the transition. They do however affect the decay indirectly; indeed the perturbative QCD effects involving, in particular, the operator Q_2 are very important in this decay. These effects are known to enhance the decay in the Standard Model by two to three times, depending on the top quark mass [9, 10]. It has taken a lot of work by a lot of theorists but now there is a practically complete next-to-leading order Standard Model prediction for the inclusive $b \to s\gamma$ branching ratio of $(3.28 \pm 0.33) \times 10^{-4}$ [8].

Why bother?

Electromagnetic penguin decays offer a unique window to probe new hypotheses beyond the Standard Model [11, 12]. The decay rate has great potential to reveal departures from the Standard Model because the loop diagrams could involve virtual particles, such as the Higgs, which cannot yet be produced on-shell. If the virtual particles in the loop of a penguin diagram were replaced by non-Standard Model particles, the decay rate could be enhanced or suppressed. For example, the W boson in the loop could be replaced by a charged Higgs, or SUSY particles could interfere with the process — see figure 1.3. Thus, any significant difference between a measurement of the inclusive $b \to s\gamma$ branching ratio and the Standard Model prediction would be evidence for new physics.

Picking up penguins

The $b \to s\gamma$ process behaves like a two-body decay so, in the b hadron rest frame, the radiated photon energy spectrum is peaked at approximately half the mass

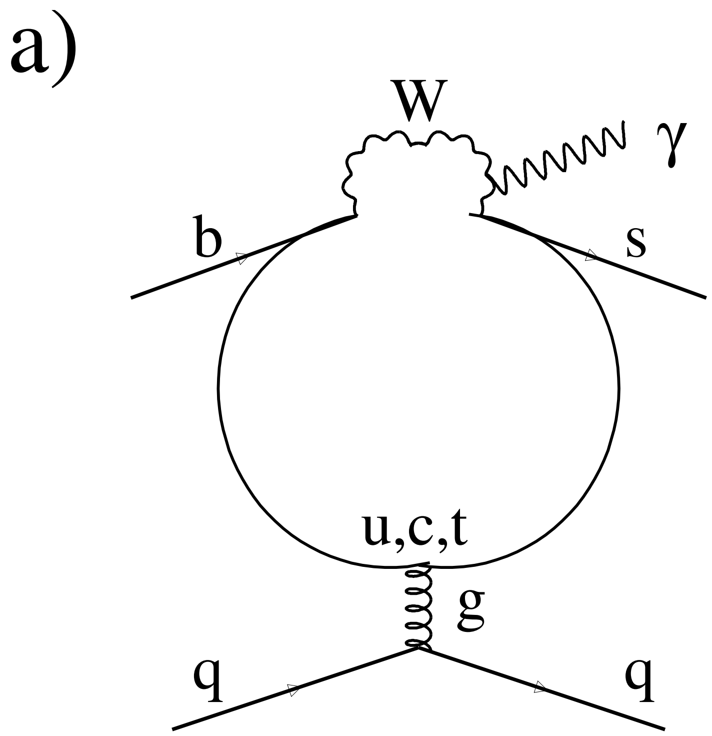

Figure 1.3: *Electromagnetic penguin diagrams beyond the Standard Model.*

of the b-hadron. In contrast, non-penguin radiative b decays such as $b \to c\gamma$ and $b \to u\gamma$ produce photons with a spectrum resembling that from bremsstrahlung and hence of much lower energy [13]. The decay $b \to d\gamma$ is also mediated by penguin diagrams but is expected to be a negligible source of background as the process is Cabbibo suppressed. The branching ratio for $b \to d\gamma$ is predicted to be $\leq 2.8 \times 10^{-5}$ [14]. Thus, $b \to s\gamma$ has a distinctive signature which makes a successful search for the decay possible. The first inclusive measurement of $Br(b \to s\gamma) = (2.32 \pm 0.57 \pm 0.35) \times 10^{-4}$, was made by the CLEO collaboration [15], who were also first to see exclusive penguin decays of B mesons[16]. Prior to the result presented in this thesis, two other LEP experiments, L3 [17] and DELPHI [18] had set upper limits on the $b \to s\gamma$ branching ratio of, respectively, $< 1.2 \times 10^{-3}$ and $< 5.4 \times 10^{-4}$ at 90% confidence level.

Chapter 2

The ALEPH experiment

2.1 Introduction

ALEPH is one of the four detectors built to record particles produced via high energy electron-positron collisions in the LEP storage ring at CERN. The data acquired by ALEPH is used to further knowledge of the Standard Model of particle physics, with the most accurate results coming from the electroweak sector. This involves a rigorous study of the myriad events in the data in order to test the theory's predictions and place constraints on the free parameters within the Standard Model.

2.2 The LEP collider

CERN's **L**arge **E**lectron-**P**ositron collider, LEP, is a 27 km circumference storage ring constructed inside a tunnel at an average depth of 100 metres at the foot of the Jura mountains near Geneva — see figure 2.1. Bunches of electrons and positrons are injected into the ring with an initial energy of 20 GeV and then accelerated in opposite directions using radio-frequency (RF) cavities. These bunches are steered around the ring using dipole bending magnets and are brought into collision at the four points on the ring where detectors are situated.

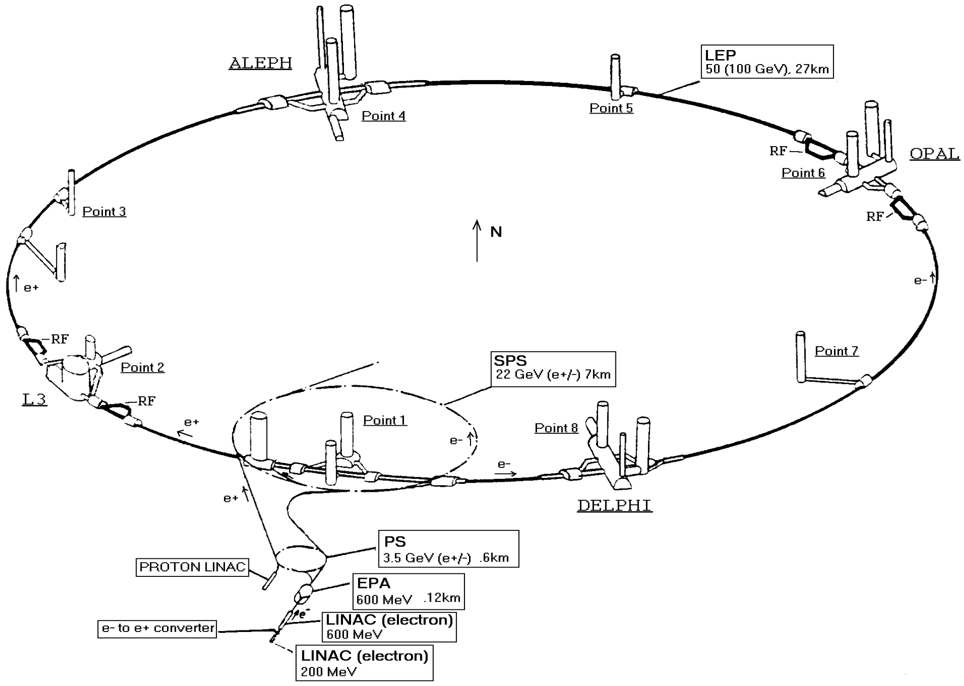

Figure 2.1: *The LEP collider*

LEP was built to enable physicists to make precise tests of electroweak physics. The first major phase of LEP operation began in 1989 and involved colliding beams at a centre-of-mass energy as close as possible to the Z^0 resonance — 45.6 GeV per beam. In the second phase, LEP 2, which began in 1996, the beam energies were increased in order to pair produce on-shell W bosons — around 80 GeV per beam.

2.3 The ALEPH detector

The ALEPH detector was designed, maintained and used by an international collaboration of more than 400 physicists representing over 30 institutions from

11 different nations. In this section an overview of the whole detector is followed by brief accounts of its component parts and how each part contributes data on LEP events which are then combined, assembled, and finally recorded for offline analyses. More complete descriptions may be found in [19, 20, 21, 22].

2.3.1 Overview of ALEPH

ALEPH (**A**pparatus for **LE**P **PH**ysics) was designed to measure as accurately as possible the nature, direction and energy of each particle created in the LEP electron-positron collisions which occur within the detector. The dimensions of the ALEPH detector are approximately $12 \times 12 \times 12$ metres and its mass is about 3000 tonnes. The detector is made up of independent modular subdetectors, arranged as a central cylindrical 'barrel' section closed by two 'endcaps', and covering almost 4π solid angle around the interaction point — see figure 2.2. There are three tracking subdetectors all contained within the barrel, with a shell of calorimetry subdetectors surrounding them.

2.3.2 Tracking

The silicon vertex detector

The innermost subdetector, which was used for data taking at the Z^0 resonance, is called VDET[1], the ALEPH silicon vertex detector [23]. VDET provides a high precision measurement of charged particle trajectories close to the interaction point and enables the identification of short-lived particles with typical decay lengths down to a few tenths of a millimetre. Two layers of silicon strip detectors are arranged in concentric barrels around the beam pipe with average radii of approximately 6.3 cm and 10.8 cm, and length 20 cm — see figure 2.3. The active detector solid angle coverage is 87% and 75% for the inner and outer layers respectively.

[1] VDET has now been replaced by an upgraded vertex detector, VDET II, which is discussed in appendix A.

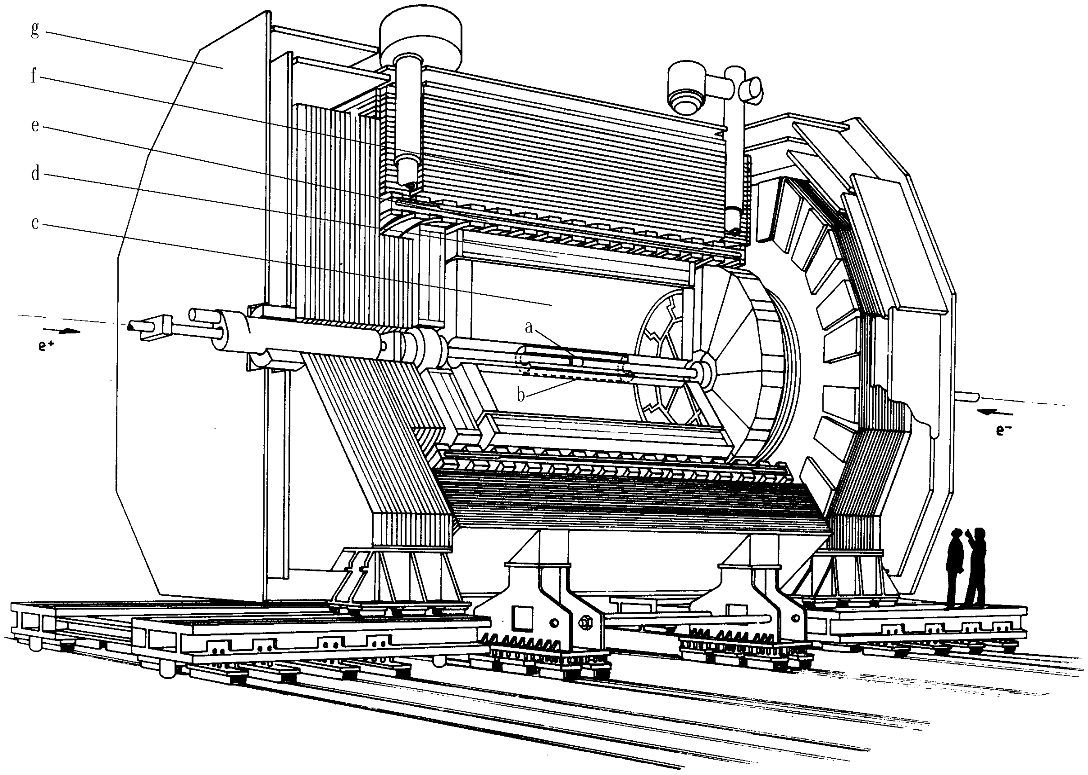

Figure 2.2: *The* ALEPH *detector: (a) silicon vertex detector (*VDET*); (b) inner tracking chamber (*ITC*); (c) time projection chamber (*TPC*); (d) electromagnetic calorimeter (*ECAL*); (e) superconducting solenoid; (f) hadron calorimeter (*HCAL*); and (g) the muon chambers. (Note that there are also luminosity calorimeters, which are situated close to the beam, but they are not labelled in this diagram.)*

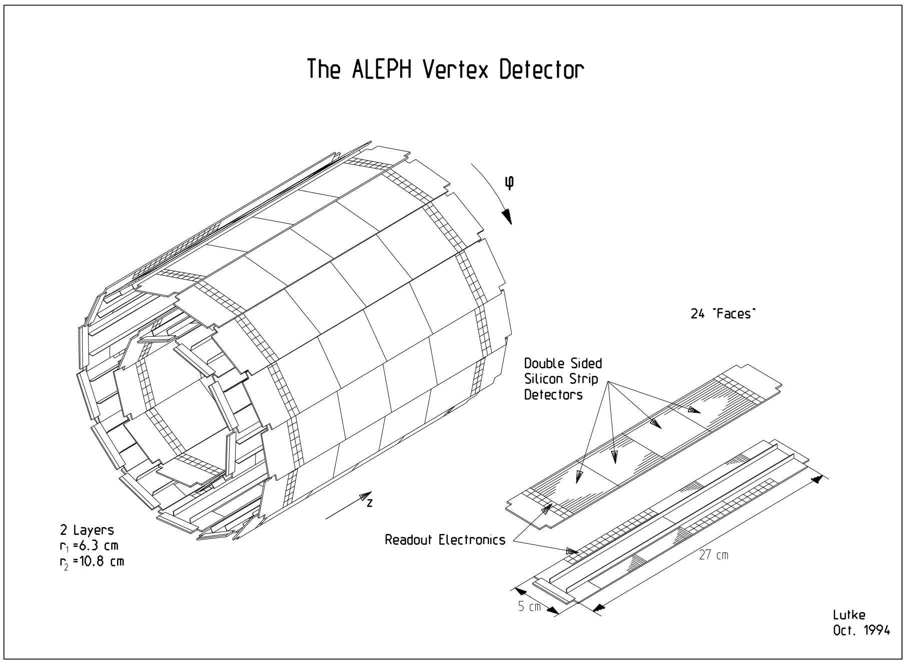

Figure 2.3: *The original* VDET

A total of 96 silicon wafers are used in VDET, 36 in the inner layer and 60 in the outer layer. The wafers have readout strips on both sides and are arranged in longitudinal groups of four, called 'faces'. The strips on one side are parallel to the beam direction and measure the azimuthal angle ϕ, while the strips on the other side are perpendicular to the beam and measure the z coordinate. With the radius r of the individual wafers given by the mechanical holding frame, the position of a single charged particle hit is measured in three dimensions (r,ϕ,z).

The point resolution of tracks at perpendicular incidence is found to be 12 μm in $r\phi$ and 10 μm in z. The addition of two very high precision VDET points onto the helix of a given charged track, measured using either or both of the other tracking subdetectors, improves the momentum resolution by about 25% from $\delta p/p = 8.8 \times 10^{-4}p$ to $\delta p/p = 6.6 \times 10^{-4}p$.

The inner tracking chamber

The inner tracking chamber, or ITC [24], is a cylindrical multiwire drift chamber with inner and outer radii of 128 and 285 mm, respectively, and length 2 metres.

It contains 960 sense wires, running parallel to the beam and strung between two aluminium endplates, each sense wire being surrounded by six field shaping wires in a hexagonal drift cell. The cells are organised into eight concentric layers; the four inner layers having 96 cells and the four outer layers having 144 cells. The cells are "close packed", meaning that cells in adjacent layers are shifted sideways by half a cell, resolving the left-right ambiguity which would otherwise be present in track reconstruction.

The $r\phi$ coordinates for a charged particle travelling through the ITC are obtained by measuring the drift times of the electrons it produces in the ITC gas mixture (Ar(80%) + CO_2(20%) at atmospheric pressure). An accuracy of about 150 μm is obtained in $r\phi$ (averaged over the drift cell). The z coordinate can also be obtained by measuring the time difference between opposite ends of a sense wire when both have registered an induced pulse. This gives an accuracy of about 70 mm when averaged over z and all layers.

As well as providing up to eight accurate $r\phi$ coordinates, it is the only tracking chamber used by the first level trigger as its fast readout allows a trigger decision to be reached within 1 μs of a beam crossing.

The time projection chamber

The time projection chamber [25], or TPC (see figure 2.4), is the largest tracking chamber in ALEPH and provides most of the charged track information. It is of cylindrical geometry, having an inner radius of 0.31 m, an outer radius of 1.8 m and a length of 4.7 m. The TPC is divided into two halves by a high voltage membrane of graphite coated mylar, at -27 kV, which lies in a plane perpendicular to the beam axis. At both ends of the TPC is an endplate, each connected to ground and containing 18 wire chambers, called sectors, arranged in a plane. The high voltage membrane and the grounded endplates give rise to an electric drift field of 155 V/cm which causes ionisation electrons to drift axially towards their nearest TPC sector. Coaxial with the beampipe are inner and outer field cage walls which use copper electrodes to ensure that the electric drift field in the volume between them is constant and parallel to the beam axis. The gas used in the TPC is Ar(91%) plus CH_4(9%) with a drift velocity of 5.2 cm/μs.

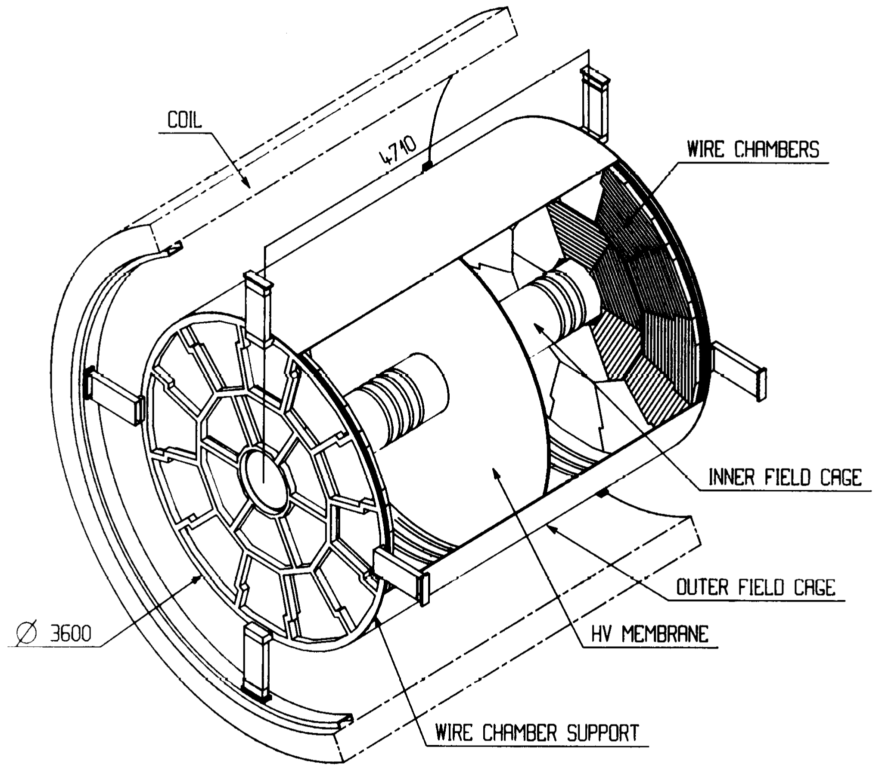

Figure 2.4: *The* TPC *subdetector: Note that the field "cages" should really be labelled "cage walls".*

Each TPC sector has three layers of wires which are the gating grid, cathode pad and sense wire plane respectively, with field shaping wires permeating through all three planes. The gating grid sets up a dipole electric field which is switched on 3 to 6 μs after a bunch crossing to stop any positive ions produced within the TPC sector from reentering the drift region and distorting the drift field. When an electron passes through the open gating grid and reaches the sense wire it causes an ionisation avalanche which induces a signal on the cathode pad, 4 mm beyond. There are 41004 pads in the TPC, each having dimensions 6.2 mm $\times$ 30 mm ($\delta(r\phi) \times \delta r$). The signal on the pad is read out for coordinate measurement and the pulses on the wires are used for measuring dE/dx, the ionisation energy loss. This information is used to separate charged electrons, muons, kaons, and pions.

The $r\phi$ coordinate of a drift electron is obtained by interpolating the signals induced on the cathode pads, whose positions are well known. The r coordinate is given by the radial position of the pad involved, and the z coordinate can be calculated if the drift field velocity is known ($\sim$ 5 cm/μs) and the drift time of the electron has been measured. There are 21 concentric pad rows so the TPC can measure 21 three dimensional points for charged particles crossing both inner and outer field cage walls. The resolution is dependent on the angles which the charged track makes with both the sense wires and the cathode pads. The $r\phi$ spatial resolution for a track with $0°$ pad crossing angle is 180 μm. The z coordinate can be obtained from either the pads or the wires if there are no other tracks crossing the sector. The z spatial resolution for the wires is 1.2 mm (with a slight z dependence) and 0.8 mm (for $\theta = 90°$) for the pads.

The superconducting solenoid

Surrounding the tracking subdetectors and the electromagnetic calorimeter is the ALEPH magnet which is vital for obtaining track momenta. The magnet is a superconducting solenoid which produces a field of 1.5 T in the z direction for a current of 5000 A. It is 7m long with inner and outer radii of 2.48 and 2.92 m. The iron return yoke of the solenoid is fully instrumented as the hadron calorimeter. The wire used is a niobium-titanium alloy and is operated at 4.3 Kelvin, at which temperature it is superconducting. The field occupies a volume of 123 m^3 and its z component is uniform to within 0.2%. The r and ϕ components of the magnetic field are less than 0.4 and 0.04% of the z component respectively.

Due to the solenoidal magnetic field, all charged particles follow a helical path. The projection of this three dimensional path onto the two dimensional endplate of the TPC produces an arc of a circle. Using the sagitta[2] of this arc it is possible to find the radius of curvature of the charged particle, which is proportional to the modulus of the track momentum component perpendicular to the magnetic field.

[2]The distance by which an arc diverges from a straight line.

The resolution of the transverse momentum p_t (GeV/c), Δp_t, is proportional to the resolution in the measurement of the sagitta, Δs (mm), that is:

$$\frac{\Delta p_t}{p_t} = 0.027 p_t \frac{\Delta s}{\ell^2 B}$$

where B is the modulus of the magnetic field and ℓ (m) is the length of the projected trajectory. The relative error on the measured momentum of a track arises from the error on the transverse momentum, as the error on the measurement of the polar angle, θ, is small. The momentum resolution, $\Delta p/p^2$, for a 45 GeV track traversing the full TPC radius is 1.2×10^{-3} (GeV/c)$^{-1}$ for the TPC only, 0.8×10^{-3} (GeV/c)$^{-1}$ for the ITC + TPC and 0.6×10^{-3} (GeV/c)$^{-1}$ for the ITC + TPC + VDET.

2.3.3 Calorimetry

The electromagnetic calorimeter

The ECAL (see fig. 2.5) surrounds the tracking chambers and consists of a barrel of length 4.77 m and inner and outer radii of 1.85 and 2.25 m, closed at either end by endcaps which have active inner and outer radii of 0.568 and 2.275 m and depth 0.411 m. The endcaps and barrel are subdivided into 12 modules, each subtending 30^0 in azimuth. The cracks between the modules, where no readout is possible, constitute 2% of the barrel surface and 6% of the endcap surface. To ensure that the cracks in the endcaps and the barrel are not coincident the endcap modules are rotated through 15^0 in azimuth. Further, to ensure that the cracks in ECAL and the hadron calorimeter are not aligned, the whole of ECAL is rotated by -1.875^0 in azimuth with respect to the hadron calorimeter. The mechanics and electronics for the endcap and barrel modules are as identical as possible.

The total energy of electromagnetic showers is measured in the ECAL using cathode pads of approximate dimensions 30×30 mm^2. These pads are connected together to give towers which point towards the interaction point and are read out in three sections, called storeys. A module consists of 45 layers of lead

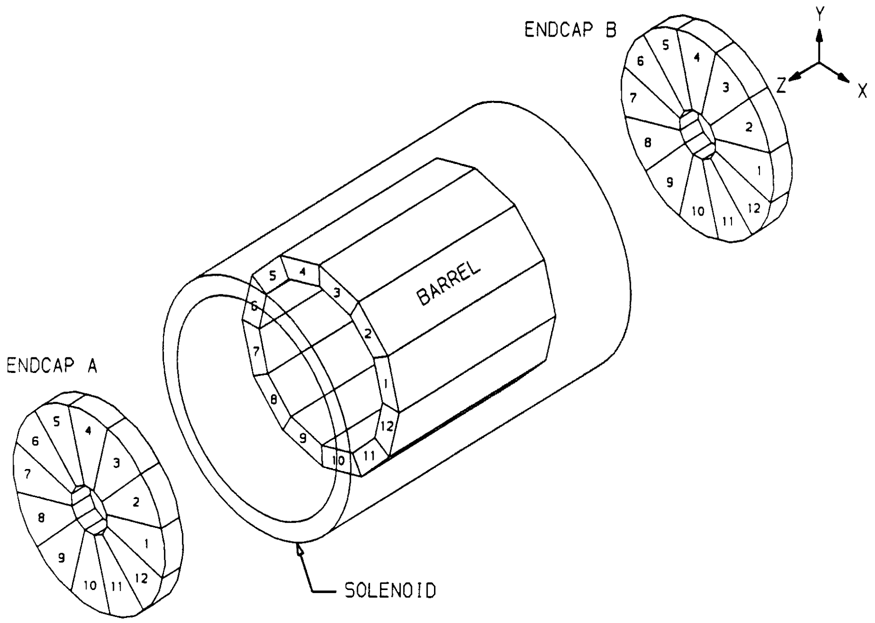

Figure 2.5: *The electromagnetic calorimeter.*

and proportional wire chambers, with the first storey ten layers thick (2 mm layers of lead giving 4 radiation lengths total), the second storey 23 layers (2 mm layers of lead giving 9 radiation lengths total) and the third storey 12 layers (4 mm layers of lead giving 9 radiation lengths total). The granularity of the pads allows the centroid of each shower to be located with angular resolution $\sigma_\phi = \sigma_\theta / sin\theta = 0.32 + 2.7/\sqrt{\mathrm{E(GeV)}}$ mrad, and the longitudinal development of the showers can be observed on the 45 wire layers providing good electron and photon identification. The energy resolution of the ECAL is parameterised as $\sigma/\mathrm{E} = 0.01 + 0.18/\sqrt{\mathrm{E(GeV)}}$.

The construction methods used result in a tower to tower uniformity of response within 1.6% (r.m.s.).

The wire chambers are built using an open sided aluminium extrusion. Anode wires sit inside channels on the open face of the extrusion and run parallel to the z axis. Below the extrusion is the cathode plane, which consists of the pads and readout lines. This ensemble is placed behind a highly resistive graphite coated mylar sheet and the resulting wire chamber is placed between two layers of lead sheet (fig. 2.6). Thus an electromagnetic shower, created by a particle travelling through the lead, will cause ionisation avalanches around the anode wires. This ionisation capacitively induces a signal on the cathode pads which is read out in storeys. The signals on each plane of wires are summed and also read out.

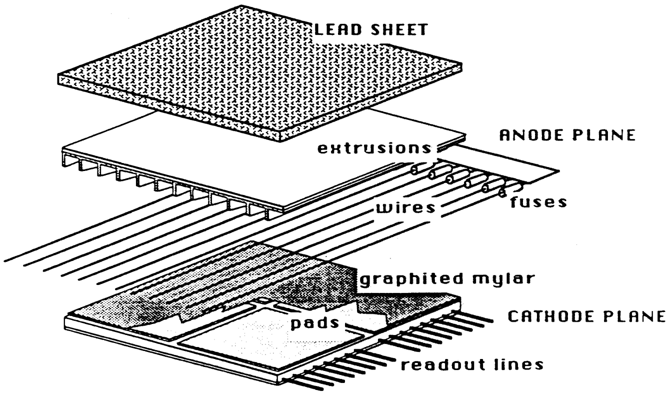

Figure 2.6: *The composition of a layer of the electromagnetic calorimeter.*

The gas used in the ECAL is Xe(80%)+CO_2(20%) and is about 60 mbar above atmospheric pressure.

The hadron calorimeter

The Hadron calorimeter, or HCAL, is the outer shell of calorimetry and provides information about particles that penetrate beyond the coil, that is most hadrons and muons. The iron structure providing the passive part of the calorimetry is also the main structural support for ALEPH and the return yoke for the magnetic field. The polar angle coverage is $6° < \theta < 174°$. As in the case of the electromagnetic calorimeter the hadron calorimeter has a barrel region which is closed at both ends by endcaps.

As for ECAL, the barrel is divided into twelve modules. The iron of each module is split into twenty two iron slabs, with spacers between each slab to allow insertion of limited streamer tubes which act as the active, or readout, part of the calorimeter. The total iron thickness is 1200 mm at $\theta = 90°$, which corresponds to 7.16 interaction lengths.

The streamer tubes are made from extruded plastic (PVC) with eight long cells of internal dimension 9×9 mm^2, and length 7 m. The inner surface of each cell is coated with graphite with a 100 μm thick wire running along its length, operating at 4 kV, and is used for triggering and electron avalanching. Opposite the open side of the cell are copper pads. The energy deposited in the pads from different layers are summed to form projective towers which subtend 3.7° in azimuth at the interaction point and have been designed so each tower has the same width in polar angle. The pattern of towers matches the pattern in the electromagnetic calorimeter, with about fourteen ECAL towers to one HCAL tower. On the opposite side of the cells to the pads is an aluminium strip which runs the length of the cell parallel to the wire. These provide a standard logic signal whenever an avalanche is induced on the wire and are used to obtain a two dimensional picture of hadronic showers and aid in muon identification.

The endcaps are divided into six modules each and are constructed in a similar way to the barrel. There are 2688 projective towers fully in the barrel, 2032 fully within the endcaps and 768 which are shared between the barrel and the endcaps. The gas used in the streamer tubes is Ar(12.5%) CO_2(56.5%) Isobutane(30%).

The hadron calorimeter has energy resolution σ_E/E of $84\%/\sqrt{E}$(GeV).

The muon chambers

Outside of the hadron calorimeter are two double layers of streamer tubes which cover 92% of the solid angle. They are used as tracking chambers and do not give information about the hadronic shower energy. They provide two-dimensional coordinates by having aluminium strip electrodes running both parallel and perpendicular to the wire in each cell of the tubes. The distance of separation between the double layers is 0.5 m for the barrel region and 0.4 m for the endcaps, which allows track directions for a particle travelling through both layers to be measured with an accuracy of about 10-15 mrad. Together with HCAL, the muon chambers are used to identify muons. For 95% efficiency, the probability of misidentifying hadrons as muons is about 1%.

2.3.4 Luminosity

The luminosity detectors

It is essential for certain accurate physics results that the error on the measurement of integrated luminosity received by ALEPH is small. Thus low angle elastic e^+e^- (Bhabha) scattering is used to measure the integrated luminosity as it is almost a pure QED process with very little interference from the weak sector, and has a well known cross section. The ALEPH luminosity monitors are designed to detect both the scattered electron and positron in coincidence on both sides of the interaction region with accurate polar angle measurements and good energy determination.

Since 1992 the luminosity in ALEPH has been measured using a silicon tungsten calorimeter, SICAL [26]. This consists of two cylindrical calorimeters situated about 2.5 m from, and either side of, the interaction region. The active inner and outer radii on both are 61 and 144 mm which corresponds to θ_{min} and θ_{max} of 24.3 and 57.7 mrad respectively. The detectors are constructed from 12 layers of tungsten sheets between which there are silicon layers, each with 512 readout pads. There are sixteen 5.2 mm radial pad-rows, each with a ϕ interval of 11.25^0. Consecutive layers of silicon are rotated through 3.75^0 in ϕ to eliminate azimuthal cracks. The energy resolution of SICAL is $\sigma_E/E = 23\%/\sqrt{E}(\mathrm{GeV})$. The SICAL was designed to produce a systematic uncertainty in the integrated luminosity measurement of less than 0.1%, and this has been improved to about 0.05% during operational running.

Before the installation of SICAL the luminosity calorimeter, or LCAL, measured luminosity. This is a sampling calorimeter based on the design of ECAL with 38 layers of lead sheets and wire chambers. It is made from four semicylindrical modules placed around the beam pipe 2.625 m from the interaction point. The systematic uncertainty in the integrated luminosity measurement due to LCAL was designed to be less than 2%, and during running an uncertainty of 0.4% was achieved.

Instantaneous luminosity is provided by the very small angle luminosity monitor, or BCAL. This consists of two opposing pairs of detectors placed at ± 7.7m from the interaction point and detects twenty times more Bhabha events than SICAL due to smaller polar angle detection.

2.4 Triggering

ALEPH employs a three level triggering system in order to separate genuine e^+e^- interactions from background; to reduce the frequency of accepted events to a rate which can be written to tape (about 1-2 Hz); and to reduce the dead time of the detector. The background events are mainly from three sources: beam-gas interactions arising from an imperfect vacuum in the beam pipe; off-momentum particles from the beam hitting either the collimators or the vacuum pipe close to ALEPH; and cosmic rays. The luminosity received by ALEPH is not high enough for there to be a need to select areas of physics on which to trigger once backgrounds have been eliminated. The trigger has been designed to be sensitive to single particles or single jets.

The level one trigger decides whether or not to initiate digitization of the event. A level one 'yes' will result if any level one trigger is satisfied. The principal level one triggers in ALEPH are as follows:

- ECAL energy greater than 6.5 GeV in the barrel or 3.8 GeV in either endcap or greater than 1.6 GeV in both endcaps in coincidence ; or
- ECAL energy greater than 1.3 GeV in a module in the same azimuthal region as an ITC track ; or
- a particle penetrating HCAL in the same azimuthal region as an ITC track.

A number of subsidiary triggers provide high redundancy and allow trigger efficiencies to be precisely determined.

Level two serves only to verify a level one trigger by replacing ITC tracking information with more accurate TPC information which is available 50 μs after the beam crossing. A level two 'yes' initiates full readout of the detector.

The level three trigger involves software analysis of the full detector readout and is used to reject background events. Very loose criteria are applied to ensure that all physics events are saved for analysis. The efficiency of the trigger is 100% for hadronic Z^0 decays, $\sim 100\,\%$ for charged leptonic Z^0 decays and $99.7 \pm 0.2\%$ for Bhabha events.

2.5 Data Acquisition and Event reconstruction

2.5.1 Data aquisition

The subdetectors in ALEPH are designed to be largely autonomous with respect to data aquisition. This requirement arose from the need to test and calibrate the individual subdetector modules during construction and commissioning of ALEPH. To this end a tree-like hierarchy was adopted (see figure 2.7).

The task of each element at each level of the hierarchy is as follows :

- **Read out controllers**. Once triggered, the ROCs read out the subdetector specific 'front-end' electronics, apply calibration procedures if required, and format the data.
- **Event builders** The EBs receive data from the ROCs and build a sub-event at subdetector level.
- **Main event builder**. The MEB combines the sub-events from the various EBs and forms the complete event.
- **ALEPH event processor**. The AEP (level 3 trigger) performs data reduction on the complete event.

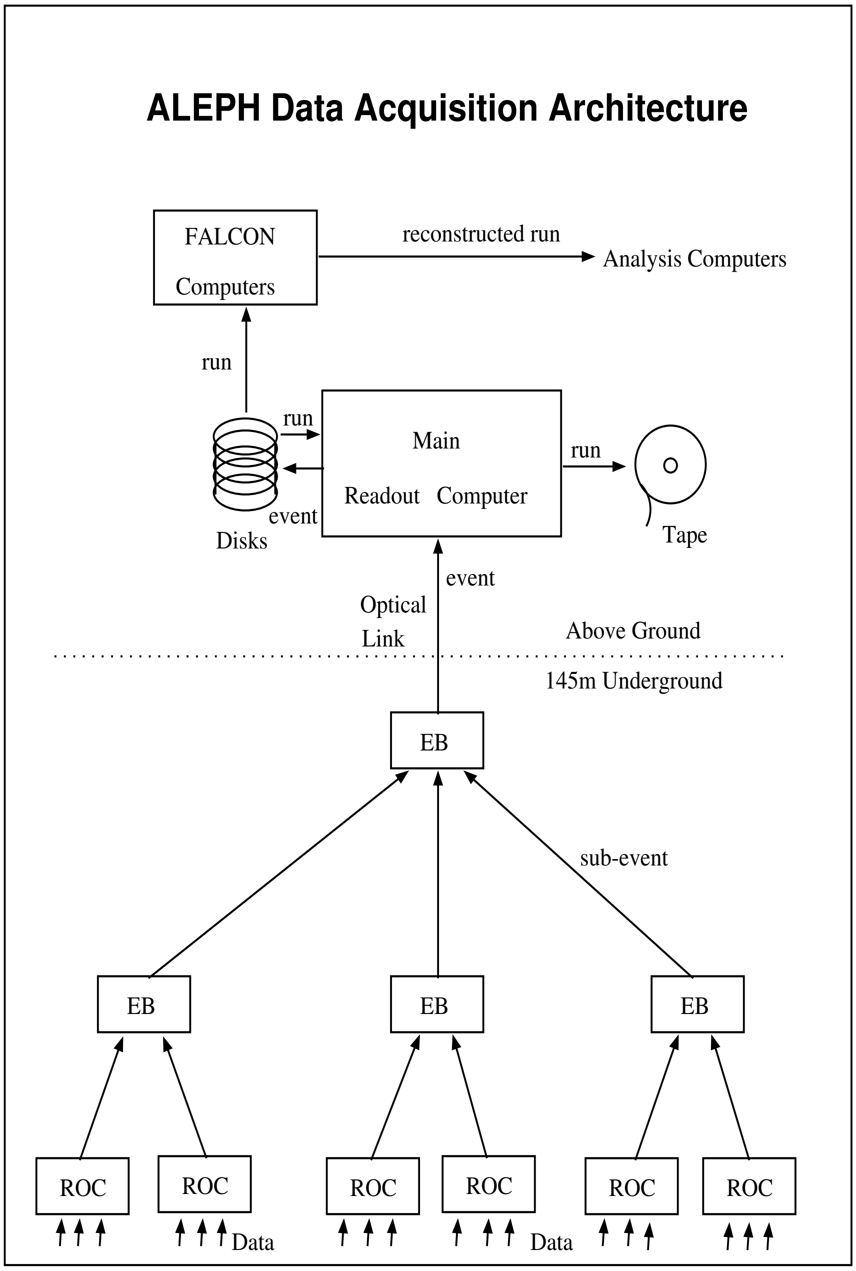

Figure 2.7: *The* ALEPH *data acquisition architecture: This is a simplified picture as there are almost 50 ROCs (Read Out Controllers) and EBs (Event Builders) in* ALEPH.

- **Host**. The host computer stores the data on disk and provides facilities for on-line event display and detector performance monitoring.
- **FALCON**. The event reconstruction in ALEPH is done 'quasi-online' by FALCON — a dedicated facility which then outputs the reconstructed event to the main CERN computer centre for storage and offline analysis.

2.5.2 Event reconstruction

The event reconstruction performed by FALCON is the process by which the digital signals from the subdetectors in ALEPH are converted into objects which can be used in physics studies. The two types of objects found are tracks, using the three tracking chambers, and calorimeter clusters.

The method to find tracks starts by using TPC information. Neighbouring hits in the TPC are connected together to form track segments. These segments are joined together if the result is consistent with a helical track hypothesis. The resulting tracks are extrapolated inwards to the other two tracking chambers where appropriate hits are assigned to the tracks. The resulting preliminary tracks are used as inputs to an accurate track fitting procedure, which uses the errors determined from the preliminary track parameters and takes into account multiple scattering.

Clusters are found in both ECAL and HCAL by the following method. All storeys which have an energy deposition greater than 30 MeV, and are connected by a minimum of a storey edge or corner, are collected together and called clusters. In the electromagnetic calorimeter, corrections are made to a cluster's energy to allow for storey threshold effects, ionisation losses for charged particles in the tracking detectors, leakage of electromagnetic showers which punch through ECAL and penetrate HCAL, and the non-linearity of calorimeter response which was found in test beam results.

2.5.3 Energy flow

The energy resolution of an event can be improved by using an energy flow algorithm [22]. This method links charged tracks to calorimeter objects and uses the redundancy in energy measurements that results to assign neutral particle energy. It also uses particle identification methods.

The method begins by considering all charged tracks found in the reconstruction. It produces a subset of good tracks which require at least four TPC hits (if the track has momentum greater than 15 GeV/c then it requires at least 8 TPC hits and 1 ITC hit) and which must originate from a cylinder of length 200 mm and radius 20 mm which is coaxial with the beams and centered on the interaction point. This will exclude all V0 candidates so these are searched for and reinstated. When dealing with the calorimeter objects, known noisy channels are masked out from the cluster finding and the readout redundancy in both calorimeters is exploited to smooth out occasional noise.

The next stage is to associate good charged tracks with calorimeter objects. All good charged tracks are called charged energy and they are assumed to be pions unless they have already been identified. Electrons, muons, photons and π^0s which have been identified are removed from the lists taking the appropriate energy from the associated calorimeter object. This should leave only charged and neutral hadrons. Lastly the energy of the tracks is subtracted from the calorimeter objects, and if the remainder is larger than 500 MeV it is attributed to neutral hadrons.

This algorithm enables a relative energy resolution of less than 9% to be obtained regardless of the energies involved.

2.5.4 Photon identification

The analysis presented in this thesis relies heavily on having good photon reconstruction. The three dimensional segmentation of ECAL ensures good photon resolution is possible up to the highest LEP energies available. However, a photon identification package is required because the clustering algorithm in the event reconstruction tends to build clusters which are too large and contain more than one photon. The photon identification package used by ALEPH was first introduced in 1992 but has since been developed and improved. It uses the GAMPEX [27] photon algorithm which starts by considering the clusters found in the event reconstruction but uses the assumptions that electromagnetic showers tend to begin in the first segment in depth of ECAL and that photon clusters are very compact.

The method used to identify candidate photons starts by looping over, in decreasing energy, the ECAL clusters found by the reconstruction algorithm. Firstly the inner layer of the towers is searched for all possible photon cluster seeds, that is a storey without a more energetic neighbour. Following this the other storeys are added to the appropriate seeds to make clusters; the outer layers being added sequentially. This method takes advantage of the compactness of electromagnetic clusters and the good projective geometry of ECAL. Finally, a new cluster is declared a "candidate photon" if its energy is greater than 0.25 GeV and no charged track is within 20 mm of the energy weighted mean centre of the cluster.

The position of the photon impact point is given by correcting the cluster barycentre to allow for the finite size of the calorimeter cells. The photon energy calculation uses the four central towers of the cluster and the expected value of the fraction of energy in the four towers, F_4. This fraction has been obtained by parameterising the shower shape for a single photon in ECAL. The effects of the calorimeter pad area, the distance between the photon impact and nearest tower corner and the variation with energy of F_4 are all included in the photon energy calculation.

The spatial resolution obtained is $\sigma_{\theta\phi} = (2.5/\sqrt{E(\mathrm{GeV})} + 0.25)$ mrad and the energy resolution $\sigma_E/E = 0.25/\sqrt{E}$. The energy resolution is worse than the expected $0.18/\sqrt{E}$ since only the four central towers of the cluster are used.

2.6 Monte Carlo detector simulation

2.6.1 The method

Most particle physics analyses involve stringent event selection criteria, homing in on a particular region of phase space in which the particular process under study is dominant. Monte Carlo methods are used to generate simulated events with the same structure as experimental data events so an analysis can be applied transparently to both. The generation of Monte Carlo events is a two stage process involving the simulation of physical processes and the effects of passing these pure events through an imperfect detector.

2.6.2 Simulating physics

All Monte Carlo simulated events referred to in this thesis were produced using a physics generator called *HVFL*. This generator is based on `JETSET` [28] with the modification that $e^+e^- \to q\bar{q}$ are generated using `DYMU3` [29], which includes an improved treatment of initial state radiation. Furthermore, certain inclusive and exclusive charmed and bottom hadron decays are modified to reflect recent experimental observation. Final state gluon and photon radiation, however, are simulated in `JETSET`.

2.6.3 Simulating the detector

The second stage is to simulate the passage of the generated particles through the detector, taking into account particle lifetimes and decays. The method used is based on the `GEANT/GHEISHA` approach [30], producing an output which has the same structure as the data. Tracking and calorimetry shower simulation are done in the `GEANT` framework. 'Hits' are produced in tracks in the tracking detectors, smeared by the appropriate resolution and used to produce 'raw data' containing the same information as real events. Showers in calorimeters are developed using `GEANT` tables and algorithms, but electron and positron showers are modelled using parameterisations established from test beam data.

2.7 ALEPH data-sets

The complete ALEPH detector acquired data at the Z^0 resonance during the years 1991 to 1995, collecting over 4 million Z^0 events. At the time of writing, almost 9 million $q\bar{q}$ Monte Carlo events have been generated for analysis and comparison with the data.

Three sets of Monte Carlo $q\bar{q}$ events are used in the analysis described in this thesis. The three sets of events use simulations of the detector geometry corresponding to the years 1992, 1993, and 1994, and three versions of the HVFL generator — HVFL03, HVFL04, and HVFL05 respectively. The important details to note, as far as this thesis is concerned, are the following:

- HVFL03 and HVFL04 use `JETSET 7.3` while HVFL05 uses `JETSET 7.4`.
- The branching ratio and particle mass measurements — along with certain `JETSET` parameters — are updated for each HVFL version. The mass of the top quark, for example, was set at 100 GeV/c^2 for HVFL03 and HVFL04 before it was measured, but HVFL05 uses the then central value for the measured top mass of 182 GeV/c^2.

2.8 Summary

The ALEPH detector is a good all round performer in the field of e^+e^- physics. The tracking detectors provide good momentum and impact parameter resolution which is important for the reconstruction of b hadrons and for tagging $b\bar{b}$ events. The calorimetry is also good and enables photons to be identified and their energies to be measured with good resolution. These features of the detector enable successful searches for rare decays of the b quark to be carried out.

Chapter 3

Monte Carlo penguins

3.1 Introduction

The first stage in the inclusive search for $b \to s\gamma$ was the Monte Carlo simulation of penguin events as they would appear in the ALEPH detector. These simulated signal events could then be compared with background Monte Carlo $q\bar{q}$ events and used in the search for real penguins in the ALEPH data. A theoretical model was used for the relative fractions of *exclusive* decay channels by which $b \to s\gamma$ occurs. An *inclusive* $b \to s\gamma$ Monte Carlo was thence assembled by adding up the most common exclusive channels according to this model.

3.2 Two types of penguins

There are effectively two types of $b \to s\gamma$ events depending on whether or not a gluon is radiated along with the photon in the decay. If there is no gluon radiated the b hadron decays into two bodies: a strange resonant state (an s hadron) and a photon. However, if a gluon is radiated there will be a continuum of possible strange states, X_s, along with the photons, with no resonant states being favoured. For this reason, two sets of fully reconstructed Monte Carlo penguin events were generated, one of each type.

Signal Monte Carlo $b\bar{b}$ events, where one b decays normally while the other b decays to $s\gamma(g)$, were generated using HVFL04 and HVFL05. The details of ALEPH Monte Carlo event generation were discussed in chapter 2.

3.2.1 Resonant penguins

Initially, 29490 fully reconstructed Monte Carlo two-body $B \rightarrow X_s\gamma$ events, where the X_s is some meson containing a strange quark, were generated using HVFL04. In these events, one of the primary b quark pair decays 'normally' while the other decays as a two-body mesonic penguin. The penguin-decaying B-meson can be a B_s, B_d or B_u with four different X_s meson resonance states being produced in the following fractions: K^*(44.8%); ${K_2}^*$(44.3%); ϕ(5.5%); and f_2'(5.4%).[1] Their distribution in $E^\star_\gamma$, the photon energy in the b hadron rest frame, is shown in figure 3.1, which directly corresponds to their X_s mass spectra. The relationship between $E^\star_\gamma$ and M_{X_s}, the mass of the s hadron (in the resonant case), is given below, where M_B is the mass of the b hadron.

$$E^\star_\gamma = (M_B^2 - M_{X_s}^2)/2M_B \tag{3.1}$$

The HVFL04 penguin events were used in the initial development of the analysis which follows, but more resonant penguins, with a larger variety of exclusive decay channels, were generated subsequently with HVFL05. Approximately 2500 events were generated for each of five B_d penguin decay channels, and also for the corresponding five B_u penguin decay channels, while approximately 600 events were generated for each of the five main B_s channels — see figures 3.2 and 3.3. Baryonic penguins, which have yet to concern theorists, were modelled by one channel only: $\Lambda_b \rightarrow \Lambda(1116)\gamma$, where the Λ_b is produced directly from hadronisation or from the decay of a heavier b baryon. The Λ_b and $\Lambda(1116)$ are assumed to have no mass width in the Monte Carlo events so, for the baryonic penguins, $E^\star_\gamma = (5.616^2 - 1.116^2)/(2 \times 5.616) = 2.697$ GeV.

[1] $B \rightarrow K\gamma$ events were not simulated because this decay is a forbidden process which would not conserve angular momentum.

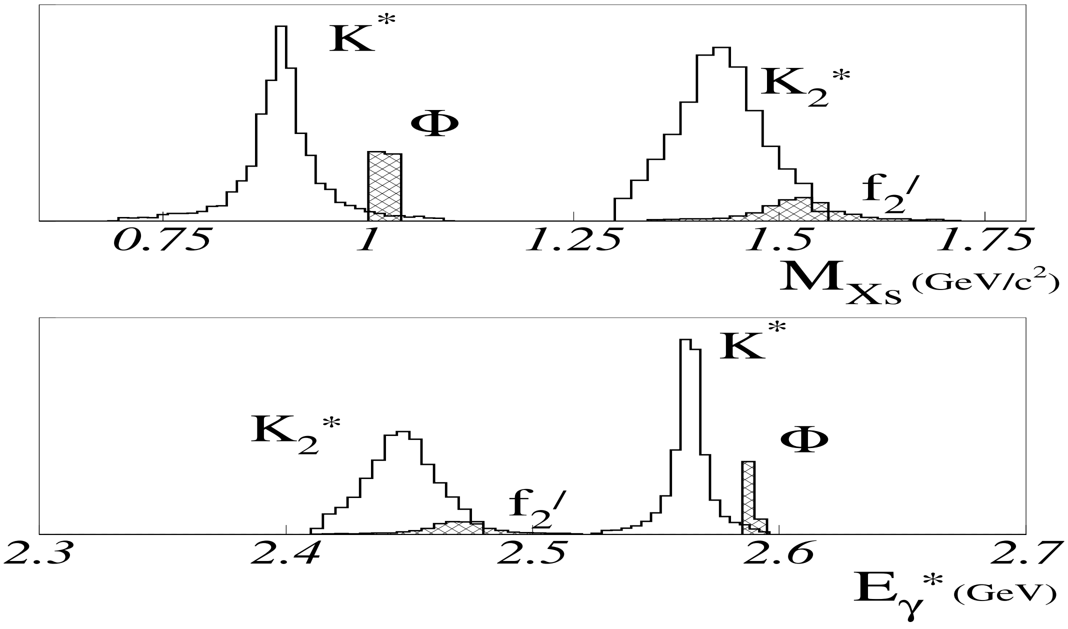

Figure 3.1: *The M_{X_s} mass peaks and the corresponding $E^\star_\gamma$ spectra for the four strange resonances produced by the* HVFL04 *penguin Monte Carlo.*

3.2.2 Non-resonant penguins

10248 non-resonant $B \to X_s\gamma$ penguin events were generated with HVFL05, based on a parameterisation of the inclusive $B \to X_s\gamma(g)$ photon spectrum predicted by Ali and Greub [32], which corresponds to a true continuum of X_s masses. In these events, the B can be B_s, B_d or B_u and again only one of the $b\bar{b}$ pair decays in a penguin fashion. The mass of the strange X_s non-resonant state is chosen from a Gaussian distribution (roughly reproducing the Ali-Greub spectrum) with asymmetric cuts, and is hadronised by `JETSET` [28] according to the quark content. Thus, in these events, there is no explicit strange resonance, and X_s is some multi-body state involving one or two kaons and n pions. The continuum X_s mass spectrum means there can be no visible structure in the $E^\star_\gamma$ spectrum for such events, even with a perfect detector — see figure 3.4.

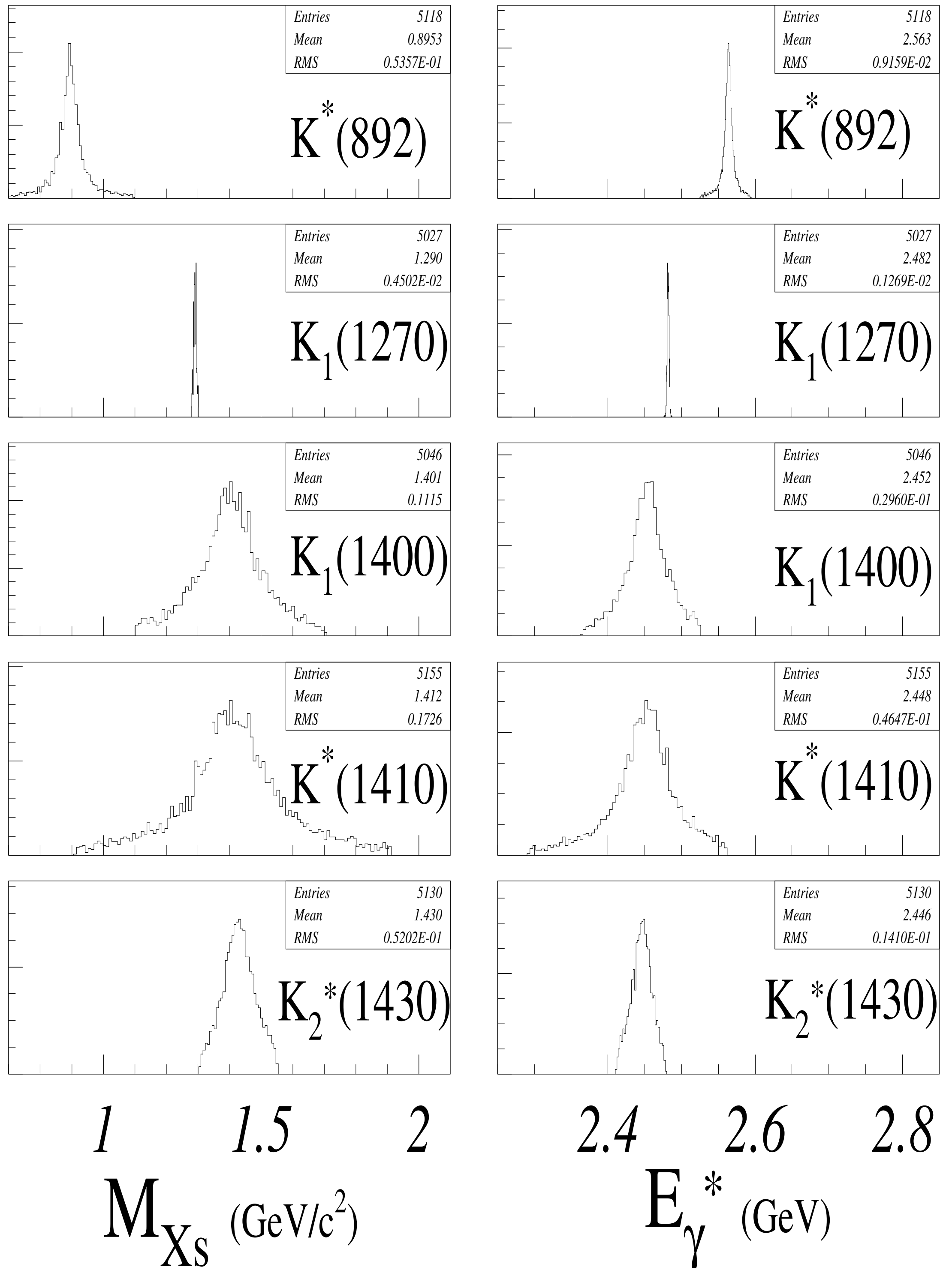

Figure 3.2: *The M_{X_s} and $E_\gamma^\star$ spectra for the five $B_{u(d)} \to X_s\gamma$ resonant penguin event samples generated with* HVFL05*. Approximately* 2500 *events were generated for each B_d penguin decay channel and the corresponding B_u penguin decay channel. (Note that the mass width for the generated K_1(1270) resonances is too small [1] but this discrepancy has no effect on the results presented in this thesis.)*

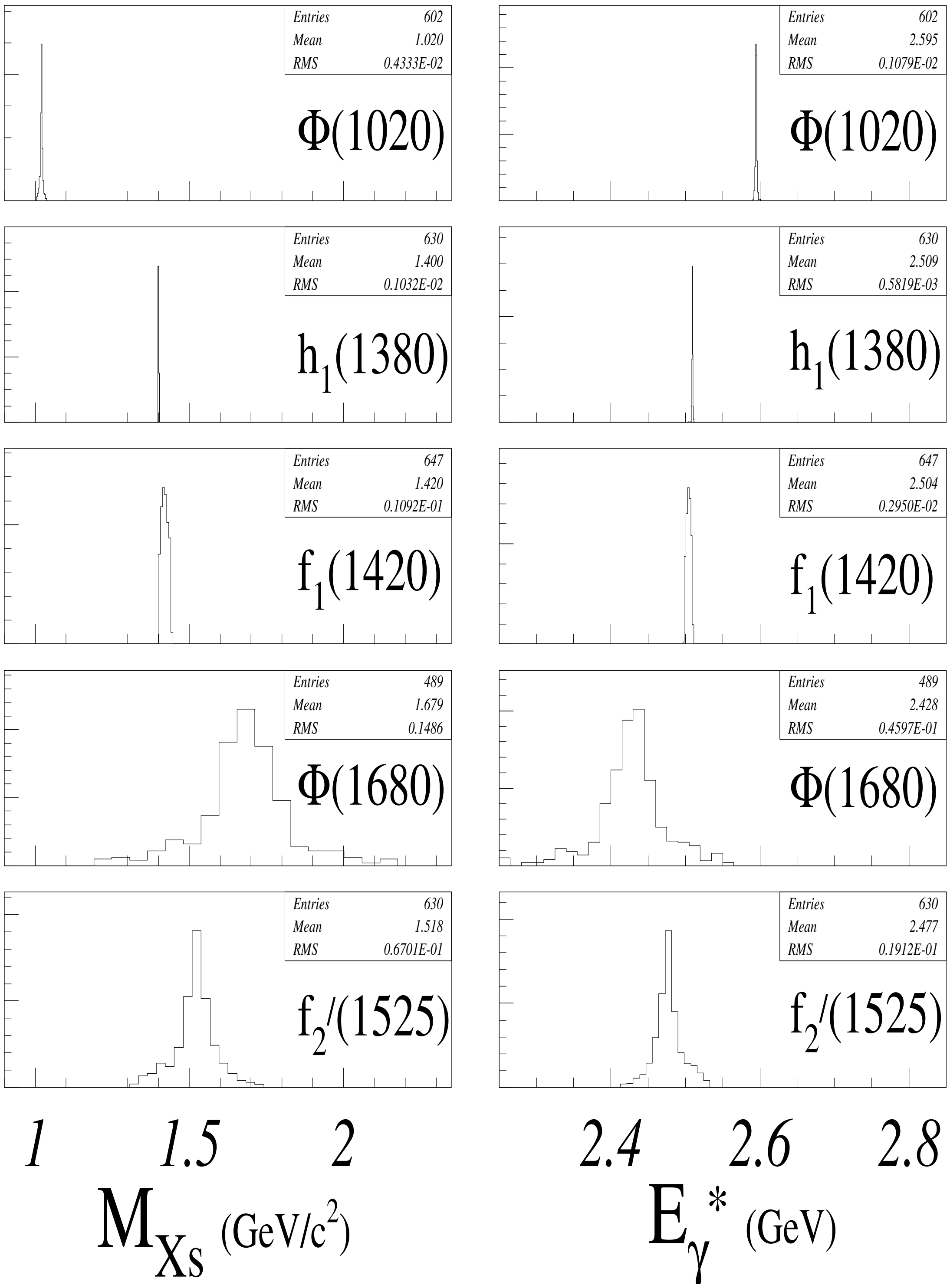

Figure 3.3: *The M_{X_s} and $E^{\star}_{\gamma}$ spectra for the five $B_s \to X_s\gamma$ resonant penguin event samples generated with* HVFL05. *Approximately* 600 *events were generated for each channel. (Note that the $h_1(1380)$ resonance is not well established and furthermore its mass width is predicted to be more than shown above [1] but this discrepancy has no effect on the results presented in this thesis.)*

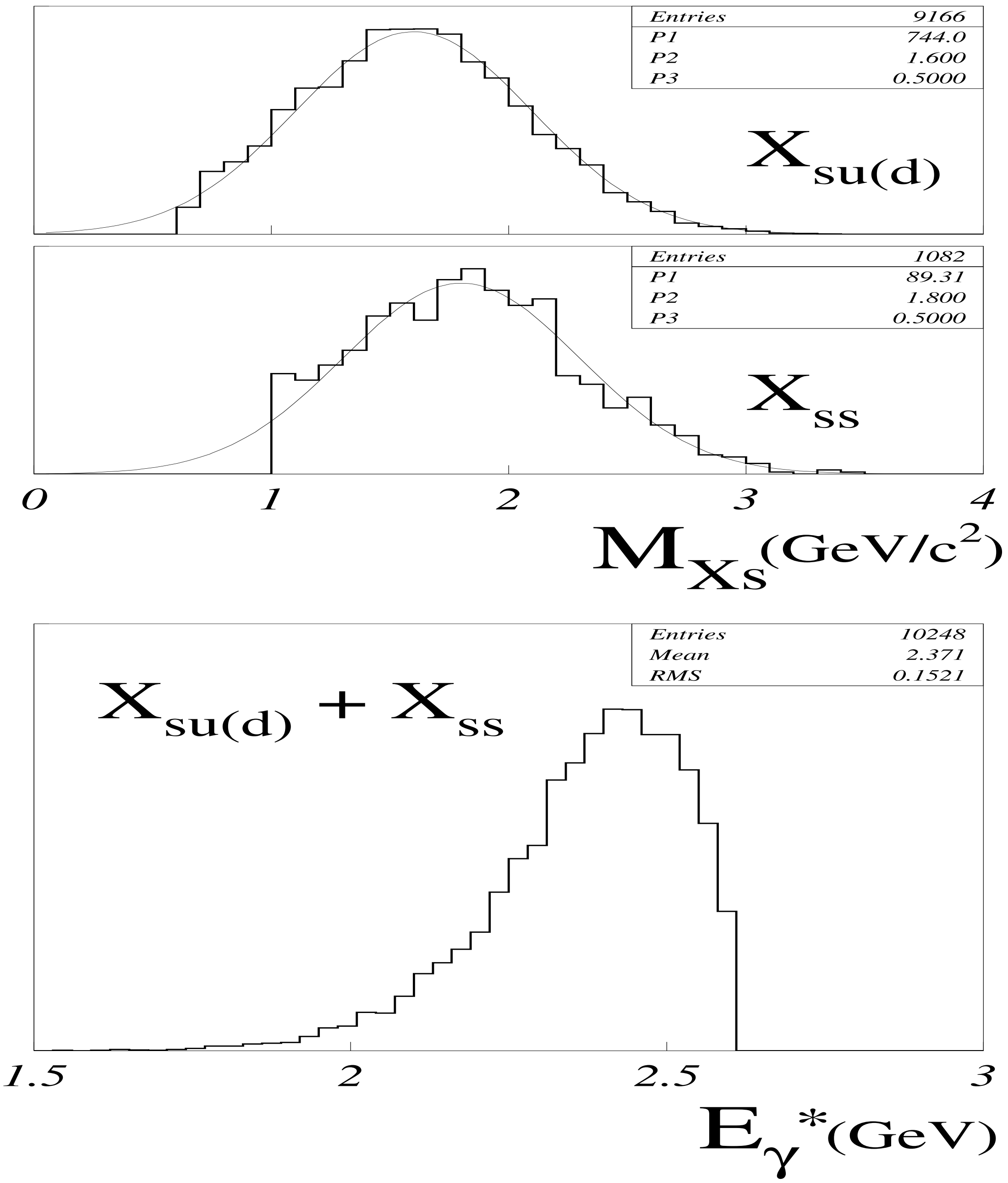

Figure 3.4: *The X_s mass spectra and the resulting $E_\gamma^\star$ spectrum for the non-resonant penguin events generated with HVFL05: The mass spectra for $X_{su(d)}$ and X_{ss} were chosen to reproduce Gaussian functions with the means and sigmas (represented by P2 and P3 respectively) as shown. The $X_{su(d)}$ and X_{ss} masses were further constrained by low mass cut-offs roughly corresponding to the mass threshold for producing $K\pi$ and KK pairs, respectively. The $E_\gamma^\star$ spectrum corresponding to the total non-resonant X_s mass spectrum is also shown.*

As detailed above, the non-resonant penguin events were designed to reproduce roughly the Ali-Greub inclusive $B \to X_s\gamma(g)$ photon spectrum. The spectator model, which produces such spectra, uses a B meson wave function model and includes gluon bremsstrahlung and higher order radiative effects. The model has a number of input parameters which can be varied to take into account recent measurements and their uncertainties. A program written by Ali and Greub [33] was used to obtain the photon spectrum for the following input parameters:

- M_B = 5.2907 GeV/c^2, where M_B is the average B meson mass. This was calculated using the 1996 Particle Data Group (PDG) values for the B_u, B_d and B_s masses along with their relative production fractions[1].
- m_t = 180 GeV/c^2, where m_t is the 1996 PDG top mass central value.
- P_F = 265 MeV/c, where P_F is the Fermi momentum of the b quark in the B meson. This value was taken from the results of a CLEO fit [34] to their semileptonic B decay data, using a spectator model, where P_F was varied in the fit along with m_c, the mass of the charm quark in the final state.
- m_q = 150 MeV/c^2, where m_q is the mass of the spectator quark in the B meson and was fixed to this value in the CLEO fit described above.
- m_s = 491 MeV/c^2, where m_s is the mass of the s quark in the final X_s state. This value was tuned to ensure the kinematic $E^{\star}_{\gamma}$ cut off at 2.6 GeV.

The resulting photon spectrum is shown in figure 3.5. The low energy photons in this spectrum, where the gluon in $B \to X_s\gamma(g)$ dominates, were considered negligible and not simulated in the non-resonant penguin events. The shape of the spectrum depends critically on the Fermi momentum; for which the CLEO fit [34] gives a value of (265 $\pm$ 25) MeV/c for a fixed m_q of 150 MeV/c^2 — see figure 3.6. The non-resonant Monte Carlo events were reweighted to reflect this set of input parameters for a P_F value of 265 MeV/c as described in figure 3.7. These reweighted non-resonant events were then used, along with the resonant events, to make an inclusive signal Monte Carlo.

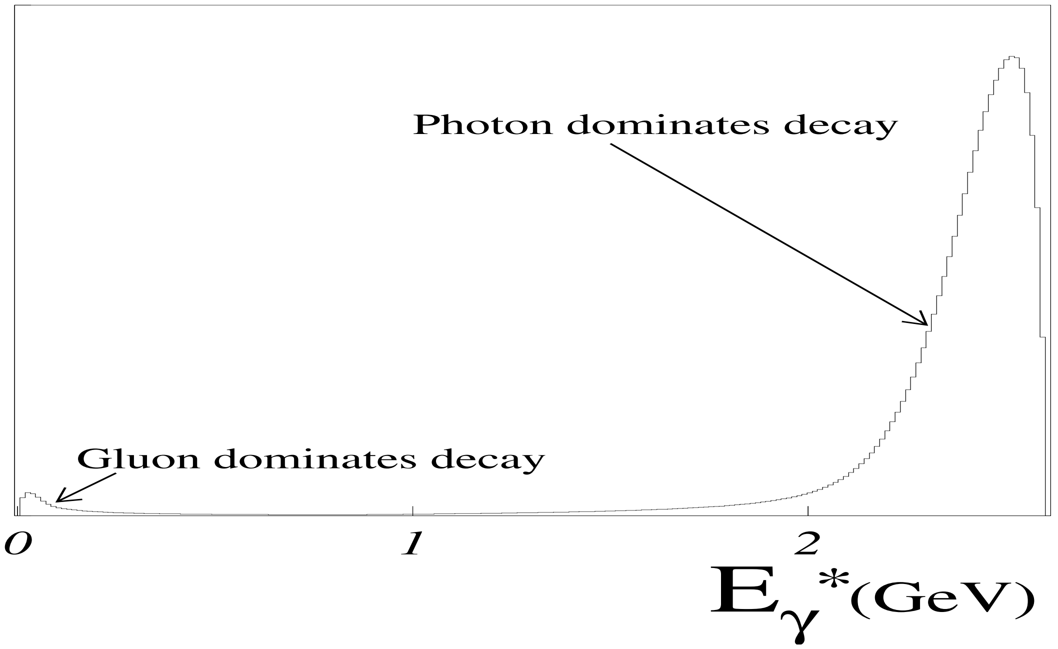

Figure 3.5: *The Ali-Greub inclusive $B \rightarrow X_s\gamma(g)$ photon spectrum for P_F = 265* MeV/c.

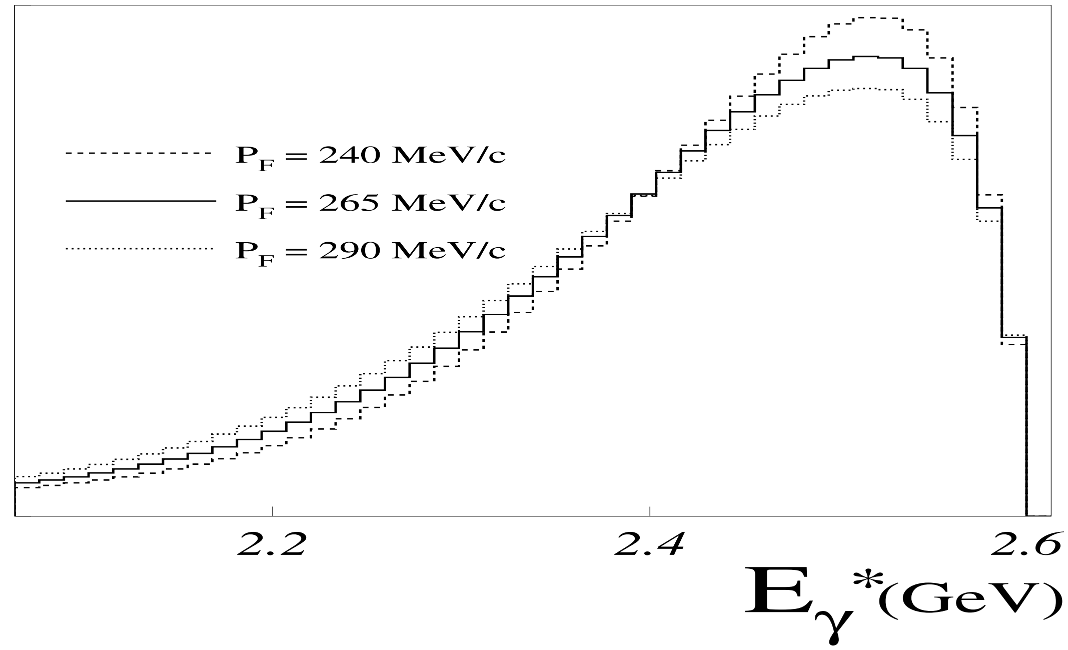

Figure 3.6: *The Ali-Greub inclusive $B \rightarrow X_s\gamma(g)$ photon spectrum for three P_F values.*

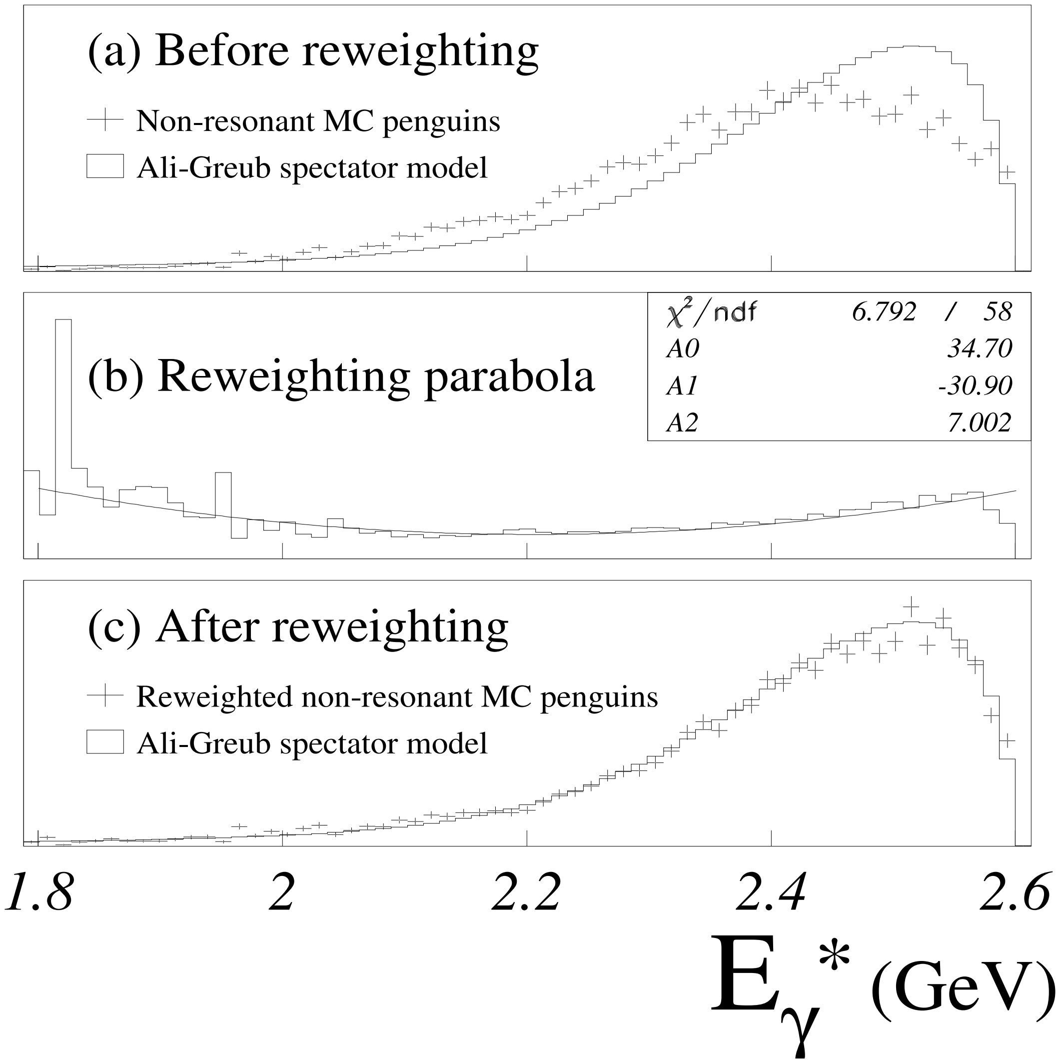

Figure 3.7: *Reweighting non-resonant penguins: a) Before reweighting, the non-resonant penguins are inconsistent with the Ali-Greub photon spectrum for a Fermi momentum of* 265 MeV/c. *b) By dividing the Ali-Greub histogram by the non-resonant histogram and fitting a parabola over the range shown, a weighting function can be obtained. c) When the non-resonant penguin events are reweighted by a factor dependent on their* $E^{\star}_{\gamma}$ *value, using the parabolic weighting function, the agreement between the spectra is good.*

3.3 Inclusive signal Monte Carlo.

Although there are, in effect, "two types of penguins" there are many possible exclusive resonant channels. The composition of the inclusive signal Monte Carlo used in this analysis is based primarily on theoretical predictions for the exclusive ratios $R_{K^{**}} = \Gamma(B \to K^{**}\gamma)/\Gamma(B \to X_s\gamma)$ from Heavy Quark Effective Theory [31], where K^{**} is some K-resonance. The CLEO measurement[15, 16] and its uncertainty is used for $R_{K^*} = \Gamma(B \to K^*(892)\gamma)/\Gamma(B \to X_s\gamma)$. The $s\bar{s}$ meson resonances are assumed to be in the same relative proportions as the K-resonances. In both cases these R values are summed and the remaining branching ratio made up with non-resonant penguin decays. Baryonic penguins, as stated above, were modelled by $\Lambda_b \to \Lambda\gamma$. The resulting signal Monte Carlo composition is shown in table 3.1, where the b hadron production fractions are taken to be:
$b \to B_u$ (37.8%); $b \to B_d$ (37.8%); $b \to B_s$ (11.2%); and $b \to \Lambda_b$ (13.2%) [1].
The spectra for this inclusive Monte Carlo model is shown in figure 3.8.

3.4 Model dependency

The analysis recounted in this thesis depends heavily on how well both the signal and background processes in the ALEPH data are simulated. Monte Carlo events are used to develop and fine-tune the analysis in order to attain good discrimination between signal and background processes. Then, on isolating a signal of $b \to s\gamma$ in E^*_γ in the ALEPH data, the inclusive signal Monte Carlo gives some measure of the efficiency for picking up penguins. However, the model here described is imperfect due, for example, to uncertainties in the exclusive $B \to X_s\gamma$ fractions and the Fermi motion of the b quark. Thus, these uncertainties must be taken into account in the resulting measurement of the $b \to s\gamma$ branching ratio. By varying the model within its uncertainties and seeing how the measurement changes about the central value, systematic errors may be evaluated.

Decay channel	No. of events generated	Exclusive decay fraction, R(%)
$B_{u(d)} \to K^*(892)\gamma$	5118	13.6 ± 5.1
$B_{u(d)} \to K_1(1270)\gamma$	5027	5.5 ± 2.1
$B_{u(d)} \to K_1(1400)\gamma$	5046	7.2 ± 2.6
$B_{u(d)} \to K^*(1410)\gamma$	5155	6.7 ± 2.6
$B_{u(d)} \to K_2^*(1430)\gamma$	5130	20.6 ± 7.5
$B_{u(d)} \to K(n\pi)\gamma$	9166	$22.0 \pm \mathbf{19.9}$
		$\Rightarrow 37.8 + 37.8 = 75.6$
$B_s \to \phi(1020)\gamma$	602	2.0 ± 0.8
$B_s \to h_1(1380)\gamma$	630	0.8 ± 0.3
$B_s \to f_1(1420)\gamma$	647	1.1 ± 0.4
$B_s \to \phi(1680)\gamma$	489	1.0 ± 0.4
$B_s \to f_2'(1525)\gamma$	630	3.0 ± 1.1
$B_s \to KK(n\pi)\gamma$	1082	$3.3 \pm \mathbf{3.0}$
		$\Rightarrow 11.2$
$\Lambda_b \to \Lambda(1116)\gamma$	5099	13.2 ± 4.1
$\Rightarrow b \to s\gamma$		$\Rightarrow 75.6 + 11.2 + 13.2 = 100$

Table 3.1: *Inclusive signal Monte Carlo composition: The R-value uncertainties for the non-resonant penguin channels ($B_{u(d)} \to K(n\pi)\gamma$ and $B_s \to KK(n\pi)\gamma$), which are in bold type above, are conservatively taken to be the linear sum of the R-value uncertainties for the resonant channels. The R-value uncertainty for the baryonic channel ($\Lambda_b \to \Lambda(1116)\gamma$) is taken to be the $b \to \Lambda_b$ production fraction uncertainty.*

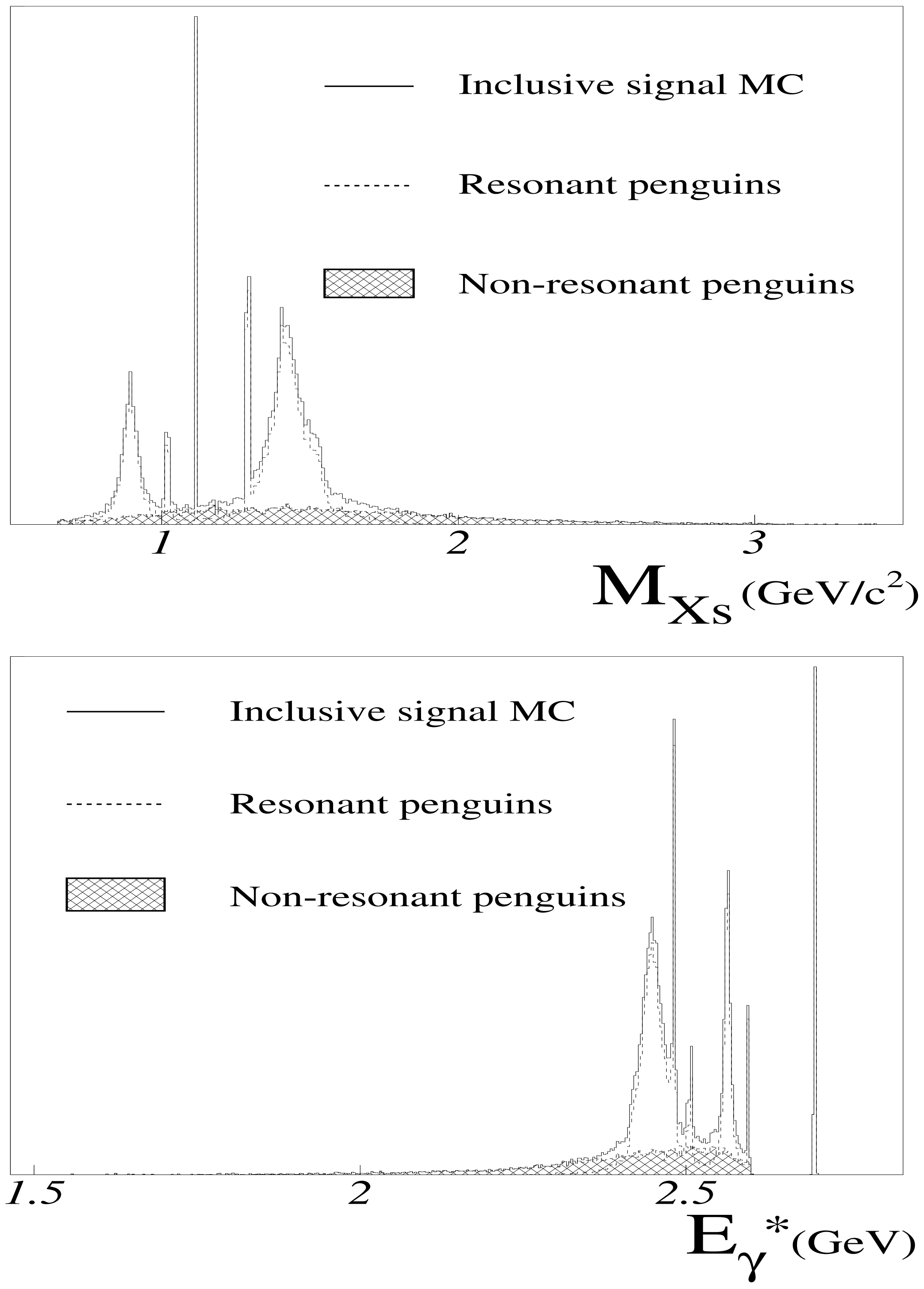

Figure 3.8: *The inclusive signal Monte Carlo X_s mass spectrum and corresponding $E_\gamma^\star$ spectrum: The contributions from resonant penguins and non-resonant penguins are shown. The contribution from $\Lambda_b \to \Lambda(1116)\gamma$ decays has been scaled down by a factor of two in these figures so the other channels can be seen more clearly. The different number of distinct peaks in the two plots is due to the relation between $E_\gamma^\star$, M_B, and M_{X_s} shown in equation 3.1 and the difference between the $B_{u(d)}$, B_s, and Λ_b masses.*

Chapter 4

Event preselection: bs and γs

4.1 Introduction

In the years 1991 to 1995, during the first phase of LEP running, with the complete ALEPH detector (including VDET) in place, ALEPH collected 4.1 million hadronic Z^0 events. Therefore, assuming the Standard Model prediction for the branching ratio of $(3.28 \pm 0.33) \times 10^{-4}$ [8], there ought to be ≈ 570 $b \to s\gamma$ decays amongst this data. To cut this immense data sample down to a manageable size, without throwing away too many precious penguins, a careful preselection of the events was performed. This preselection reduces the data sample to a relatively small number of hadronic events, which have high b-purity and contain one or more high energy 'candidate' photons.

4.2 Hadronic event selection

From the initial data set of 4,062,343 million hadronic Z^0 decays, events are selected in the first instance according to the standard ALEPH hadronic event selection. This selection requires at least five charged tracks in the TPC that have at least four reconstructed coordinates and a polar angle greater than 18.2° ($|\cos\theta| < 0.95$), which ensures that at least six TPC pad rows are traversed. The distance of closest approach of the tracks to the ALEPH origin must be less than

10 cm along the beam direction and 2 cm transverse to it. Finally, the sum of the energies of the tracks satisfying these criteria (assuming the pion mass for each) is required to be larger than 10% of the centre of mass energy.

This selection has an efficiency of $\approx 99\%$ and introduces no significant flavour bias. The background from τ events and $\gamma\gamma$ interactions are $\approx 0.62\%$ and $\approx 0.3\%$ respectively [35] and can be safely ignored in this analysis. The latter produce particles with negligible lifetime and are effectively removed after applying typical impact parameter tag cuts. The τ has a significant lifetime but its decay products have small impact parameters owing to the relatively small τ mass. Consequently, τ events also form a negligible background ($\approx 0.05\%$) once typical tag cuts are applied.

To allow the calculation of variables used to tag $b\bar{b}$ events, each event must have at least one track with VDET hits and a minimum of two jets with momentum greater than 10 GeV and polar angle greater than $5.7°$ — these requirements are discussed in more detail in section 4.4. In each remaining event, the thrust axis is determined using all energy flow objects — described in section 2.5.3. Then, to ensure the event is well contained within the detector volume, the cosine of the polar angle of the thrust axis is required to be less than 0.9, as shown in figure 4.1.

These cuts give an overall acceptance of 88.2% leaving 3,583,365 hadronic events.

4.3 Candidate photon selection

Candidate photons are identified using the ALEPH photon identification package which was described in section 2.5.4. In this analysis, events passing the hadronic event selection cuts must also contain at least one candidate photon which fulfills the following requirements. Only those candidate photons which do not share an ECAL cluster with any other candidate photon are accepted. The candidate photon's energy, E_γ, is required to be greater than 4.75 GeV, as shown in fig-

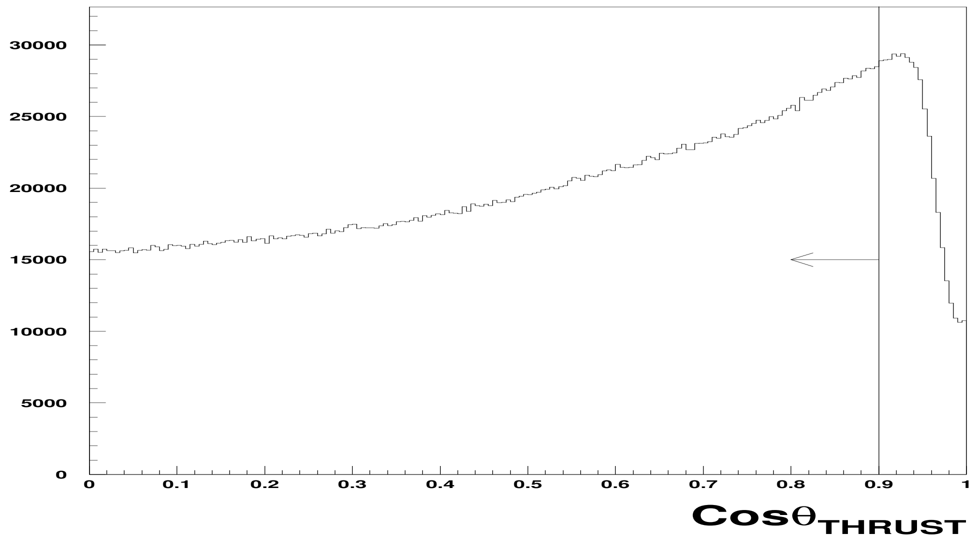

Figure 4.1: *The cosine of the polar angle of the thrust axis for all data events satisfying the* ALEPH *hadronic event selection and the impact parameter tag event selection. The cut on this variable is indicated by a vertical line and an arrow showing which events are selected.*

ure 4.2. Finally, to reduce π^0 contamination the condition is imposed that the cluster cannot be combined with another neutral cluster in the event to form a pair with invariant mass less than 0.2 GeV/c^2, as shown in figure 4.3.

4.4 $b\bar{b}$ event selection

Events which satisfy the hadronic event selection and contain at least one candidate photon which passes the candidate photon selection cuts are subjected to further scrutiny by using the 'b-tagging' algorithm which is described below.

4.4.1 Tagging $b\bar{b}$ events

In Z^0 decays, most of the b hadrons are to be found in $b\bar{b}$ events. The b hadrons produced in these events are boosted such that their long lifetime is further lengthened (in the detector frame of reference) and they travel two to three millimetres before decaying. They typically decay to about five charged particles on average,

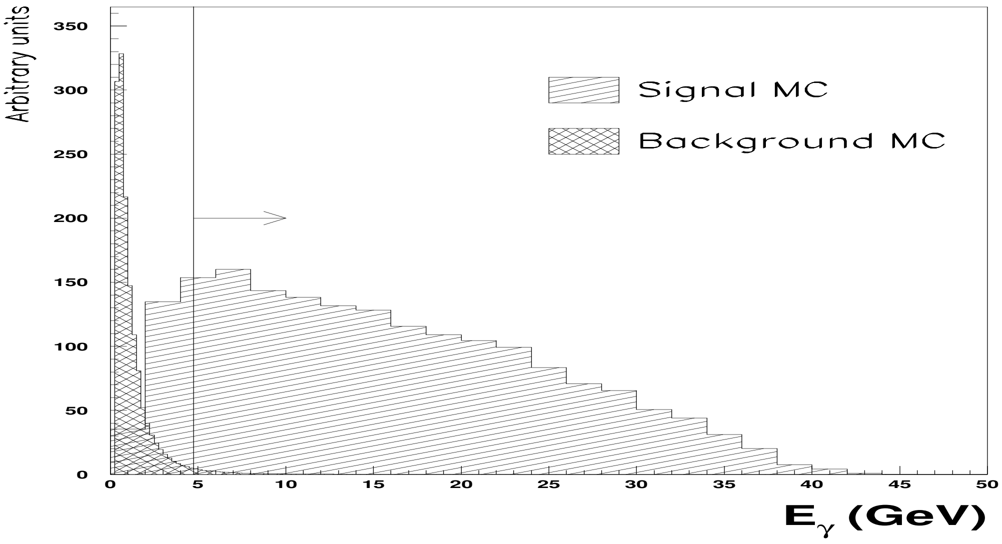

Figure 4.2: *The photon energy cut for candidate photons in hadronic events satisfying the hadronic event selection described in section* 4.2. *Signal Monte Carlo photons are shown as well as background Monte Carlo photons. The normalisations of the two event samples are arbitrary. The preselection cut on this variable, E_γ is indicated by a vertical line and an arrow showing which candidate photons pass the cut.*

including the decay products of secondary charmed hadrons. The b hadrons are, on average, an order of magnitude more massive than their decay products so their decays are highly energetic. Now, c hadrons, although having similar decay lengths to those of b hadrons, are lighter and their decays have lower charged multiplicities ($\approx$ two to three tracks), while most of the tracks in $Z^0 \to u\bar{u}$, $d\bar{d}$, $s\bar{s}$ events originate from the primary interaction point. Consequently, $b\bar{b}$ events can be effectively 'tagged' with high purity by requiring the presence of many charged tracks with significant impact parameters with respect to the Z^0 decay point. ALEPH uses these distinguishing features to tag b hadron decays using an algorithm which relies heavily on the precise tracking afforded by VDET. The algorithm, which is described fully in [36] and briefly below, involves the measurement of track impact parameters in an event which are then combined to give a quantity which can be used for b-tagging.

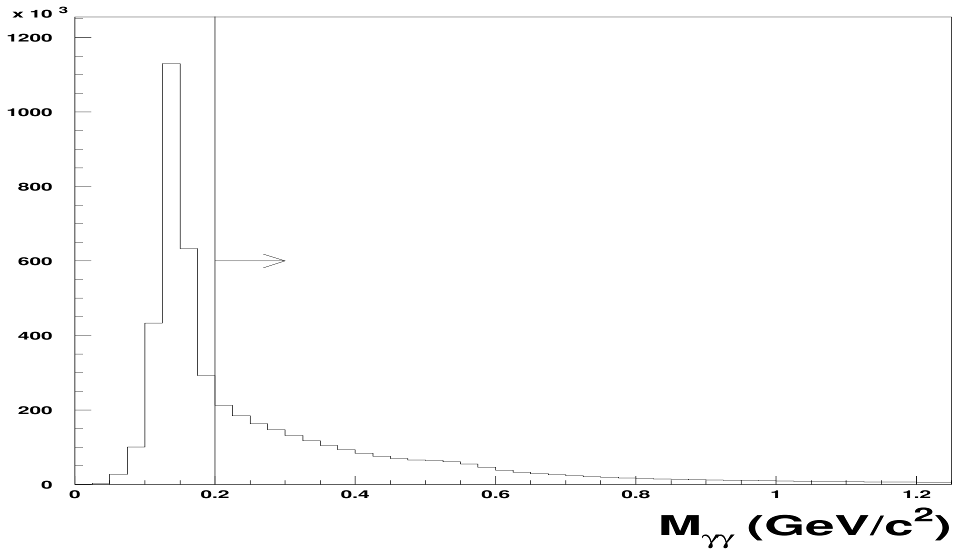

Figure 4.3: *The cut to reduce the number of photons coming from π^0 mesons is shown. The distribution is the mass of each candidate photon when combined with another candidate photon in the event to give a mass closest to the π^0 mass. The distribution is for all candidate photons contained in events from the total data sample which satisfy the hadronic event selection described in section* 4.2. *The cut on this variable, $M_{\gamma\gamma}$, is indicated by a vertical line and an arrow showing which candidate photons pass the cut.*

4.4.2 Measuring track impact parameters in 3D

The true three-dimensional impact parameter δ of a particle is here defined as its distance of closest approach to the Z^0 decay point. Figure 4.4 shows a schematic diagram of a b hadron decay with the impact parameter of one of its decay products indicated. In order to measure the impact parameters for the tracks from a b hadron decay, the b hadron direction and the Z^0 decay point must first be reconstructed.

The b hadron flight direction

The directions of the b hadrons in a $Z^0 \rightarrow b\bar{b}$ event are obtained by clustering charged and neutral objects into jets using the JADE scaled minimum mass algorithm [37]. In this algorithm, the pair of charged and neutral objects in an

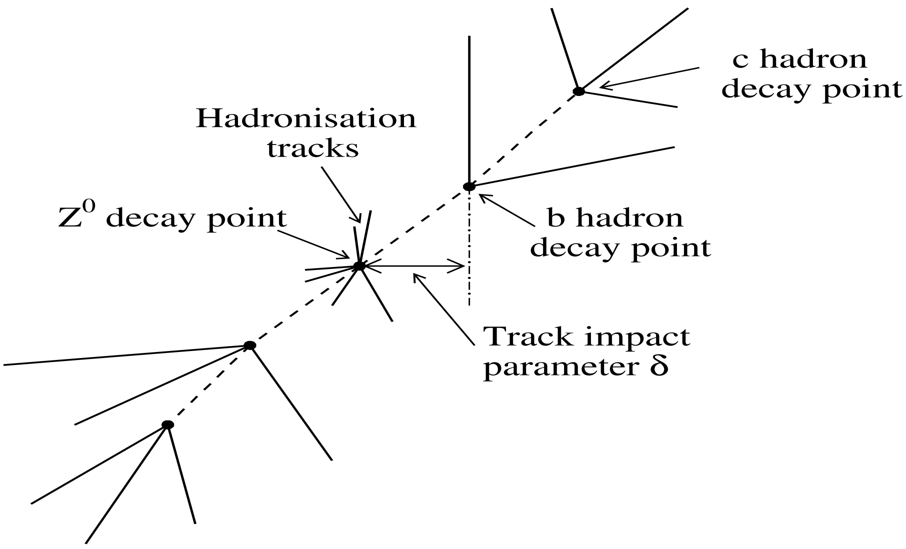

Figure 4.4: *Schematic diagram of a b hadron decay.*

event whose combination gives the smallest invariant mass is combined to form one composite object, or cluster. This process is repeated with the next lowest mass pair and so on until the reduced number of 'objects' is such that no pair i and j has a scaled invariant mass less than a jet-resolution threshold, or ycut. The square of the scaled invariant mass, y_{ij}, of two particles is given by

$$y_{ij} = \frac{M_{ij}^2}{E_{\mathsf{LEP}}^2} \ , \tag{4.1}$$

where M_{ij} and E_{LEP} are the invariant mass of particles i and j, and the LEP centre of mass energy respectively. The remaining clusters of objects are then the jets of the event. The jet definition which was found to give the best angular resolution for b hadrons used a ycut of 0.02.

As mentioned in section 4.2, the impact parameter algorithm rejects an event unless its two highest momentum jets each have a polar angle greater than 5.7° and have energies greater than 10 GeV.

The Z^0 decay point

The Z^0 decay point, or primary interaction point, is determined event by event by combining tracking information within the event with information on the location of the luminous region, or 'beamspot'. Each charged track in the event is projected onto the plane perpendicular to its associated jet's direction. Then, whether a track comes from the primary interaction point or from the decay of the b hadron, it will appear to originate from the primary interaction point when viewed in this plane. These projected tracks are then combined with beamspot information in the $x - y$ plane in a χ^2 fit to the primary interaction point. This procedure gives a measured resolution on the Z^0 decay point of 50 μm in the x and z directions and less than 10 μm in the y direction where the beamspot information dominates. This algorithm is described more fully in [38].

Track impact parameters

With the b hadron direction and Z^0 decay point reconstructed, the track impact parameters are measured as shown in figure 4.5 and now described. Each track helix is linearised at the point, B, where it is closest to its associated jet, $\hat{J}$. The impact parameter δ of a charged track is then defined as the distance of closest approach of the corresponding linearised track to the reconstructed primary interaction point, A, and is signed according to:

$$\tilde{\delta} \;=\; sign((\overrightarrow{B - A}) \cdot \hat{J})\, \delta \quad . \tag{4.2}$$

That is, $\tilde{\delta}$ is positive if the point of closest approach of the track helix to its jet lies in that half of the event defined by the jet direction. Due to the finite experimental resolution, a random sign is hence assigned to tracks which actually originate from the primary vertex.

4.4.3 The 3D impact parameter tag

Tracks must satisfy the following selection criteria (referred to in section 4.2) if they are to be used in the impact parameter tag calculations. Each track

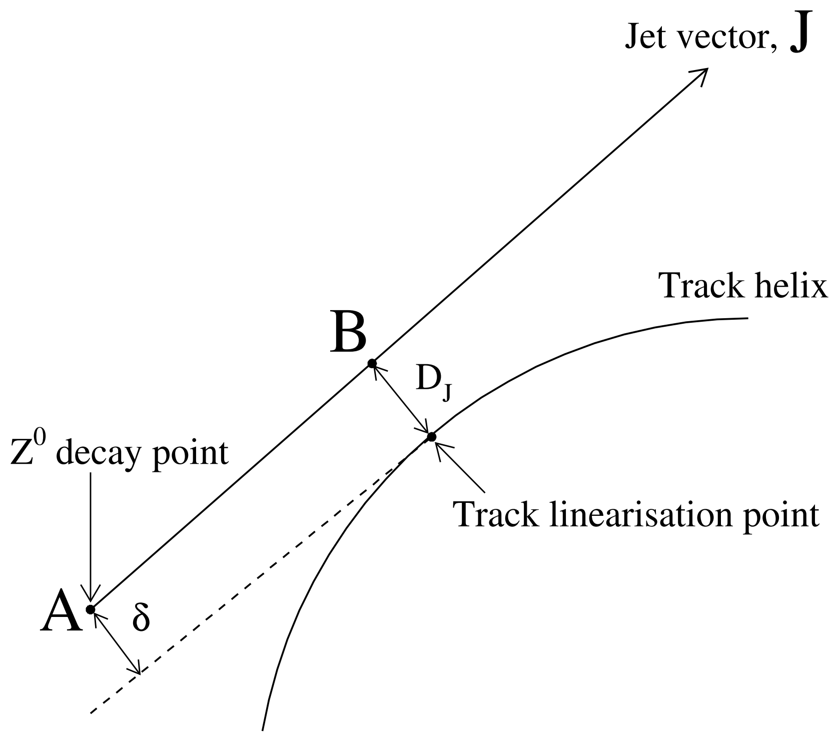

Figure 4.5: *The reconstruction of track impact parameters.*

must have at least one VDET hit, in both $r - \phi$ and z dimensions. In order to decrease background from material interactions and very long lived particles such as K^0 mesons each track is required to have an impact parameter of less than 2.5 mm. Finally, the distance of closest approach of each track to the jet-axis (D_J in figure 4.5) is required to be less than 0.4 mm for tracks with one VDET hit and less than 0.7 mm for tracks with two VDET hits. This reduces the number of tracks with misassociated VDET hits. The measured impact parameters for these tracks and their uncertainties can be used to produce a quantity for tagging $Z^0 \to b\bar{b}$ events.

Impact parameter significance

The statistical resolution on the impact parameter varies as a function of momentum, angle and the number of reconstructed coordinates within the vertex detector. These functional dependences can be removed by considering not the measured impact parameter itself but its estimated statistical significance, $\tilde{\delta}/\sigma_{\tilde{\delta}}$, where $\sigma_{\tilde{\delta}}$ is the uncertainty on the measured $\tilde{\delta}$. Figure 4.6 shows the signed impact parameter significance distribution for Monte Carlo simulated events. The distribution would be symmetric about zero if all tracks originated from the primary interaction point. The excess on the positive side is the lifetime signal, and is attributed to high impact parameter tracks from the decays of b hadrons and to a lesser extent c hadrons. The negative half of the distribution is a measure of the background under the lifetime signal.

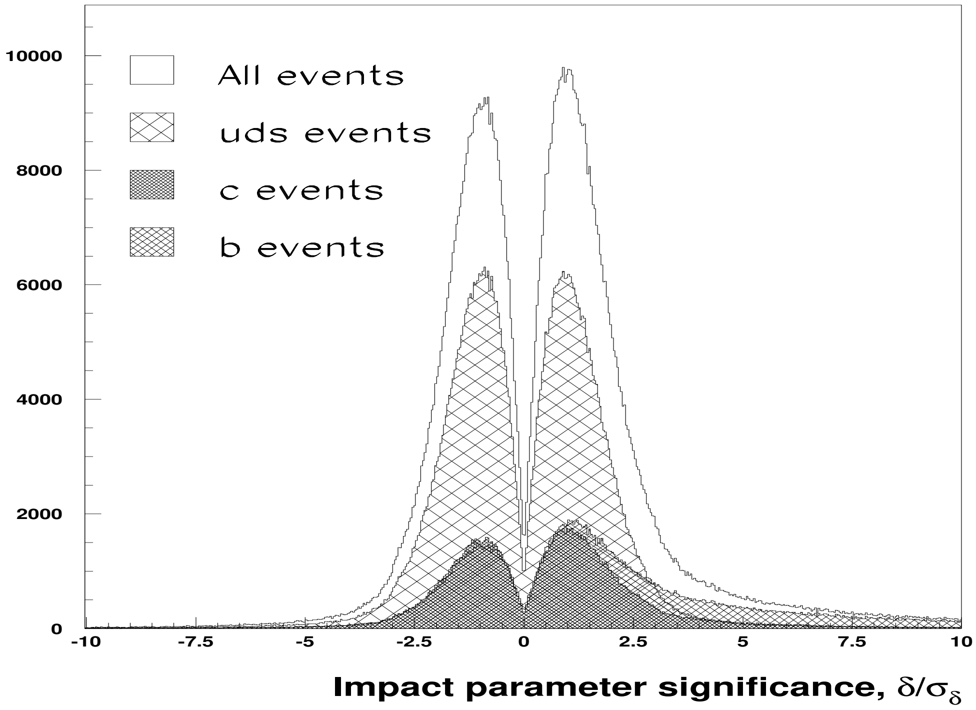

Figure 4.6: *The signed impact parameter significance distribution for Monte Carlo simulated events.*

The negative impact parameter significance data distribution is fitted with the sum of a gaussian and two exponentials [36]. This fit is a direct measurement of the experimental resolution of the impact parameter significance. All track probabilities used in the impact parameter tag algorithm are obtained using the resolution functions obtained in the data and are hence not dependent on Monte Carlo simulation.

Track probability

The negative impact parameter significance fit to the data is used to assign to a given charged track with impact parameter information a probability P_t, that it originated from the primary interaction point. The probability for a track with impact parameter significance $\tilde{\delta}/\sigma_{\tilde{\delta}}$ is defined as

$$P_t(\tilde{\delta}/\sigma_{\tilde{\delta}}) = \int_{|\tilde{\delta}/\sigma_{\tilde{\delta}}|}^{+\infty} R(x)dx \, , \tag{4.3}$$

where $R(x)$ is the resolution function obtained from data. That is, $P_t(\tilde{\delta}/\sigma_{\tilde{\delta}})$ is the probability that a track originating from the primary vertex could be measured to have an impact parameter significance $\tilde{\delta}/\sigma_{\tilde{\delta}}$, or greater.

Hemisphere probability

Each event is split into two hemispheres defined by the thrust axis. In each hemisphere, those charged tracks with impact parameter information are combined to form a probability P_{hem} for that hemisphere,

$$P_{hem} = \Pi \sum_{j=0}^{N-1} \frac{(-ln\Pi)^j}{j!} \, , \tag{4.4}$$

where

$$\Pi = \prod_{i=1}^{N} P_{t_i} .$$

P_{hem} is the probability that a set of N tracks all originating from the primary interaction point, could reproduce the observed set of track probabilities, or any other set equally likely or more unlikely. The proof that this quantity behaves as a probability is given in [36]. Thus, b hemispheres can be chosen preferentially by accepting only those hemispheres with P_{hem} values *below* an arbitrary cut value.

In $b \to s\gamma$ hemispheres, the charged track multiplicity is lower than in more typical b-decay hemispheres. Furthermore, approximately half of the energy from the decaying penguin b hadron is taken by the photon. Thus, only the hemisphere opposite to the candidate photon is used in this analysis to tag $b\bar{b}$ events. For candidate photons, the opposite hemisphere probability, P_{hem}^{opp}, is required to be less than 0.125 in the event preselection, as shown in figure 4.7.

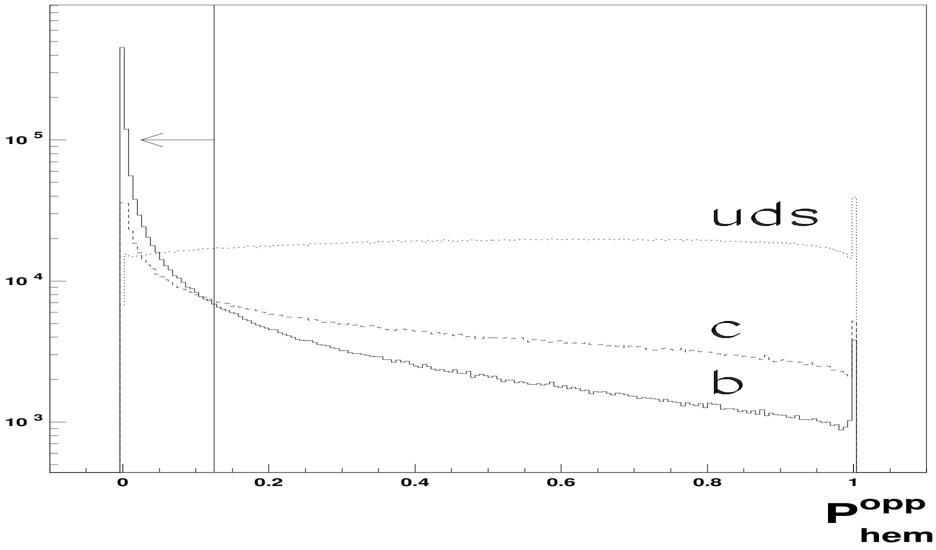

Figure 4.7: *The P^{opp}_{hem} distributions for all background Monte Carlo photons in events satisfying the hadronic event selection described in section 4.2. This is the probability that all tracks in the hemisphere opposite to a candidate photon are consistent with coming from the primary interaction point. The distributions are for uds, c, and b-events, revealing the 'b-tagging' power of the impact parameter algorithm. The preselection cut value is indicated by a a vertical line and an arrow showing which events are selected.*

4.5 Summary of the event preselection

The event preselection, described above, proceeds in six stages. The first three stages select well-contained hadronic events which can be used by the impact parameter tag algorithm, as described in section 4.2. The latter three stages select events which contain at least one candidate photon which satisfies the photon selection described in section 4.3 and the hemisphere probability cut described in section 4.4.3. These six stages can be summarised as follows:

1. Standard ALEPH hadronic event selection

2. Impact parameter tag event selection

3. $\cos\theta_{Thrust} < 0.9$

4. At least one candidate photon which does not share its ECAL cluster with any other candidate photon and has $E_\gamma > 4.75$ GeV

5. Probability that all tracks in the opposite hemisphere to the candidate photon come from the primary interaction point, P_{hem}^{opp}, is < 0.125

6. The candidate photon, when combined with any other candidate photon in the event, has $M_{\gamma\gamma} > 0.2$ GeV/c^2

4.6 Efficiencies and acceptances

The $Z^0 \to q\bar{q}$ branching fraction is approximately 70% [1] but the identification of these events by ALEPH is not 100% efficient so the number actually detected can only be estimated. The standard ALEPH hadronic event selection, however, results in an extremely pure sample of hadronic *data* events and this number can more reliably be compared with the number of hadronic Monte Carlo *simulated* events remaining after the ALEPH standard hadronic event selection. Thus, to be consistent in this analysis, all signal Monte Carlo 'efficiencies' and background Monte Carlo 'acceptances' actually denote the fraction of *selected* hadronic events surviving the cuts rather than the fraction of *generated* events surviving the cuts.

After the event preselection cuts the data sample is reduced to 174257 events. These events contain at least one high energy candidate photon and have a b-purity of $\approx 51\%$. Table 4.1 shows the effect of each stage of the event preselection on the various exclusive $b \to s\gamma$ decay channels. The signal efficiency for each exclusive channel is defined as N_6/N_1, where N_1 is the number of events passing the standard ALEPH hadronic event selection cuts, and N_6 is the number surviving the event preselection. The overall efficiency for the inclusive $b \to s\gamma$ model is 46%. Table 4.2 shows the effect of each stage of the event preselection on data and the standard ALEPH Monte Carlo. After the preselection, the acceptances (N_6/N_1) for the data years are consistent with each other, except for the 1994 data which has a significantly higher acceptance than the other four years. The acceptances for the three sets of ALEPH standard Monte Carlo are inconsistent with each other and are significantly lower than the data acceptances. However, the acceptances for data and Monte Carlo are compared again after the further event selection cuts described in the following chapters.

Channel	N_0	N_1	N_2	N_3	N_4	N_5	N_6	Eff(%)
$K^*(892)$	5118	4970	4960	4421	3267	2362	2271	45.7 ± 1.0
$K_1(1270)$	5027	4913	4907	4379	3237	2356	2270	46.2 ± 1.0
$K_1(1400)$	5046	4928	4925	4422	3228	2356	2268	46.0 ± 1.0
$K^*(1410)$	5155	5020	5017	4508	3274	2350	2250	44.8 ± 0.9
$K_2^*(1430)$	5130	5000	4995	4485	3316	2465	2378	47.6 ± 1.0
$K(n\pi)$	9166	8946	8939	7934	5727	4190	4035	45.1 ± 0.7
$\phi(1020)$	602	586	585	521	398	291	281	48.0 ± 2.9
$h_1(1380)$	630	620	620	562	441	326	321	51.8 ± 2.9
$f_1(1420)$	647	638	635	564	413	301	294	46.1 ± 2.7
$\phi(1680)$	489	475	474	418	293	209	203	42.7 ± 3.0
$f_2'(1525)$	630	611	610	547	396	296	285	46.6 ± 2.8
$KK(n\pi)$	1082	1045	1043	938	690	507	484	46.3 ± 2.1
$\Lambda(1116)$	5099	4863	4851	4328	3220	2263	2226	45.8 ± 1.0
$\Rightarrow b \to s\gamma$								46.1 ± 0.4

Table 4.1: *The numbers of $b \to s\gamma$ Monte Carlo events passing each stage of the event preselection. The first column lists the Monte Carlo penguin decay channels. N_0 is the number of events generated for each channel. $N_1 \to N_6$ are the numbers of events passing the six stages of the event preselection respectively. The final column gives the signal efficiency (here defined as N_6/N_1) for each channel after these cuts.*

Events	N_1	N_2	N_3	N_4	N_5	N_6	Acc(%)
91 DATA	242557	241702	215521	50245	14322	10345	4.26 ± 0.04
92 DATA	671264	669354	595955	136632	38944	28193	4.20 ± 0.03
93 DATA	672003	669450	594136	137140	39606	28518	4.24 ± 0.03
94 DATA	1724276	1719583	1526567	352880	105372	76116	4.41 ± 0.02
95 DATA	737578	734835	651486	150817	42977	31085	4.21 ± 0.02
All DATA	4047678	4034924	3583365	827714	241221	174257	4.31 ± 0.01
92 MC $q\bar{q}$	3625191	3621715	3216840	742662	197828	134604	3.71 ± 0.01
93 MC $q\bar{q}$	2092829	2091213	1857738	476108	128647	85771	4.01 ± 0.01
94 MC $q\bar{q}$	3104155	3101701	2761457	715170	193816	137562	4.43 ± 0.01
All MC $q\bar{q}$	8822175	8814629	7836035	1933540	520291	357937	4.06 ± 0.01

Table 4.2: *The numbers of events in data and the background Monte Carlo passing each stage of the event preselection. The first column lists the event samples. $N_1 \rightarrow N_6$ are the numbers of events passing the six stages of the event preselection respectively. The final column gives the acceptance (N_6/N_1) for each event sample after these cuts.*

Chapter 5

Penguin b hadron reconstruction

5.1 Introduction

The signal of $b \to s\gamma$ is a distinctive peak in the energy spectrum for photons which have been boosted into the rest frame of their parent b hadrons. To see such a signal it is therefore essential to reconstruct accurately the b hadrons in penguin decays and thereby the boost of signal photons. To this end a dedicated $b \to s\gamma$ jet reconstruction algorithm was designed. The algorithm and its performance are described in this chapter.

5.2 $b \to s\gamma$ decay products

Figure 5.1 shows a schematic representation of a $b \to s\gamma$ event. The event is divided into two hemispheres by a plane orthogonal to the event thrust axis. In a penguin decay, the b hadron will decay to a photon plus a number of tracks coming from the X_s, the hadronic system containing the s quark. However, there will also be tracks in the same hemisphere which come from quark and gluon hadronisation. Nevertheless, penguin decay products are quite distinctive and it is possible to pick out the most probable X_s tracks in a penguin hemisphere and, on adding the photon to these tracks, to reconstruct a penguin b hadron with good resolution in angle and energy.

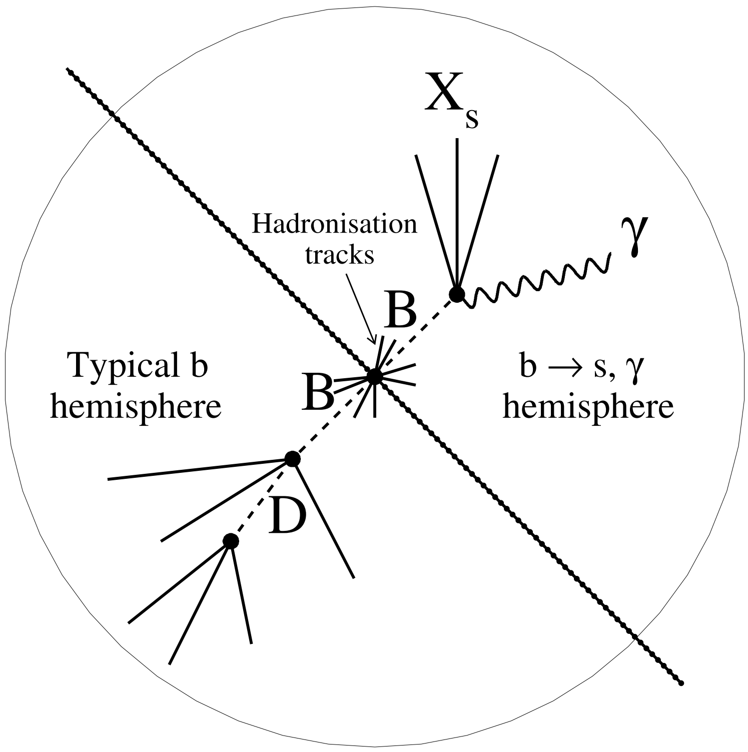

Figure 5.1: *A schematic representation of a penguin event.*

5.3 Track mass assignments

The energy flow algorithm described in section 2.5.3 produces a number of energy flow objects for each reconstructed event. For each event passing the preselection cuts described in chapter 4, the group of energy flow objects in the hemisphere, or hemispheres, containing a candidate photon (as defined in section 2.5.4) is reduced to a pool of 'tracks'. These tracks are assigned masses dependent on which type of particle they most closely resemble and are then used to build a jet. In each hemisphere containing a candidate photon, π^0 mesons are reconstructed from two candidate photons when the $\gamma\gamma$ invariant mass is compatible with the π^0 mass. K^0_S mesons are reconstructed similarly from any two oppositely signed charged tracks which form a vertex and have an invariant mass (assuming both charged tracks are pions) consistent with the K^0_S mass. Each hemisphere then consists of reconstructed π^0 and K^0_S mesons and the remaining charged tracks and neutral ECAL and HCAL clusters. Any neutral HCAL cluster is assumed to be a K_L^0 and hence given the kaon mass. All charged tracks are given the pion mass and, depending on the lateral spread of its energy deposition [1], a neutral ECAL object is given either zero mass (photon) or the pion mass (unresolved π^0). The resulting pool of 'tracks' is used in the jet reconstruction algorithm where each track is assigned a $b \to s\gamma$ track probability, as described in the next section.

5.4 $b \to s\gamma$ track probabilities

The $b \to s\gamma$ probability for each track in the hemisphere of a candidate photon is calculated as a function of its momentum, its rapidity, and, if the track is a charged track with VDET hits, its impact parameter significance. The track probabilities are obtained from probability functions which were produced using the HVFL04 two-body signal Monte Carlo events, described in section 3.2.1, which is a mixture of $B \to K^*\gamma$ (45%), $B \to K_2^*\gamma$ (45%), $B_s \to \phi\gamma$ (5%) and $B_s \to f_2'\gamma$ (5%). This is a different composition to that of the inclusive signal Monte Carlo used in the following analysis (see section 3.3) which would produce slightly different probability distributions. However the reconstruction algorithm depends on the ordering of tracks in an event, which is determined by their relative $b \to s\gamma$ probabilities, and this ordering will not be significantly affected by slight variations in the probability functions used.

Probability functions were produced separately for each type of 'track': charged tracks; K^0 mesons; π^0 mesons; and neutral calorimetry clusters. Plots (a) and (b) of figure 5.2 show the momentum-rapidity and impact parameter significance distributions for charged tracks from the $b \to s\gamma$ decay. Plots (c) and (d) of figure 5.2 show the corresponding hadronisation charged track distributions. The $b \to s\gamma$ decay tracks have a much harder momentum spectrum than the hadronisation tracks and possess larger rapidities. Similarly, due to the long lifetime of the b hadron, the signal tracks have more significant impact parameters than the hadronisation tracks, where the spectrum is dominated by the impact parameter resolution.

[1] The analysis of ECAL energy depositions is described in section 6.5.

In a given momentum bin the $b \to s\gamma$ probability, $\mathcal{P}_{mom}$, is defined as:

$$\mathcal{P}_{mom} = \frac{\text{No. of } b \to s\gamma \text{ decay tracks}}{\text{No. of } b \to s\gamma \text{ decay tracks } + \text{No. of hadronisation tracks}}$$

If the track is a charged track with VDET hits, the independent impact parameter significance probability is calculated in the same way as P_{mom} and the two probabilities, $\mathcal{P}_{mom}$ and $\mathcal{P}_{ip}$, are combined to give a final probability, $\mathcal{P}$:

$$\mathcal{P} = \frac{\mathcal{P}_{mom} \cdot \mathcal{P}_{ip}}{\mathcal{P}_{mom} \cdot \mathcal{P}_{ip} + (1 - \mathcal{P}_{mom}) \cdot (1 - \mathcal{P}_{ip}) \cdot R}$$

where R is the average fraction of the total number of signal decay charged tracks with VDET hits over the total number of hadronisation charged tracks with VDET hits in a $b \to s\gamma$ hemisphere (R=0.298). Plot 5.2(e) shows the momentum probability distribution in the rapidity bin, $2.5 <$ Rapidity < 2.75, and 5.2(f) shows the charged track impact parameter significance probability distribution. Each probability distribution is fitted with a fifth order polynomial and an asymptotic function. The momentum probability functions are constructed for ten different rapidity bins which are used to interpolate to the probability corresponding to any value of rapidity and momentum.

5.5 Jet building

In each event passing the event preselection described in chapter 4, an attempt is made to build a jet from each candidate photon therein, and its associated pool of tracks, using the $b \to s\gamma$ track probability functions described in the previous section. The reconstruction of a jet, which is assumed to be a penguin b hadron, begins with the candidate photon onto which tracks (K^0_S and π^0 mesons, charged tracks and neutral calorimeter objects) in the same hemisphere as the photon are added in order of decreasing $b \to s\gamma$ probability. The addition of tracks stops if, by adding the next highest probability track, the mass of the system is further from the mean B meson mass (which is taken to be 5.28 GeV/c^2) than it would be if the track had not been added. This reconstruction is performed in two stages, as follows :

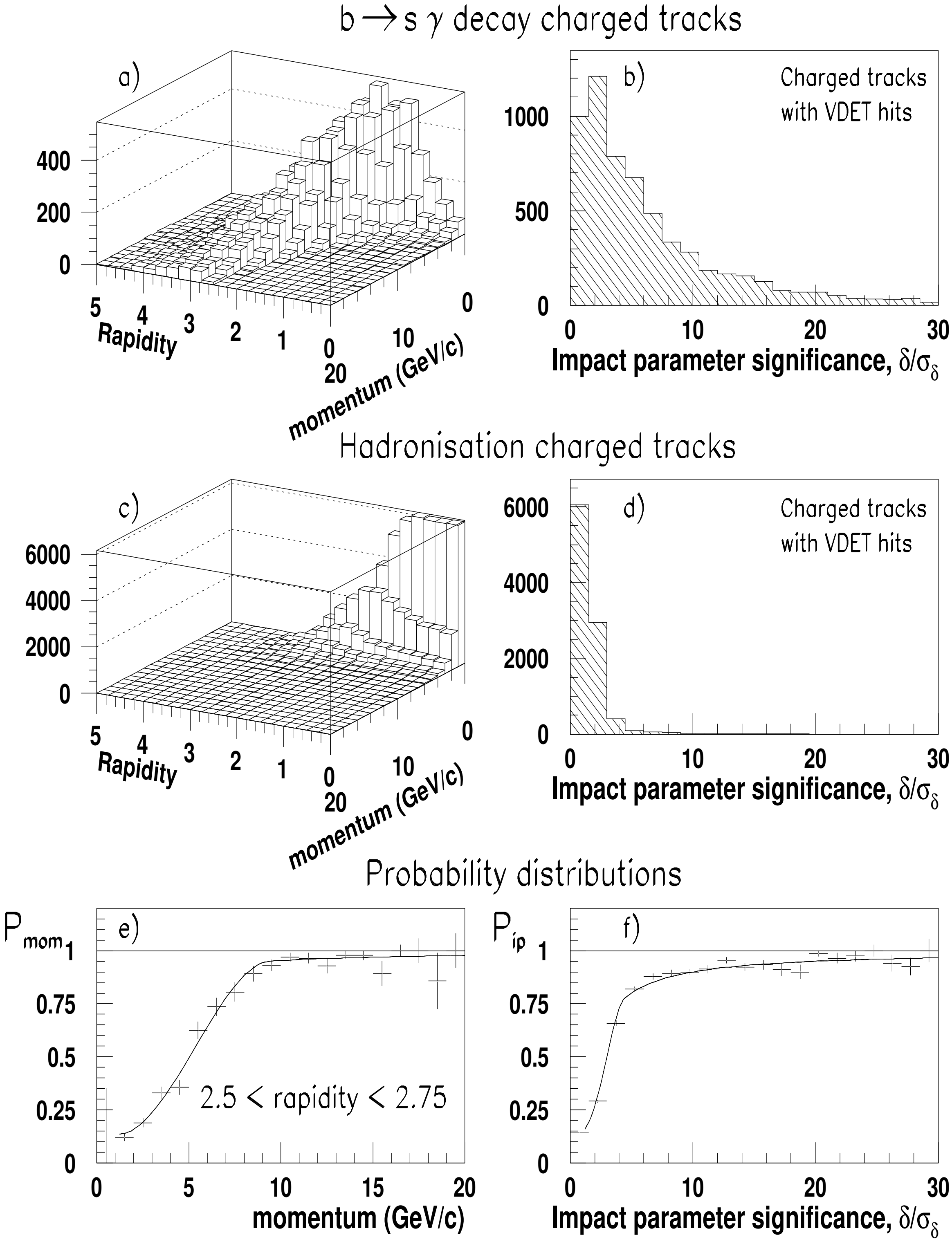

Figure 5.2: *The momentum-rapidity (a) and impact parameter significance (b) distributions for signal charged tracks and the corresponding hadronisation charged track distributions (c) and (d). Plot (e) shows the momentum probability distribution in the rapidity bin, 2.5 < rapidity < 2.75, and (f) shows the total charged track impact parameter significance probability distribution. The curves in (e) and (f) are the fitted parameterisations.*

1. An initial estimate of the b hadron vector is obtained by using only those tracks with rapidity (with respect to the thrust vector) greater than 1.0 and then calculating the probabilities as a function of momentum and impact parameter significance only.

2. The four-momenta of the candidate photon and its accompanying high rapidity tracks are then summed and used as an estimate of the b hadron flight direction with which a better estimate of the track rapidities can be made. The above process is then repeated but with the rapidity cut removed and the momentum probability function replaced by a two-dimensional momentum-rapidity probability function.

5.6 Jet selection

The reconstructed jets in events passing the event preselection cuts must also satisfy certain requirements which are represented graphically in figure 5.3 and discussed below. Jets are accepted as possible penguin b hadrons if the jet mass is within 0.7 GeV/c^2 of the mean B meson mass of 5.28 GeV/c^2, the X_s mass is less than 4.0 GeV/c^2, and the X_s track multiplicity (K^0_S and π^0 mesons, charged tracks and neutral calorimeter objects) is greater than one and less than eight. These requirements have little effect on the signal efficiency, but the X_s mass cut does remove much of the combinatorial background due to π^0 mesons produced in hadronisation. Table 5.1 shows the efficiencies for each exclusive $b \to s\gamma$ decay channel after the jet selection cuts [2]. The inclusive signal efficiency is $\approx$ 33%. Table 5.2 gives the acceptances for data and background Monte Carlo events after the cuts. The acceptances are still inconsistent although the total acceptances for data and Monte Carlo are consistent with each other at this stage.

[2] Note that the efficiency for the baryonic penguin Monte Carlo sample is significantly less than for the other, mesonic, channels. No attempt is made in the jet reconstruction algorithm to reconstruct Λ baryons and assign them their correct mass of 1116 MeV/c. Thus there was no special $b \to s\gamma$ track probability function calculated for Λ baryons. More often than the mesonic penguins, the *reconstructed* X_s has a track multiplicity of one and fails the jet selection.

Channel	N_0	N_1	N_6	N_7	Efficiency(%)
$K^*(892)$	5118	4970	2271	1717	34.55 ± 0.83
$K_1(1270)$	5027	4913	2270	1768	35.99 ± 0.86
$K_1(1400)$	5046	4928	2268	1748	35.47 ± 0.85
$K^*(1410)$	5155	5020	2250	1713	34.12 ± 0.82
$K_2^*(1430)$	5130	5000	2378	1788	35.76 ± 0.85
$K(n\pi)$	9166	8946	4035	2995	33.48 ± 0.61
$\phi(1020)$	602	586	281	209	35.67 ± 2.47
$h_1(1380)$	630	620	321	247	39.84 ± 2.53
$f_1(1420)$	647	638	294	233	36.52 ± 2.39
$\phi(1680)$	489	475	203	158	33.26 ± 2.65
$f_2'(1525)$	630	611	285	204	32.38 ± 2.27
$KK(n\pi)$	1082	1045	484	352	33.68 ± 1.80
$\Lambda(1116)$	5099	4863	2226	1040	21.39 ± 0.66
$\Rightarrow b \to s\gamma$					33.40 ± 0.29

Table 5.1: *The numbers of $b \to s\gamma$ Monte Carlo events passing the jet selection. This table is essentially a continuation of table 4.1. The first column lists the Monte Carlo penguin decay channels. N_0 is the number of events generated for each channel. N_1 is the number of events passing the standard* ALEPH *hadronic event selection. N_6 is the number of events passing the event preselection cuts of chapter 4. N_7 is the number of events passing the jet selection cuts. The final column gives the signal efficiency (here defined as N_7/N_1) for each channel after these cuts.*

Events	N_1	N_6	N_7	Acceptance(%)
91 DATA	242557	10345	2149	0.89 ± 0.02
92 DATA	671264	28193	5979	0.89 ± 0.01
93 DATA	672003	28518	6244	0.93 ± 0.01
94 DATA	1724276	76116	15257	0.88 ± 0.01
95 DATA	737578	31085	6802	0.92 ± 0.01
All DATA	4047678	174257	36431	0.900 ± 0.005
92 MC $q\bar{q}$	3625191	134604	30222	0.834 ± 0.005
93 MC $q\bar{q}$	2092829	85771	18859	0.90 ± 0.01
94 MC $q\bar{q}$	3104155	137562	29343	0.95 ± 0.01
All MC $q\bar{q}$	8822175	357937	78424	0.889 ± 0.003

Table 5.2: *The numbers of events in data and the background Monte Carlo passing the jet selection. This table is essentially a continuation of table* 4.2. *The first column lists the event samples.* N_1 *is the number of events passing the standard* ALEPH *hadronic event selection.* N_6 *is the number of events passing the event preselection cuts of chapter* 4. N_7 *is the number of events passing the jet selection cuts. The final column gives the acceptance (*N_7/N_1*) for each event sample after these cuts.*

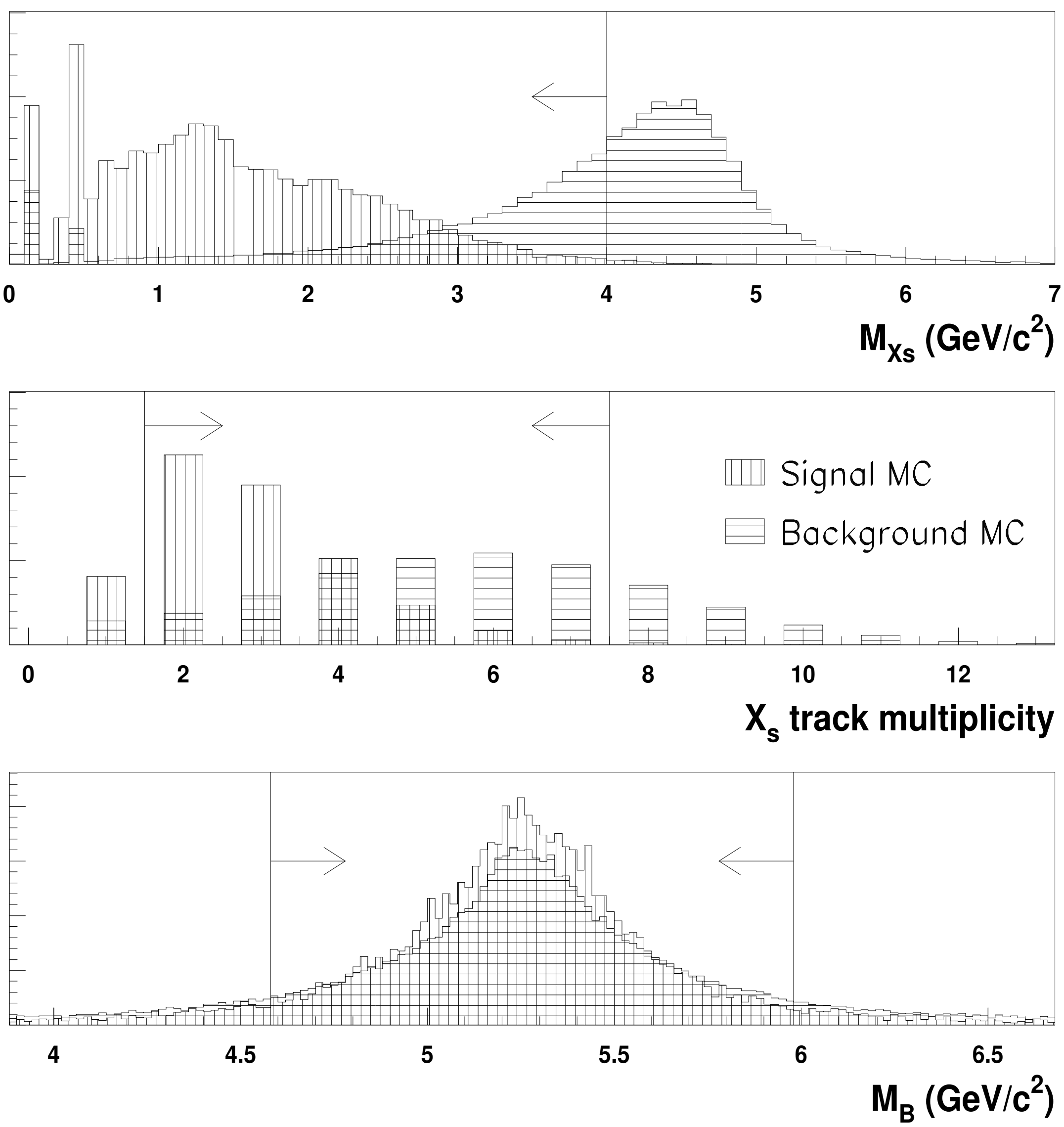

Figure 5.3: *Jet selection cuts. Signal and background Monte Carlo events are shown for each jet selection cut variable in vertical and horizontal shadings respectively, where the number of background events has been normalised to the number of signal events. The cut values in each variable are indicated by arrows defining the events which pass the cuts.*

5.7 Resolutions and reconstructed spectra

Figure 5.4 shows the residual momentum(P) distributions for penguin b hadrons reconstructed using the algorithm described in this chapter. Figures 5.5 and 5.6 show the corresponding residual angular distributions in θ and ϕ. Figures 5.7 (a), (b), and (c) show Gaussian fits to the residual distributions in P, θ and ϕ for the inclusive signal Monte Carlo model described in section 3.3. The Gaussian regions indicated on these plots contain about 73%, 67%, and 61% of the events passing the jet selection cuts, respectively. The resolutions corresponding to the fitted Gaussians in P, θ and ϕ are 1.7 GeV/c, 0.35° and 0.37° respectively. The accurate reconstruction of the b hadrons provided by this jet reconstruction algorithm enables the boost of the signal photons to be determined with good resolution. Figures 5.8 and 5.9 show the reconstructed exclusive photon energy spectra for Monte Carlo signal photons in the rest frame of the reconstructed b hadrons ($E_\gamma^\star$) and the mass spectra for the reconstructed X_s systems, (M_{X_s}) respectively. The residual distributions for $E_\gamma^\star$ are shown in figure 5.10. These distributions peak at a value close to zero but have large negative tails corresponding to a tendency to underestimate the boosted photon energy and overestimate the mass of the strange hadronic system. The $E_\gamma^\star$ resolution, corresponding to the fitted Gaussian for the inclusive model shown in figure 5.7(d), is 0.12 GeV and the Gaussian peak includes 67% of the events.

Using the jet reconstruction algorithm and applying further selection cuts, it is possible to resolve a signal for $b \to s\gamma$ in the ALEPH data. This is the subject of the next chapter.

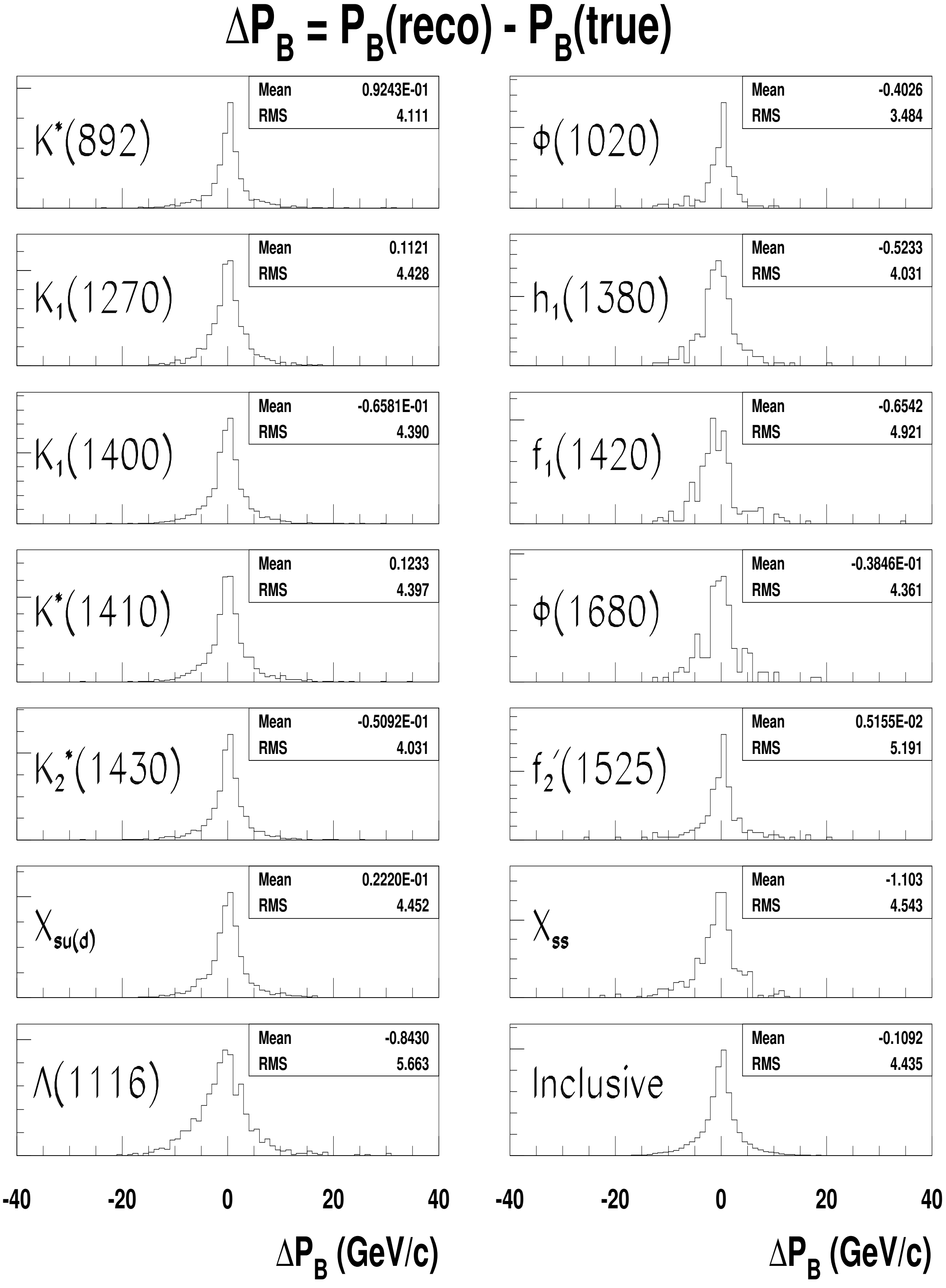

Figure 5.4: *Signal Monte Carlo reconstructed b hadron residual momentum distributions. The residual momentum is defined as the reconstructed b hadron momentum minus the true b hadron momentum. There is a distribution for each simulated exclusive penguin decay channel and the combined inclusive model.*

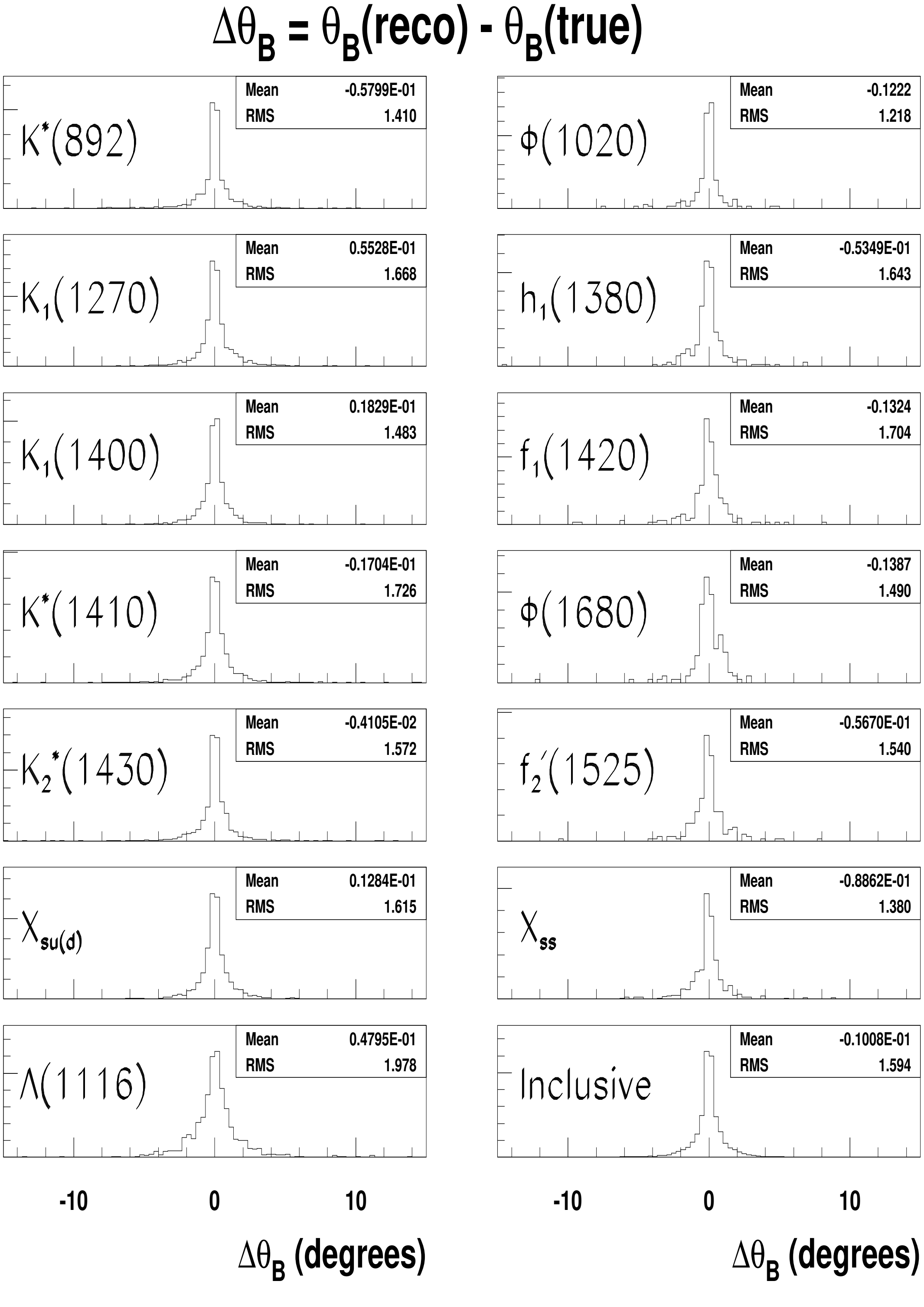

Figure 5.5: *Signal Monte Carlo reconstructed b hadron residual polar angle distributions. The residual polar angle is defined as the reconstructed b hadron polar angle minus the true b hadron polar angle. There is a distribution for each simulated exclusive penguin decay channel and the combined inclusive model.*

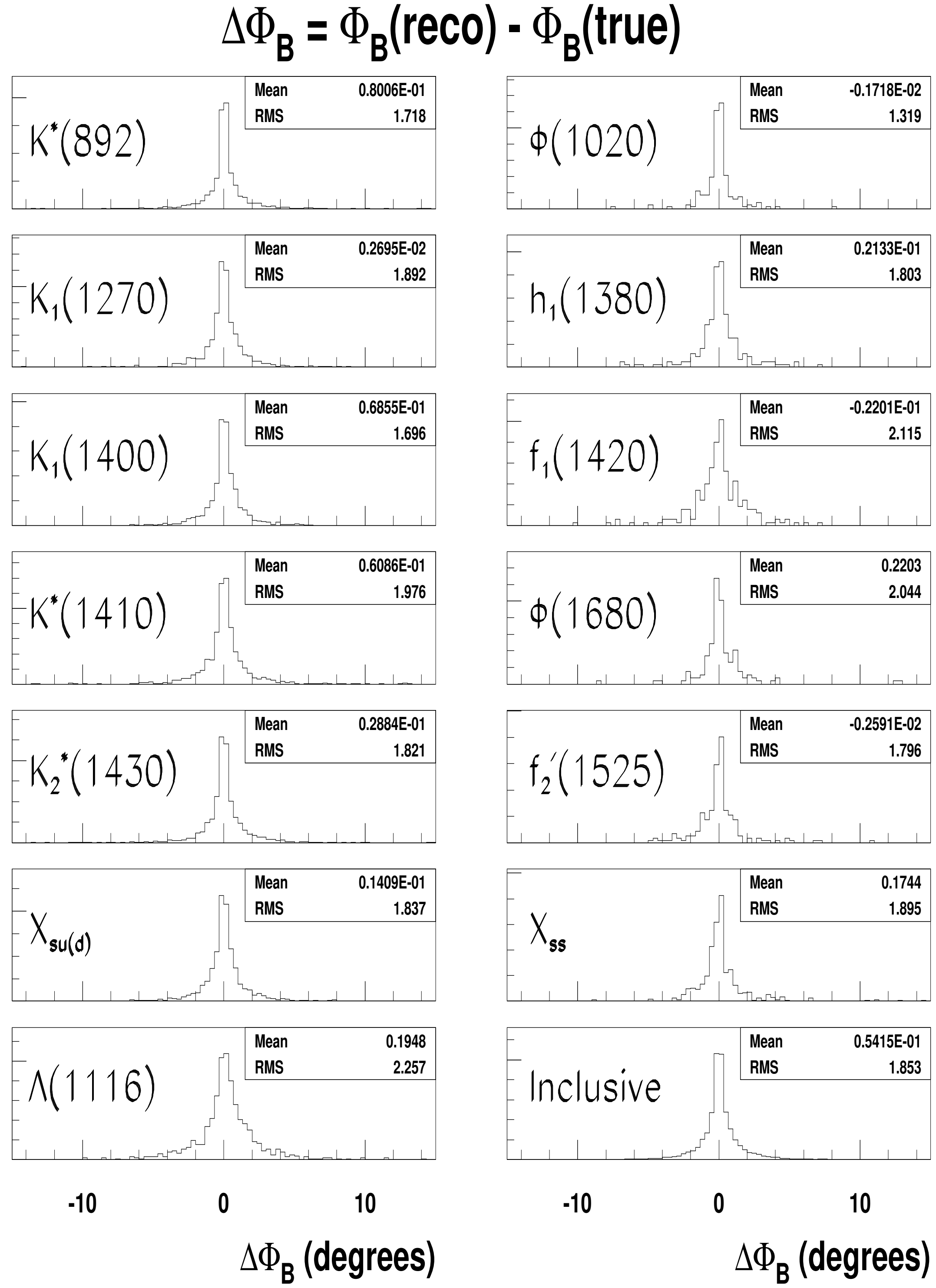

Figure 5.6: *Signal Monte Carlo reconstructed b hadron residual azimuthal angle distributions. The residual azimuthal angle is defined as the reconstructed b hadron azimuthal angle minus the true b hadron azimuthal angle. There is a distribution for each simulated exclusive penguin decay channel and the combined inclusive model.*

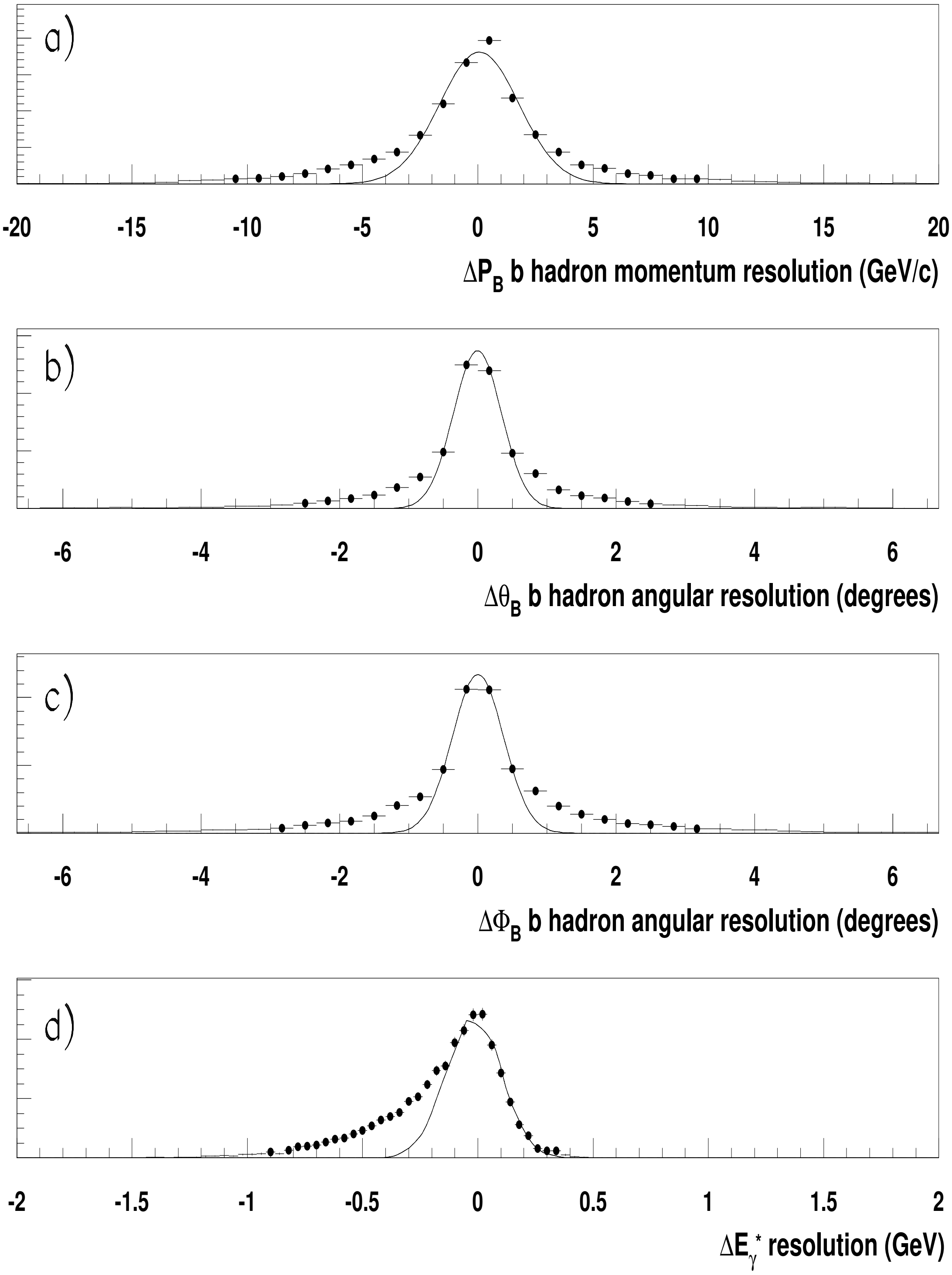

Figure 5.7: *Penguin b hadron resolutions. The central regions of the residual distributions in P, θ, ϕ and $E^{\star}_{\gamma}$ for the inclusive signal Monte Carlo model are fitted with Gaussians. The resolutions are then given by the sigma parameter values resulting from the fits.*

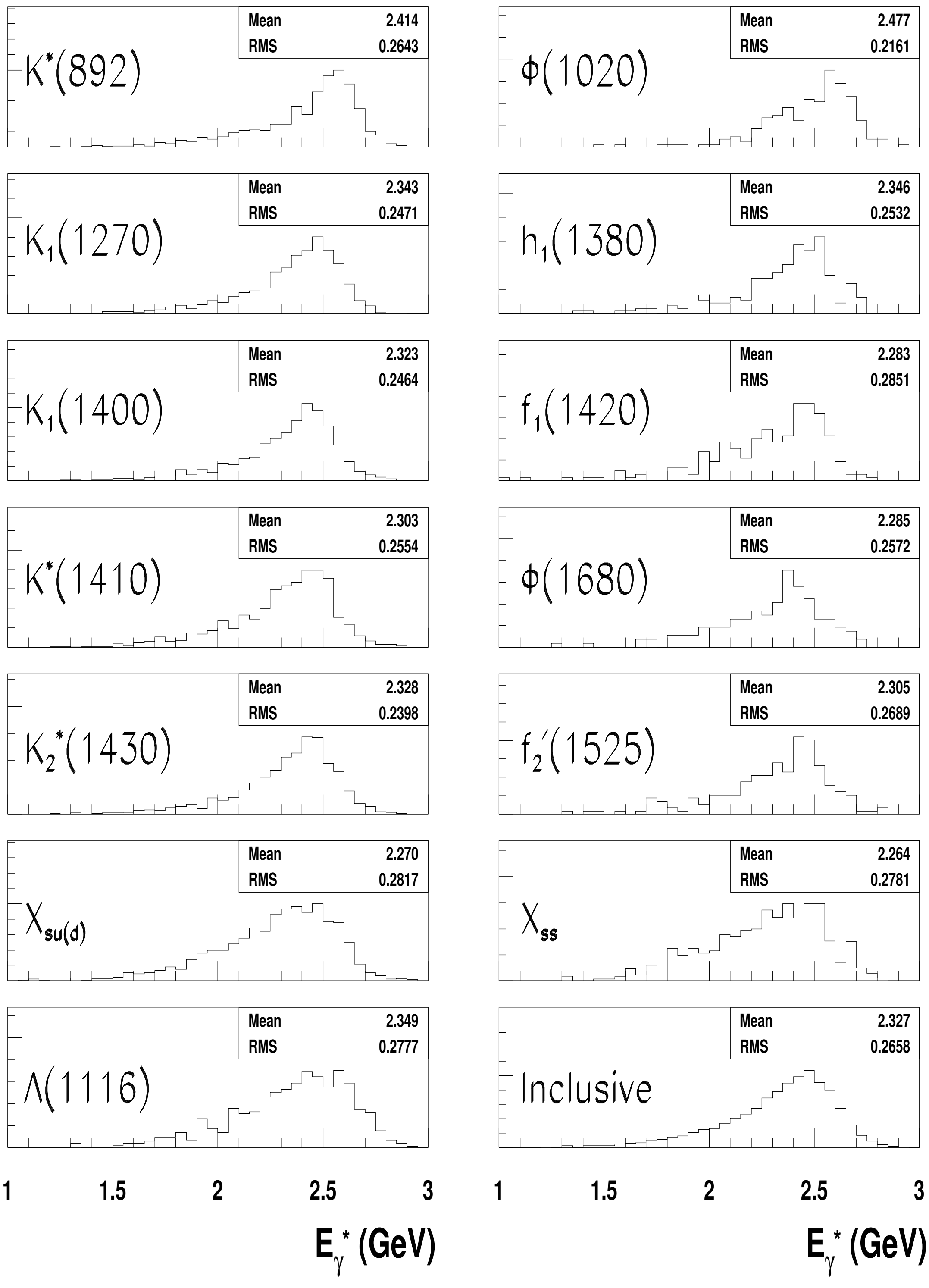

Figure 5.8: *Reconstructed $b \to s\gamma$ $E^\star_\gamma$ distributions. There is a distribution for each simulated exclusive penguin decay channel and the combined inclusive model.*

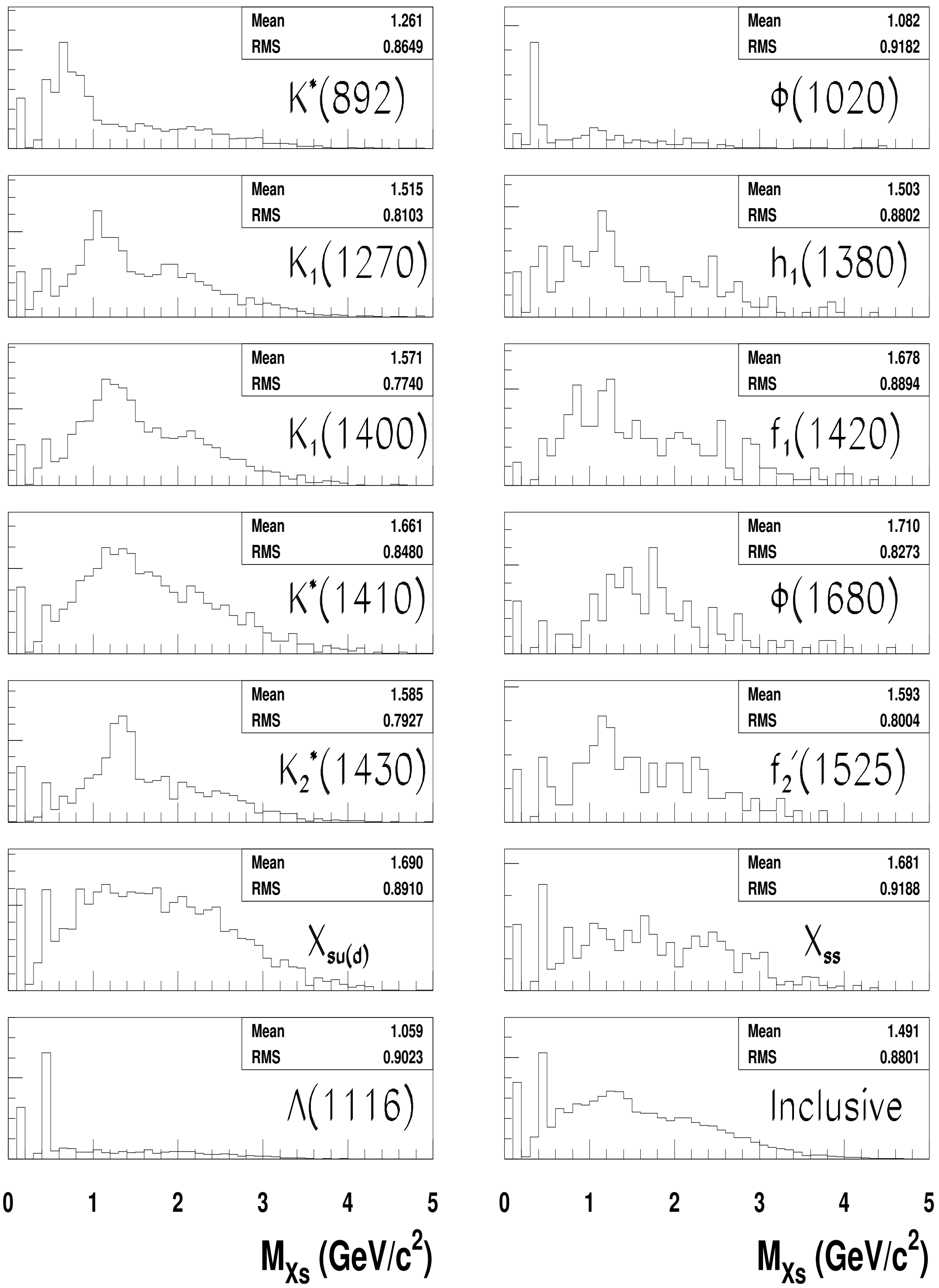

Figure 5.9: *Reconstructed $b \to s\gamma$ M_{X_s} distributions. There is a distribution for each simulated exclusive penguin decay channel and the combined inclusive model.*

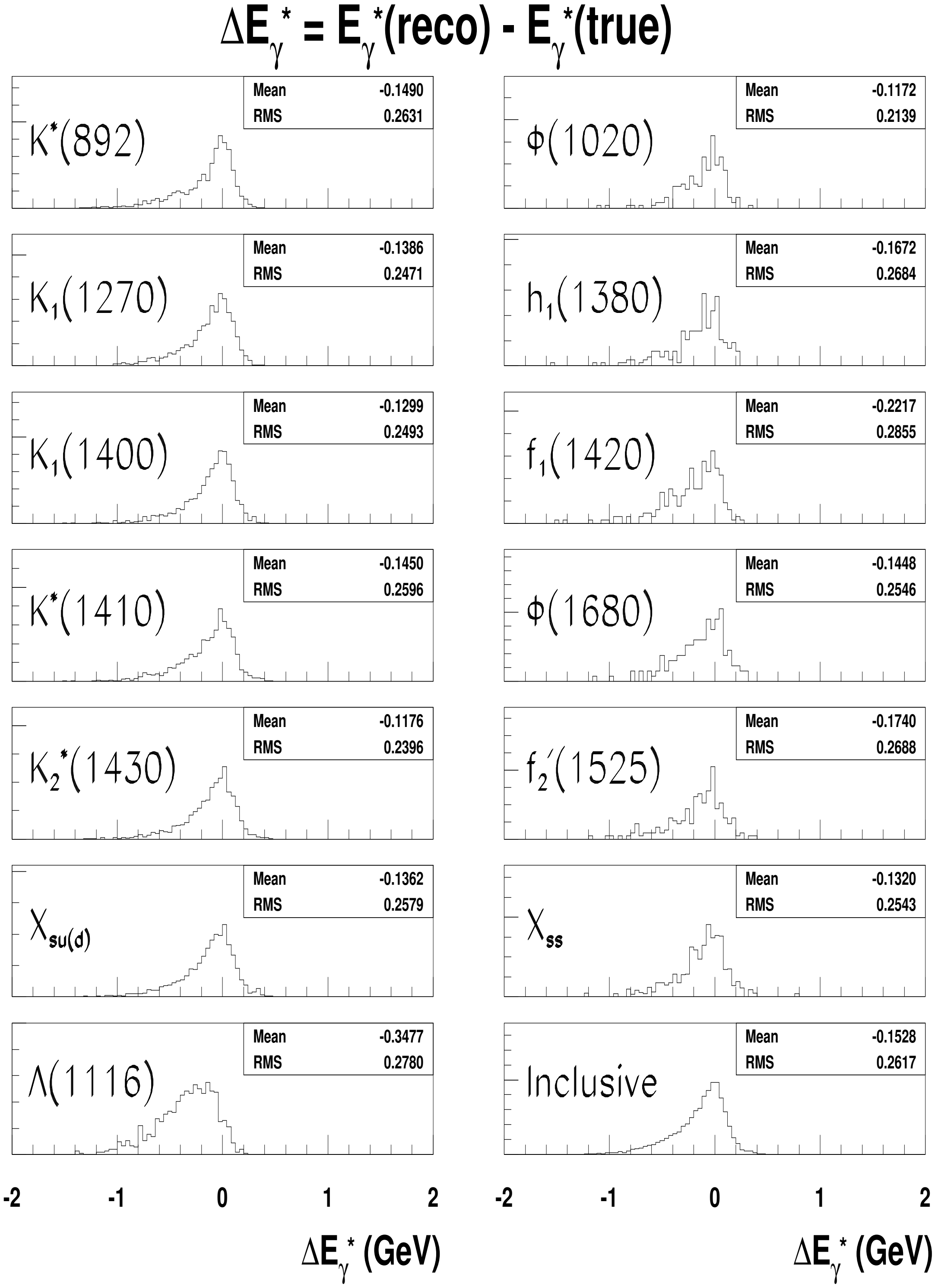

Figure 5.10: *Reconstructed $b \to s\gamma$ $E^{\star}_{\gamma}$ resolutions. There is a distribution for each simulated exclusive penguin decay channel and the combined inclusive model.*

Chapter 6

Measurement of $Br(b \to s\gamma)$

6.1 Introduction

This chapter describes the final event selection which enables a signal for $b \to s\gamma$ penguin decays to be observed in the ALEPH data — above the remaining background processes — and a branching ratio to be measured. A multivariate fit to the remaining data is performed using a combination of signal and background Monte Carlo events. The results of the fit are presented along with the measured branching ratio for $b \to s\gamma$ and, finally, systematic uncertainties on the result are calculated.

6.2 Final event selection

The requirements made thus far of a candidate photon have been described in chapters 4 and 5. The candidate photons must now pass some loose cuts on a quantity gleaned from a moments analysis of ECAL clusters. This quantity, which is described below, is an integral part of the fit for $Br(b \to s\gamma)$ where it is used to distinguish between photons and unresolved π^0 mesons. The final requirements made of the reconstructed jets ensure that only jets with decay topologies resembling that of $b \to s\gamma$ remain. The background and signal Monte Carlo event samples, described in chapters 2 and 3 respectively, are used to find a set of cuts which gives the best balance between signal acceptance and background rejection. The optimal cut values are used in the final event selection and also to define the binning in the multivariate fit which follows.

6.2.1 The story so far

The initial event preselection was described in chapter 4 where events are first required to pass the standard ALEPH hadronic event selection; contain enough good tracks for the impact parameter tag algorithm to work; and be well contained within the ALEPH detector. These hadronic events are then required to contain at least one candidate photon, which does not share its calorimetry cluster with any other object; cannot be combined with any other photon in the same event to give an invariant mass less than 0.2 GeV/c^2; and has an energy (E_γ) greater than 4.75 GeV. The opposite hemisphere to the photon is required to have an impact parameter tag probability (P_{hem}^{opp}) of less than 0.125 resulting in an event sample enriched in $b\bar{b}$ pairs. More event selection requirements were detailed in chapter 5, which described the jet reconstruction algorithm that attempts to build a jet from a candidate photon by combining it with tracks in the same event hemisphere. Only events containing reconstructed jets which satisfy the following criteria are accepted: the mass of the hadronic system accompanying the photon in the jet must be less than 4.0 GeV/c^2; the aforementioned system must contain greater than one, but less than eight, tracks; and the jet as a whole must have a mass between 4.58 GeV/c^2 and 5.98 GeV/c^2.

6.2.2 Moments analysis of ECAL clusters

When low energy π^0 mesons decay into two photons within ECAL they produce two separate energy depositions, or clusters. At higher energies, however, the photons produced in π^0 meson decays result in overlapping energy depositions in ECAL and a single cluster. Thus the spatial energy distribution of a photon cluster in ECAL is roughly circular, whereas π^0 mesons produce more elliptical distributions — see figure 6.1. A measure of how elliptical the spatial energy distribution of ECAL clusters is provided by the ALEPH cluster moments analysis [27] which uses a technique devised by Bulos [39]. This technique provides a means to identify π^0 mesons and resolve the positions of the photon impacts in the cluster.

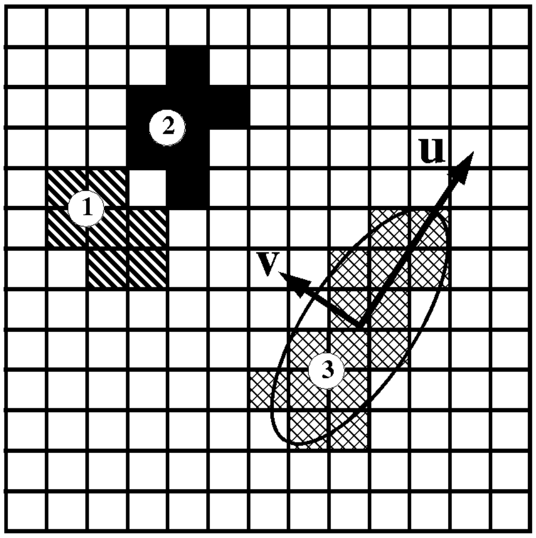

Figure 6.1: *An illustration of the difference between the energy distributions in electromagnetic clusters arising from photons and those from unresolved π^0 mesons. There are three clusters: 1 and 2 represent a π^0 meson which has been resolved into two photons while 3 is an unresolved π^0 meson. The major and minor axes u and v resulting from a cluster moments analysis are shown for cluster 3, where the axes pass through the barycentre of the cluster.*

For each cluster, the following quantities are first calculated:

$$\underbrace{E_{Total} = \sum_{i=1}^{n} E_i}_{Zeroth\ order\ moment}$$

$$\underbrace{\bar{x} = \frac{\sum_{i=1}^{n} x_i E_i}{E_{Total}} \qquad \bar{y} = \frac{\sum_{i=1}^{n} y_i E_i}{E_{Total}}}_{First\ order\ moments}$$

$$\underbrace{\overline{xy} = \frac{\sum_{i=1}^{n} x_i y_i E_i}{E_{Total}} \qquad \overline{x^2} = \frac{\sum_{i=1}^{n} x_i^2 E_i}{E_{Total}} \qquad \overline{y^2} = \frac{\sum_{i=1}^{n} y_i^2 E_i}{E_{Total}}}_{Second\ order\ moments\ of\ the\ energy\ distribution}$$

where x_i, y_i are the coordinates in the ALEPH coordinate system of the ith storey in the cluster, E_i is the energy of the ith storey, and E_{Total} is the total energy of the n storeys in the cluster. From these quantities, the major and minor axes, u and v, in the cluster can be calculated, along with the major and minor variances, λ_l and λ_s, by diagonalising the matrix of second order moments of the energy distribution:

$$\begin{pmatrix} \overline{x^2} - \bar{x}^2 & \overline{xy} - \bar{x}\bar{y} \\ \overline{xy} - \bar{x}\bar{y} & \overline{y^2} - \bar{y}^2 \end{pmatrix}$$

The eigenframe of the cluster is defined by the two eigenaxes, u and v. The eigenaxes pass through the barycentre of the cluster, and for a cluster containing two photon impacts, the impact positions must lie on the major axis. The eigenvariances, λ_l and λ_s are given by:

$$\lambda_l = (\overline{x^2} - \bar{x}^2)\cos^2\phi + 2(\overline{xy} - \bar{x}\bar{y})\sin\phi\cos\phi + (\overline{y^2} - \bar{y}^2)\sin^2\phi$$

and

$$\lambda_s = (\overline{x^2} - \bar{x}^2)\sin^2\phi - 2(\overline{xy} - \bar{x}\bar{y})\sin\phi\cos\phi + (\overline{y^2} - \bar{y}^2)\cos^2\phi$$

where

$$\phi = \frac{1}{2}\arctan\left(\frac{2(\overline{xy} - \bar{x}\bar{y})}{(\overline{x^2} - \bar{x}^2) - (\overline{y^2} - \bar{y}^2)}\right)$$

is the angle required to rotate from the ALEPH coordinate system to the eigenframe of the cluster. The rms deviations, or sigmas, of the major and minor axes are then defined as $\sigma_l = \sqrt{\lambda_l}$ and $\sigma_s = \sqrt{\lambda_s}$, respectively. The quantity σ_l is used to bin the data in the multivariate fit described below. The optimum cut on this quantity for the rejection of π^0 mesons is found to be $\sigma_l < 2.3$ cm, and this cut defines the two bins in σ_l — as shown in figure 6.2. In the final event selection, however, σ_l is merely required to be between 0.5 cm and 4.0 cm in order to reject candidate photons which resemble neither true photons nor unresolved π^0 mesons.

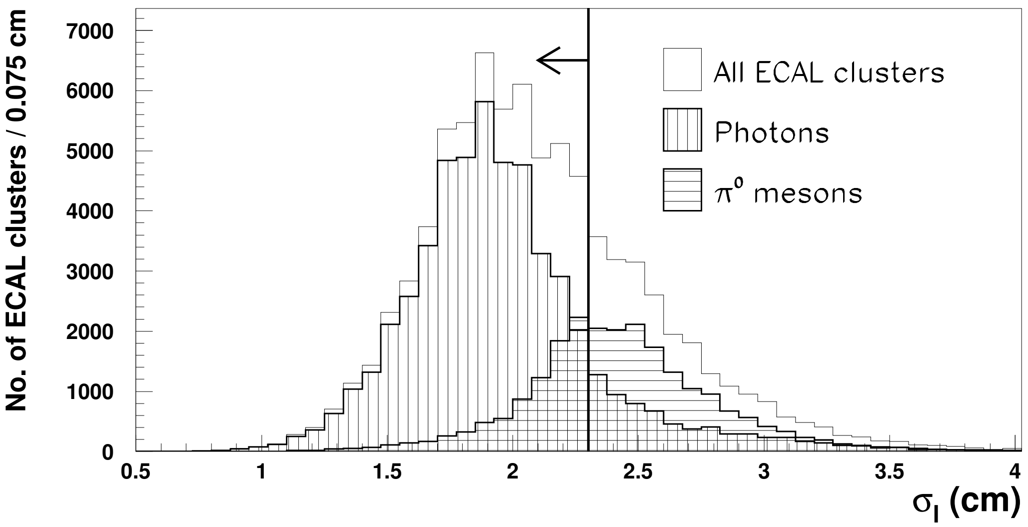

Figure 6.2: *The rms deviation along the major axis of the* ECAL *cluster energy distribution for each candidate photon in the standard (background) Monte Carlo which passes the cuts described in chapters* 4 *and* 5*. The candidate photons which are truly photons are shown, along with those which are actually unresolved π^0 mesons. The optimum pair of bins to separate π^0 mesons and photons is indicated by a vertical line with an arrow defining the bin containing the most true photons. This binning is used in this analysis to fit for the normalisation of the π^0 background.*

6.2.3 Topological selection variables

In a $b \to s\gamma$ decay, the b hadron decays into a high energy photon and a low mass strange hadronic, X_s, state, giving a distinctive decay topology. During Monte Carlo studies of both signal $b \to s\gamma$ events and background $q\bar{q}$ events, various topological selection variables were tested. The variables which are used in the final analysis are listed and explained below:

- E_{jet} is the reconstructed jet energy. E_{jet} is higher for $b \to s\gamma$ jets than for background jets containing a photon (produced in background processes such as final state radiation) and a group of tracks in the same hemisphere. The jet reconstruction algorithm described in chapter 5 is designed to reconstruct the b hadrons in $b \to s\gamma$ decays so the signal E_{jet} distribution has the form of the b quark fragmentation function.

- S_b is the sphericity of all the objects making up the reconstructed jet — including the candidate photon — in the rest frame of the jet. S_b peaks at zero for signal b hadrons since the X_s and the photon are back-to-back in the b hadron (or b jet) rest frame, whereas the S_b distribution for background jets is very broad.

- ${\theta_\gamma}^\star$ is the angle between the photon direction in the reconstructed jet's rest frame and the direction of the reconstructed jet. Penguin photons are isotropic, because B-mesons are spinless, so the $\cos\theta_\gamma^\star$ distribution is flat for signal photons but peaks at one for background photons.

6.2.4 Optimising cuts using Monte Carlo events

To observe a signal of $b \to s\gamma$ in the boosted photon energy spectrum, E_γ^*, a set of cuts is required which gives the best balance between signal acceptance and background rejection. The background and signal Monte Carlo samples, described in chapters 2 and 3 respectively, were used to test various combinations of cuts in order to find the best set. What needs to be maximised is: $N_{b\to s\gamma}/\sqrt{N_{BG}}$, where

$N_{b\to s\gamma}$ is the number of signal events passing the cuts and N_{BG} is the number of background events which pass the cuts and lie in the signal region of E^*_γ. Now, although the boosted photon energy distributions for most of the background processes are peaked at low E^*_γ values and fall away at higher energies, final state radiation photons, or FSR, tend to peak in the same place as signal photons due to the jet reconstruction algorithm used. Furthermore, the production rate of FSR is poorly modelled in `JETSET` — and hence the background Monte Carlo used in this analysis — and the difference between `JETSET` predictions and data varies with the choice of cuts [40]. This poses a problem of how to find an optimum set of cuts using a flawed background Monte Carlo.

To overcome the problem with FSR in the background Monte Carlo, and hence the resulting uncertainty in how N_{BG} actually varies in the data, cuts are chosen which maximise $N_{b\to s\gamma}/\sqrt{N_{FSR}}$ and $N_{b\to s\gamma}/\sqrt{N_{non-FSR}}$, where N_{FSR} and $N_{non-FSR}$ are here defined as the number of FSR and non-FSR background events, respectively, which pass the cuts and lie in the signal region of E^*_γ. The cuts on the following selection variables are varied: $\cos\theta^\star_\gamma$, S_b, E_γ, σ_l, $-\log P^{opp}_{hem}$, and E_{jet}. The signal region in $E_\gamma{}^\star$ is here defined as being between 2.2 and 2.8 GeV. The optimised sets of cuts are found to differ in only two of the varied quantities: $-\log P^{opp}_{hem}$ and E_{jet}. The final cuts chosen are: $\cos\theta^\star_\gamma < 0.55$, $S_b < 0.16$, $E_\gamma > 10$ GeV, $-\log P^{opp}_{hem} > 1.2$, and $E_{jet} < 50$ GeV which are shown in figure 6.3. The loose cuts on $-\log P^{opp}_{hem}$ and E_{jet} are chosen so that these variables can be binned and a fit performed to extract the final state radiation rate as well as the branching ratio for $b \to s\gamma$. The binning in the fit which follows is defined by the cuts which maximise $N_{b\to s\gamma}/\sqrt{N_{FSR}}$, which are the same as above except that $-\log P^{opp}_{hem} > 2.2$ and $E_{jet} > 32$ GeV. The optimum σ_l cut is found to be $\sigma_l < 2.3$ cm but this cut is not part of the event selection and is instead used, along with $-\log P^{opp}_{hem}$ and E_{jet}, to bin the data so that the background from unresolved π^0 mesons may be determined. The loose cuts on σ_l were described in the previous section.

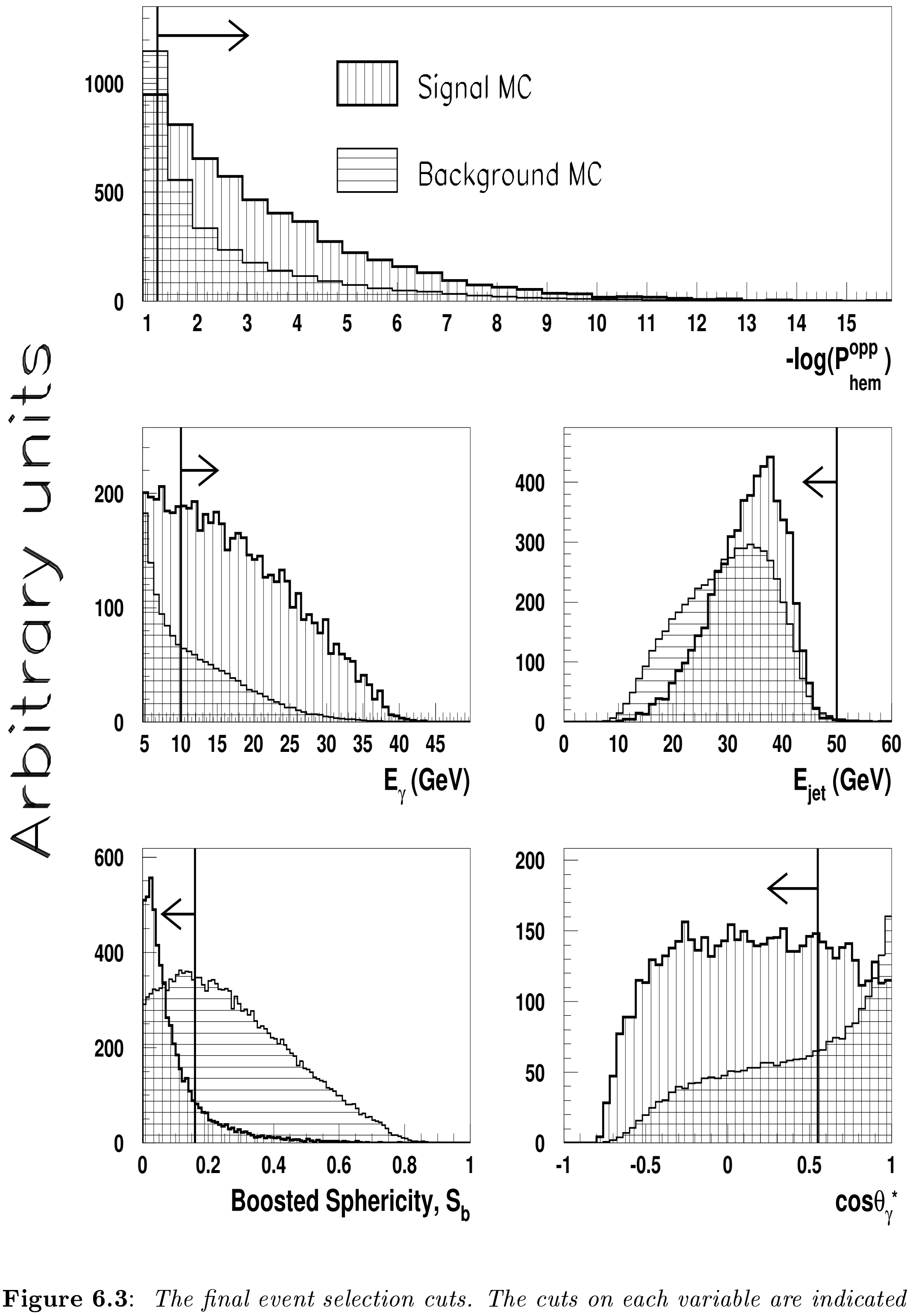

Figure 6.3: *The final event selection cuts. The cuts on each variable are indicated by vertical lines with arrows defining their acceptance. The signal Monte Carlo distributions in each variable are denoted by vertical stripes and the background Monte Carlo distributions by horizontal stripes.*

6.2.5 Final efficiencies and acceptances

The efficiencies for the various exclusive $b \to s\gamma$ channels after the final event selection are shown in table 6.1. After all the cuts, the efficiencies for each mesonic $b \to s\gamma$ decay channel are very similar but the efficiency for baryonic penguins passing the cuts is still significantly lower — for the reasons described in chapter 5. The acceptances for each data year and the background Monte Carlo event samples are given in table 6.2. The acceptances for each data year are seen to be consistent with each other after all the cuts. Similarly, the acceptances for the background Monte Carlo samples, corresponding to the detector configurations of 1992, 1993, and 1994, are shown to be consistent. The consistency of the data years is tested further by comparing the distributions in each selection variable, and the same check is performed for each background Monte Carlo event sample. The data years are found to be consistent; as are the background Monte Carlo samples. Thus, in the analysis which follows, all the background Monte Carlo events are added together and all the data events are added together.

There remain 1560 events from the original ALEPH data sample of four million hadronic Z^0 decays and 3004 background Monte Carlo events from the original sample of 8.8 million. Normalising the original number of Monte Carlo events to the original number of hadronic Z^0 decays requires a factor of 0.4588. Applying this normalisation factor to the remaining number of background Monte Carlo events gives a predicted number of 1378 background events passing the cuts. Thus there is a significant excess in the data above that predicted by the background Monte Carlo. This excess is shown in figure 6.4 for each topological cut variable and the variables used in the fit described below. The excess is particularly noticeable in the signal region of the boosted photon energy, or E^*_γ, distribution.

Channel	N_1	N_7	N_8	N_9	N_{10}	N_{11}	N_{12}	N_{13}	Eff.(%)
$K^*(892)$	4970	1717	1489	1151	1150	1149	773	726	14.61 ± 0.54
$K_1(1270)$	4913	1768	1530	1170	1167	1165	817	745	15.16 ± 0.56
$K_1(1400)$	4928	1748	1500	1115	1113	1111	735	669	13.58 ± 0.50
$K^*(1410)$	5020	1713	1501	1163	1161	1160	750	656	13.07 ± 0.51
$K_2^*(1430)$	5000	1788	1531	1132	1131	1129	779	705	14.10 ± 0.53
$K(n\pi)$	8946	2995	2543	1893	1891	1888	1289	1104	12.34 ± 0.37
$\phi(1020)$	586	209	175	143	143	143	106	104	17.75 ± 1.74
$h_1(1380)$	620	247	209	151	151	149	102	92	14.84 ± 1.55
$f_1(1420)$	638	233	207	145	145	145	103	87	13.64 ± 1.46
$\phi(1680)$	475	158	141	114	114	104	76	65	13.68 ± 1.70
$f_2'(1525)$	611	204	178	136	136	136	86	74	12.11 ± 1.41
$KK(n\pi)$	1045	352	312	245	245	245	165	141	13.51 ± 1.14
$\Lambda(1116)$	4863	1040	902	724	723	720	407	361	7.42 ± 0.39
$\Rightarrow b \to s\gamma$									12.84 ± 0.27

Table 6.1: *The numbers of $b \to s\gamma$ Monte Carlo events passing the final event selection. This table is essentially a continuation of table 5.1. The first column lists the Monte Carlo penguin decay channels. N_1 is the number of events passing the standard* ALEPH *hadronic event selection. N_7 is the number of events passing the jet selection cuts. N_8 and N_9 correspond to the numbers of events passing the final cuts on P_{hem}^{opp} and E_γ, respectively. N_{10} to N_{13} are the numbers of events passing the final stages of the event selection and correspond to the cuts on σ_l, E_{jet}, $\cos\theta_\gamma^\star$, and S_b, respectively. The final column gives the final signal efficiency (defined as N_{13}/N_1) for each channel after these cuts.*

Events	N_1	N_7	N_8	N_9	N_{10}	N_{11}	N_{12}	N_{13}	Acc.(%)
91 DATA	242557	2149	1560	760	742	740	245	89	0.037 ± 0.004
92 DATA	671264	5979	4411	2201	2135	2121	691	274	0.041 ± 0.002
93 DATA	672003	6244	4643	2277	2203	2188	698	265	0.039 ± 0.002
94 DATA	1724276	15257	11363	5472	5275	5244	1740	639	0.037 ± 0.001
95 DATA	737578	6802	5014	2454	2392	2377	796	293	0.040 ± 0.002
All DATA	4047678	36431	26991	13164	12747	12670	4170	1560	0.039 ± 0.001
92 MC $q\bar{q}$	3625191	31688	22753	11775	11653	11595	3699	1174	0.032 ± 0.001
93 MC $q\bar{q}$	2092829	18859	14388	7181	7109	7066	2271	707	0.034 ± 0.001
94 MC $q\bar{q}$	3104155	29343	21920	11054	10944	10884	3424	1123	0.036 ± 0.001
All MC $q\bar{q}$	8822175	79890	59061	30010	29706	29545	9394	3004	0.034 ± 0.001

Table 6.2: *The numbers of events in data and the background Monte Carlo passing the final event selection. This table is essentially a continuation of table* 5.2. *The first column lists the event samples.* N_1 *is the number of events passing the standard* ALEPH *hadronic event selection.* N_7 *is the number of events passing the jet selection cuts.* N_8 *and* N_9 *correspond to the numbers of events passing the final cuts on* P_{hem}^{opp} *and* E_γ*, respectively.* N_{10} *to* N_{13} *are the numbers of events passing the final stages of the event selection and correspond to the cuts on* σ_l, E_{jet}, $\cos\theta^\star_\gamma$, *and* S_b*, respectively. The final column gives the final acceptance (defined as* N_{13}/N_1*) for each event sample after these cuts.*

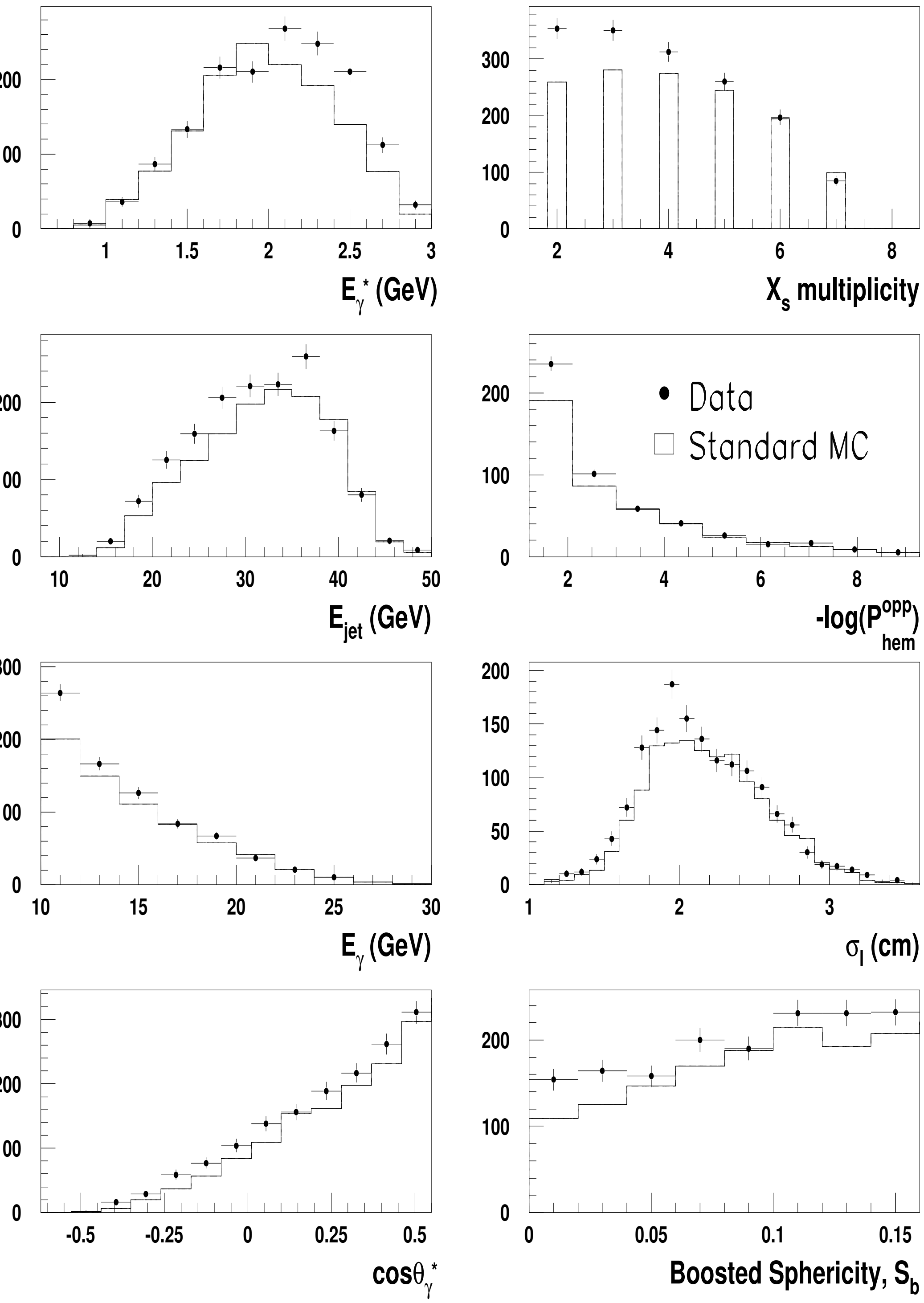

Figure 6.4: *Comparing data and MC before the fit in each cut variable and fit variable, where the standard* ALEPH *background Monte Carlo event sample is normalised to the total number of hadronic Z^0 decays in the data after the hadronic event selection — as described in the text. Note the large excess, particularly in the E_γ^* spectrum. The error bars shown are for data statistics only.*

6.3 The main sources of background

The main remaining sources of background to $b \to s\gamma$ after the final event selection — according to the standard ALEPH Monte Carlo — can be categorised as follows.

- $(b \to c)\pi^0$ events: Of the remaining background Monte Carlo events (candidate photons) 34% are due to misidentified π^0 mesons (19%), or photons from π^0 mesons (15%), produced in $b \to c$ decay chains. Of this 34%, most of the π^0 mesons are either immediate descendants ('daughters') of a b hadron or are daughters of ρ mesons which are themselves daughters of a b hadron. There is considerable uncertainty on the actual branching fractions for such decays [1] and this fact is taken into account in the fit described in the next section.

- (non$-b)\pi^0$ events: Candidate photons which are actually π^0 mesons or photons coming from π^0 mesons in non-b decays make up 29% of the background. A previous ALEPH analysis [41] found that the *inclusive* π^0 production rate in the standard background Monte Carlo is too low for high momentum π^0 mesons. Thus the normalisation of the (non$-b)\pi^0$ background is included along with the $(b \to c)\pi^0$ normalisation in the fit below.

- FSR events: Final state radiation accounts for 12% of the remaining background — just over half of which is from $c\bar{c}$ events. As discussed in section 6.2.4 there is also uncertainty in the production rate for this background, and, unlike the $(b \to c)\pi^0$ and (non$-b)\pi^0$ backgrounds, it resembles $b \to s\gamma$. Again the normalisation of this background is included in the fit below.

- $b \to u$ decays: Just under 4% of the background is due to $b \to u$ decays. Now, $b \to u$ decays account for 3% of all b decays in the standard Monte Carlo but this rate is a factor two greater than current estimates of the $b \to u$ decay rate, which can be calculated as follows:

$$\mathcal{P}(b \rightarrow u/b \rightarrow anything) = \frac{F(m_u/m_b)(\mid V_{ub} \mid)^2}{F(m_u/m_b)(\mid V_{ub} \mid)^2 + F(m_c/m_b)(\mid V_{cb} \mid)^2},$$

where V_{ub} and V_{cb} are CKM matrix elements and $F(m_u/m_b)$ and $F(m_c/m_b)$ are phase space factors. Using $\mid V_{ub}/V_{cb} \mid = 0.08 \pm 0.02$ [1] and $F(m_u/m_b)/F(m_c/m_b) \approx 7/3$ [13] in the above equation gives a value for the $b \rightarrow u$ decay rate of 1.5%. Thus, the $b \rightarrow u$ background is reweighted by a factor of 0.5 in the fit which follows.

- The rest of the background (21%) can not be so neatly categorised. Almost 19 of the remaining 21% of candidate photons are *true* photons but they are produced in many different ways. There is a small background (less than 1%) of candidate photons which are in fact η mesons. Finally, for just over 2% of the background, the true origin of the reconstructed candidate photon could not be determined from Monte Carlo truth information.[1]

[1] After the full reconstruction of ALEPH Monte Carlo events there is no one-to-one correspondence between reconstructed objects and the particles which produced them. Thus a matching routine is used to find the closest 'truth' particle, in angle and energy, to a reconstructed object but this routine occasionally fails to find a good match.

6.4 Multivariate fit

The final sample of 1560 hadronic events is split into eight sub-samples in order to separate signal and background events and fit for the fractions of data which are due to $b \to s\gamma$ decays and the three main background processes — discussed and underlined in the previous section — using the remaining Monte Carlo events. This amounts to tuning the background Monte Carlo in regions of parameter space where $b \to s\gamma$ does not occur while simultaneously fitting for the $b \to s\gamma$ branching ratio. The eight sub-samples are defined in table 6.3.

Sub-sample no.	E_{jet}(GeV)	$-\log P_{hem}^{opp}$	σ_l(cm)
1	< 32	1.0 – 2.2	< 2.3
2	32 – 50	1.0 – 2.2	< 2.3
3	< 32	> 2.2	< 2.3
4	32 – 50	> 2.2	< 2.3
5	< 32	1.0 – 2.2	> 2.3
6	32 – 50	1.0 – 2.2	> 2.3
7	< 32	> 2.2	> 2.3
8	32 – 50	> 2.2	> 2.3

Table 6.3: *Defining the sub-samples for the multivariate fit.*

The first four sub-samples are enriched with events in which the candidate photon has a lateral energy distribution consistent with that of a genuine photon, that is $\sigma_l < 2.3$ cm — see figure 6.2. Conversely, the second set of four sub-samples are mostly populated with events containing candidate photons which are actually unresolved π^0 mesons. Thus, the normalisation of background processes containing high energy π^0 mesons comes mainly from sub-samples 5 to 8.

The data are further divided into sub-samples of relatively high or low b-purity, containing jets of relatively high or low energy, in order, primarily, to separate signal photons from FSR photons, but also to distinguish between π^0 mesons produced in b hadron decays and other (non-b) π^0 mesons. Figure 6.5 (a) shows the E_{jet} distributions in Monte Carlo for signal and FSR after the final event selection. The $b \to s\gamma$ jets have an energy spectrum determined by the b quark fragmentation function, whereas the FSR jets, which consist of a FSR photon combined with a 'random' combination of tracks, have a broad energy distribution peaked at a lower energy. Figure 6.5 (b) shows the $-\log P_{hem}^{opp}$ distributions in light quark (u, d, s), charm and beauty events after the cuts. Since the FSR photons are mostly from $c\bar{c}$ events after the final event selection, $-\log P_{hem}^{opp}$ helps to further distinguish between FSR and $b \to s\gamma$. Finally, the eight sub-samples are also binned in $E_\gamma^\star$, the quantity which has most power to separate a $b \to s\gamma$ from background processes.

The $E_\gamma^\star$ plots for the first four, photon-enriched, sub-samples are shown in figure 6.6 for data, the standard Monte Carlo and the FSR background predicted by the standard Monte Carlo. The agreement between data and Monte Carlo below $E_\gamma^\star$ of 2.0 GeV is good but above 2.0 GeV there is a clear excess in data in each plot which is interpreted as being due to a combination of $b \to s\gamma$ events and an underestimated FSR background. In the plot for sub-sample no. 4, where there is very little FSR, there is still an excess, indicating the presence of the $b \to s\gamma$ signal. The $E_\gamma^\star$ plots for the second set of four, π^0-enriched, sub-samples are shown in figure 6.7 for data and the standard Monte Carlo. In these plots the standard Monte Carlo does not fit the data very well, particularly in sub-sample 8 which suggests that there are too many (non-b) π^0 mesons in the standard Monte Carlo, but there is no suggestion of an excess in the data above 2.0 GeV which would fake a $b \to s\gamma$ signal.

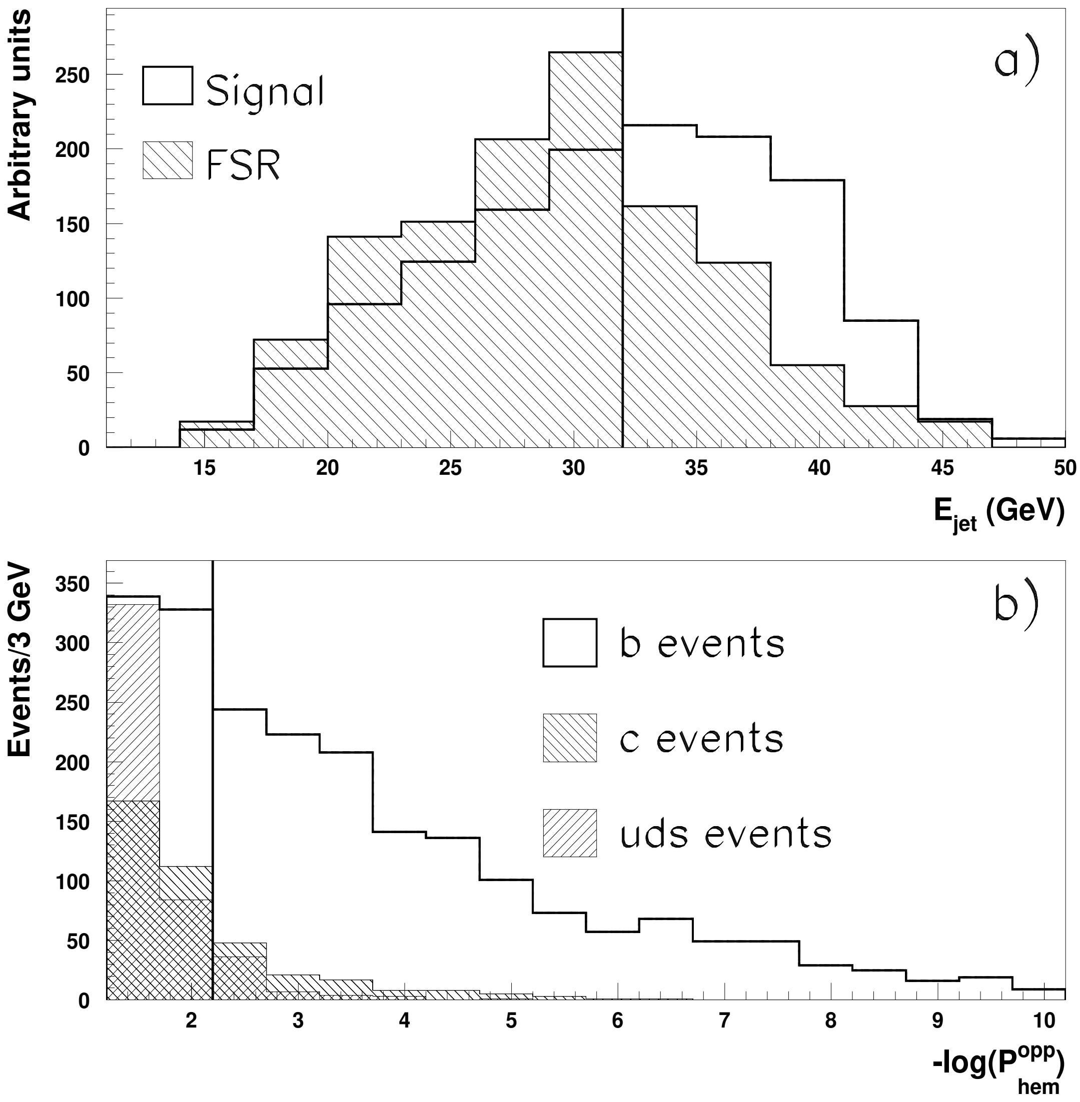

Figure 6.5: *The quantities used in the multivariate fit to separate signal events from FSR background: (a) shows the Monte Carlo E_{jet} distributions for signal and FSR and (b) shows the $-\log P^{opp}_{hem}$ distributions in light quark (u, d, s), charm and beauty events after the final event selection. Note that the normalisations in the E_{jet} distributions are arbitrary. The two vertical lines at $E_{jet} = 32$ GeV and $-\log P^{opp}_{hem} = 2.2$, along with the binning in σ_l shown in figure 6.2, define the eight event sub-samples used in the multivariate fit.*

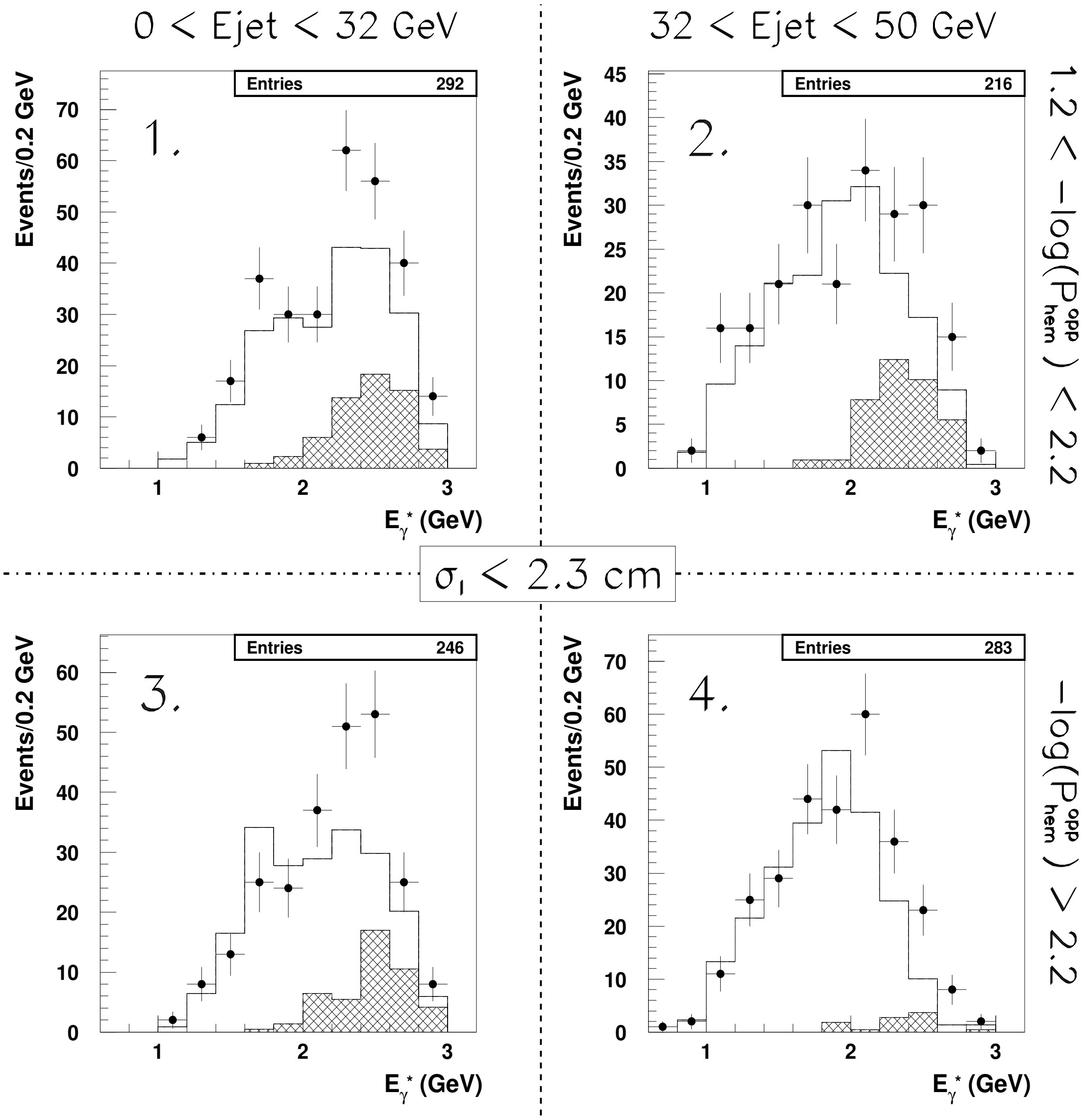

Figure 6.6: *The $E^\star_\gamma$ distributions in data (error bars) and the standard background Monte Carlo (solid histograms) — before the fit — for the first four, photon-enriched, sub-samples. The shaded distributions show the FSR component of the background predicted by the standard Monte Carlo. The error bars shown only include the statistical uncertainty on the data points.*

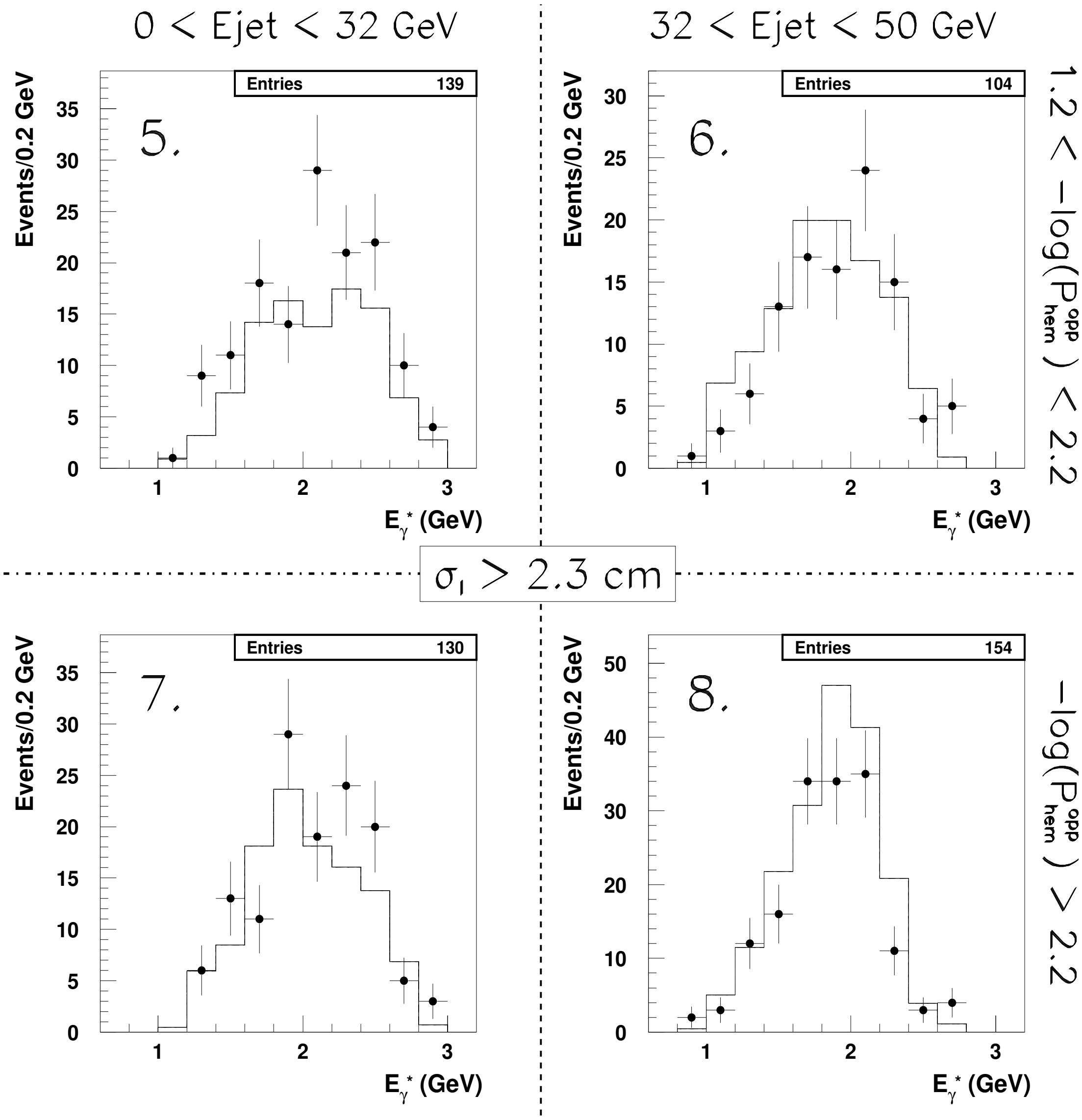

Figure 6.7: *The* $E^\star_\gamma$ *distributions in data (error bars) and the standard background Monte Carlo (solid histograms) — before the fit — for the second set of four,* π^0*-enriched, sub-samples. The error bars shown only include the statistical uncertainty on the data points. Note the particularly poor agreement between data and Monte Carlo in plot* 8*.*

The `HMCMML` fitting package [42] is used in this analysis. `HMCMML` performs binned log-likelihood fits using input Monte Carlo histograms to fit data histograms — while correctly incorporating the uncertainties due to the finite Monte Carlo statistics in each bin — and using `MINUIT` [43] to maximise the log-likelihood function. The eight data distributions are fitted simultaneously in a four parameter, binned log-likelihood fit. The four parameters in the fit are $N_{b\rightarrow s\gamma}$, N_{FSR}, $N_{(b\rightarrow c)\pi^0}$ and $N_{(\mathrm{non}-b)\pi^0}$, which are, respectively, the total number of signal, FSR, $(b \rightarrow c)\pi^0$, and $(\mathrm{non}-b)\pi^0$ background events which make up the remaining data. The shapes of the $E^\star_\gamma$ distributions are taken from the standard Monte Carlo and the other sources of background are assumed to be correctly modelled with their normalisation fixed at 0.4588. The sensitivity of the fit to $b \rightarrow s\gamma$ enters mainly through sub-sample no. 4 where there is very little FSR expected. According to the background Monte Carlo, the b purity in sub-sample no. 4 is 96.6%.

6.5 Results

The results of the multivariate fit are shown in table 6.4. A non-negligible amount of $b \rightarrow s\gamma$ is required to fit the data and the background Monte Carlo requires correction. The fitted value of N_{FSR} is 1.57 $\pm$ 0.22 times larger than that predicted by the standard Monte Carlo. The fitted value of $N_{(b\rightarrow c)\pi^0}$ decays is (31.3 $\pm$ 13.1) % lower than that predicted by the standard Monte Carlo. The fitted value of $N_{(\mathrm{non-b})\pi^0}$ decays is (46.1 $\pm$ 17.8) % higher than that predicted by the standard Monte Carlo.

The inclusive $b \rightarrow s\gamma$ branching ratio is evaluated as follows :

$$Br(b \rightarrow s\gamma) = \frac{N_{b\rightarrow s\gamma}}{\varepsilon_{b\rightarrow s\gamma}} \cdot \frac{1}{2\, N_{had}\, R_b}$$

where $\varepsilon_{b\rightarrow s\gamma}$ is the efficiency with which inclusive $b \rightarrow s\gamma$ decays pass the final event selection and is given in table 6.1; N_{had} is the number of hadronic events in the data after the standard ALEPH hadronic event selection; and R_b is the $Z \rightarrow b\bar{b}$ hadronic branching fraction which is set to its Standard Model value of 0.2158 [44]. The resulting branching ratio and its total (data plus Monte Carlo)

Fit parameter	Standard (normalised) MC value	Fitted value
$N_{b\to s\gamma}$	0	70.23 ± 20.4
N_{FSR}	165.6 ± 8.7	260.7 ± 36.9
$N_{(b\to c)\pi^0}$	473.0 ± 14.7	324.7 ± 59.4
$N_{(\mathrm{non-b})\pi^0}$	400.1 ± 13.5	584.7 ± 71.0
Fixed parameter	Standard (normalised) MC value	Fixed value
N_{other}	315.7 ± 12.0	315.7 ± 12.0

Table 6.4: *Results of the four parameter fit to the data: The first column gives the number predicted by the standard Monte Carlo when normalised to the initial number of hadronic events in the data sample. The second column gives the corrected values resulting from the multivariate fit.*

statistical error are :

$$Br(b \to s\gamma) = (3.14 \pm 0.92) \times 10^{-4}.$$

The $E^\star_\gamma$ plots for the first four, photon-enriched, sub-samples are shown in figure 6.8 for data and the *corrected* Monte Carlo. The $E^\star_\gamma$ plots for the second set of four, π^0-enriched, sub-samples are shown in figure 6.9 for data and the corrected Monte Carlo. The χ^2 for the fit is 58.5 for 63 degrees of freedom, where only bins with at least four entries are included in the χ^2 calculation. Figure 6.10 (a) shows the combined E^*_γ distribution for sub-samples 2 and 4 (as defined in section 6.4) in data and Monte Carlo after the normalisations of the background processes have been corrected. The remaining excess is interpreted as a signal for $b \to s\gamma$ and is shown in figure 6.10 (b) with the fitted distribution superimposed. Figure 6.11 compares data and Monte Carlo after the fit in each of the variables used in the analysis. The agreement in each variable is significantly improved, compared with figure 6.4.

If, however, $b \to s\gamma$ events are not included in the fit, the excess in the data remains. It can not be accounted for by a fit which just involves some combination of the background sources.

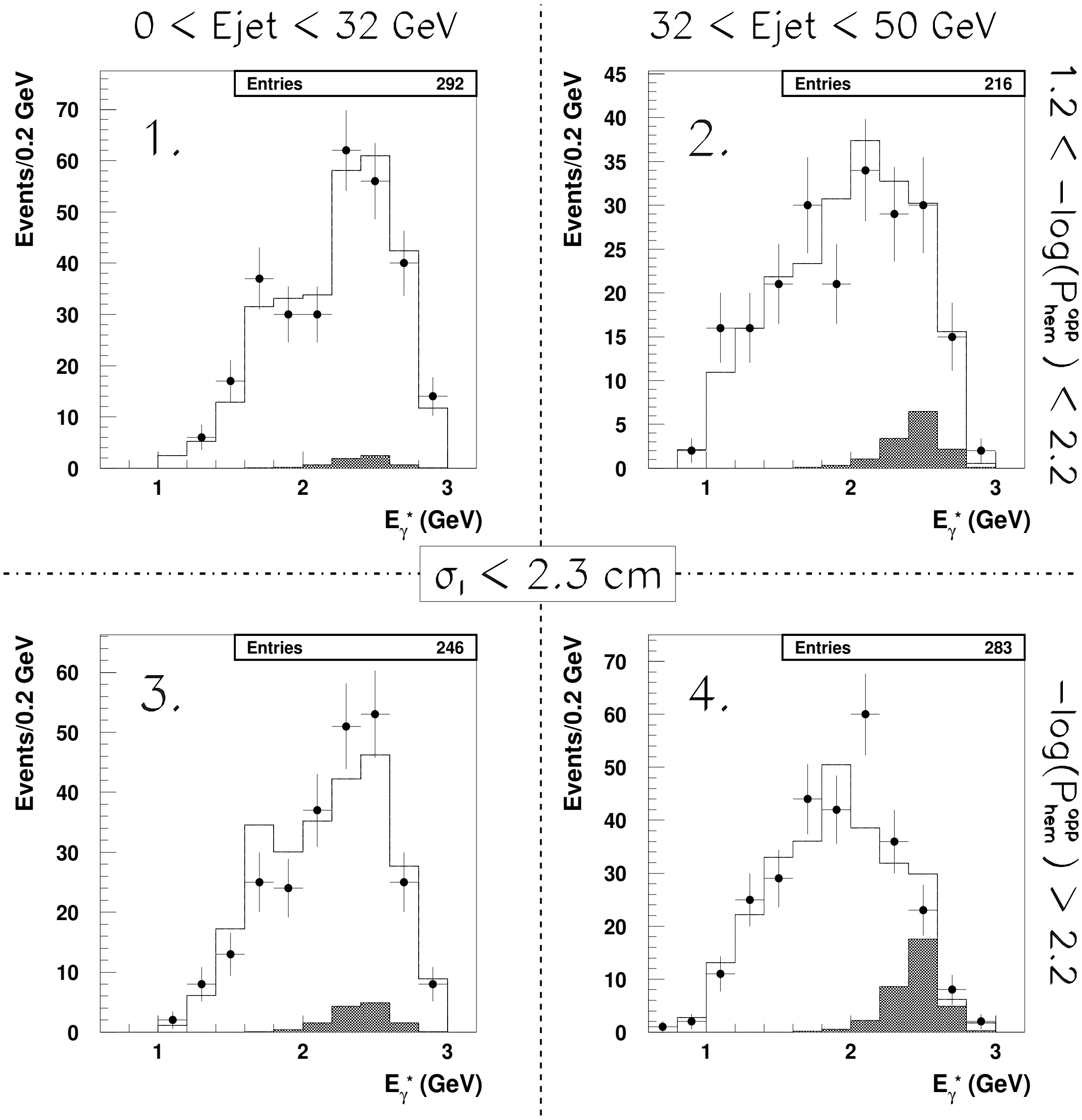

Figure 6.8: *The $E^\star_\gamma$ distributions in data (error bars) and the corrected background Monte Carlo (solid histograms) — after the fit — for the first four, photon-enriched, sub-samples. The shaded distributions show the $b \to s\gamma$ component of the corrected Monte Carlo. The error bars shown only include the statistical uncertainty on the data points.*

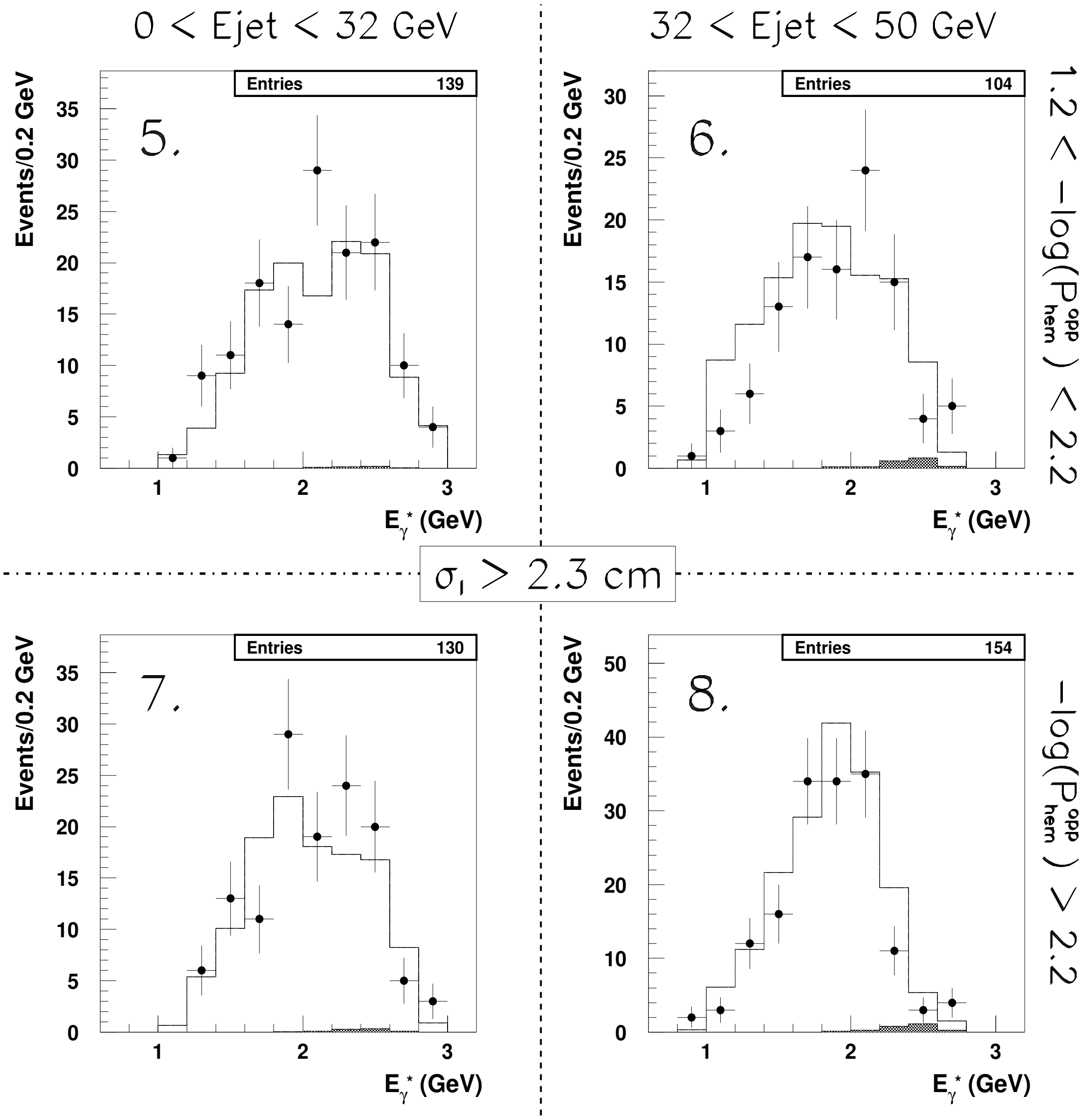

Figure 6.9: *The $E^\star_\gamma$ distributions in data (error bars) and the corrected background Monte Carlo (solid histograms) — after the fit — for the second set of four, π^0-enriched, sub-samples. The error bars shown only include the statistical uncertainty on the data points. Note in particular the improved agreement between data and Monte Carlo in plot* 8.

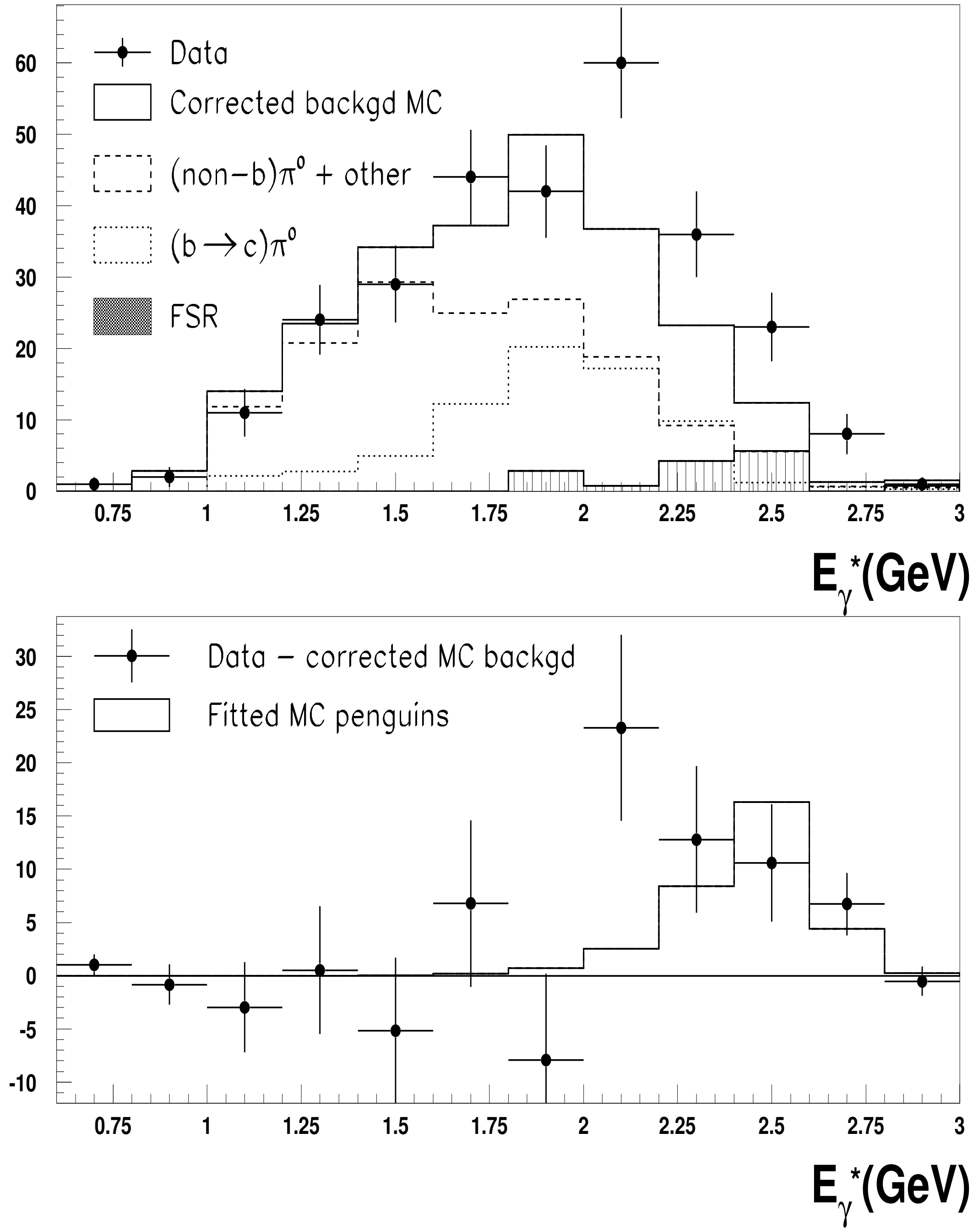

Figure 6.10: *A signal of $b \to s\gamma$ where E^*_γ is the energy of a photon in the rest frame of the reconstructed jet. The top figure shows the data and Monte Carlo background events in the combined sub-samples* 2 *and* 4 *(see section* 6.4*), after the correction of the background processes' relative normalisations. The bottom figure shows the excess in data after subtraction of the corrected Monte Carlo background and the signal distribution resulting from the multivariate fit.*

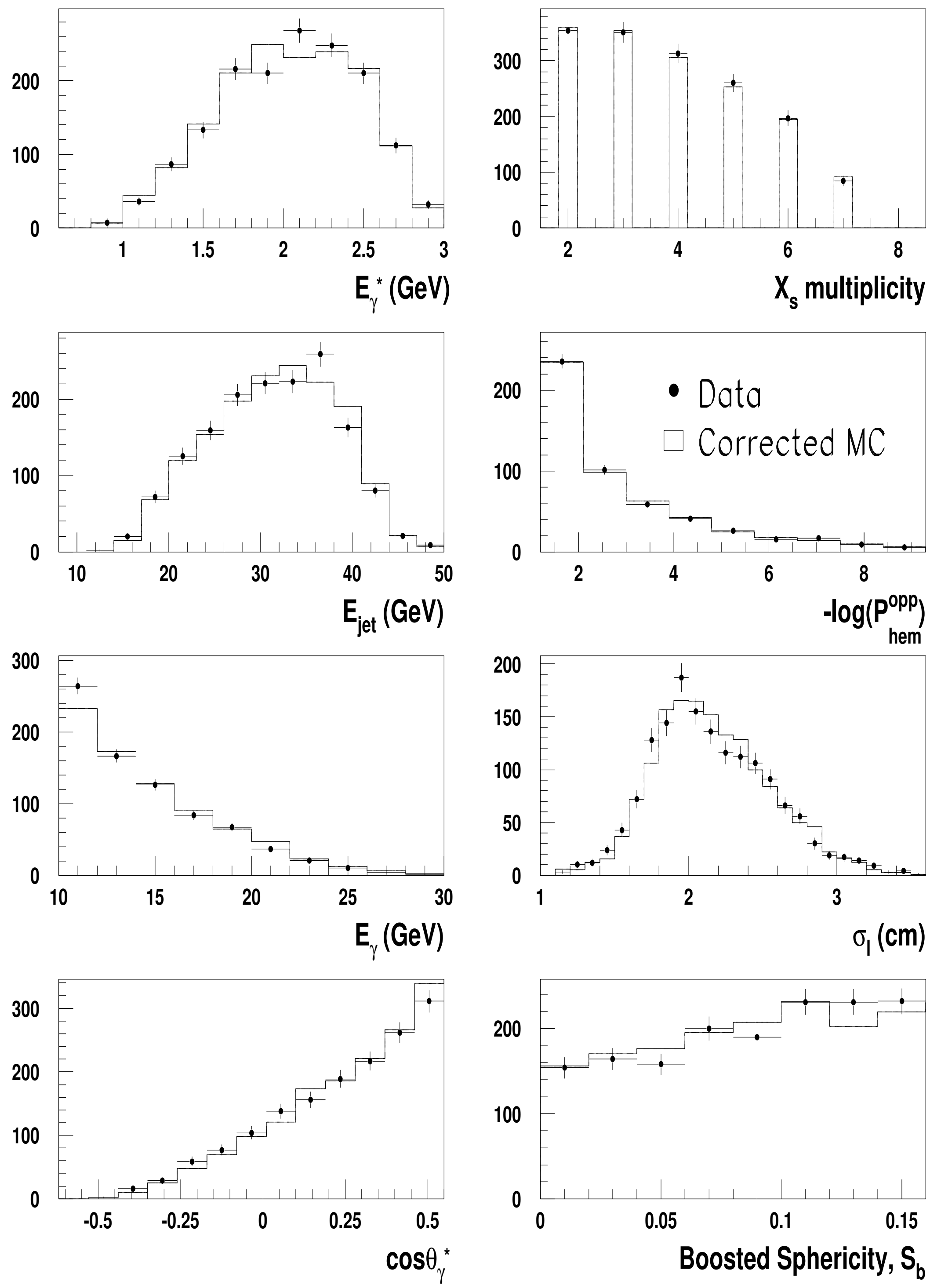

Figure 6.11: *Comparing data and Monte Carlo events after the fit in each cut variable and fit variable, where fitted penguins have been added to the corrected* ALEPH *background Monte Carlo. The error bars shown are for data statistics only.*

6.6 Statistical and systematic errors

Table 6.5 gives a breakdown of the statistical and systematic errors on the branching ratio measurement. The methods used to evaluate these errors are described below, where each error is referred to by its label in the table.

	Source of uncertainty	Error ($\times 10^{-4}$)
Δ_1	Signal Monte Carlo statistics	0.002
Δ_2	FSR normalisation (from fit)	0.345
Δ_3	$(b \to c)\pi^0$ normalisation (from fit)	0.150
Δ_4	$(\mathrm{non}-\mathrm{b})\pi^0$ normalisation (from fit)	0.091
Δ_5	'Other' background normalisation (statistical)	0.007
Δ_6	$b \to u$ decay rate	0.209
Δ_7	Exclusive $b \to s\gamma$ branching fractions	0.196
Δ_8	Fraction of baryonic $b \to s\gamma$ decays	0.215
Δ_9	b quark Fermi momentum	0.030
Δ_{10}	B meson production fractions	0.009
Δ_{11}	Assumption for $B_s \to X_{ss}\gamma$ exclusive branching fractions	0.007
Δ_{stat}	Data statistics — $\Delta_{stat} = \sqrt{\Delta_{fit}^2 - \sum_{i=1}^{4} \Delta_i^2}$	0.83
Δ_{sys}	Total systematic error — $\Delta_{sys} = \sqrt{\sum_{i=1}^{11} \Delta_i^2}$	0.53
Δ_{tot}	Total error — $\Delta_{tot} = \sqrt{\Delta_{stat}^2 + \Delta_{sys}^2}$	0.98

Table 6.5: *Uncertainties on the $Br(b \to s\gamma)$ measurement. Note that Δ_{fit} is the total statistical error — data plus Monte Carlo — which comes from the multivariate fit.*

The statistical uncertainty in the branching ratio of $\Delta_{fit} = \pm\ 0.92 \times 10^{-4}$ — from the multivariate fit — can be reduced to its component parts where the errors are due to signal Monte Carlo statistics; the fitted background normalisation uncertainties; and data statistics:

- The total $Br(b \to s\gamma)$ fit error (Δ_{fit}) has a small contribution from the $b \to s\gamma$ Monte Carlo. This signal Monte Carlo statistical error is taken to be the fraction $\Delta\varepsilon_{b\to s\gamma}/\varepsilon_{b\to s\gamma}$ of Δ_{fit} and is taken to be a *systematic* error on the branching ratio measurement (Δ_1).

- The covariance matrix produced in the fit is used to extract the uncertainties in the branching ratio for $b \to s\gamma$ due to uncertainties in the three other parameters in the fit. The following procedure, described in [43], is adopted. The matrix is inverted, the row and column corresponding to the fit parameter removed, then the reduced matrix is reinverted to give a reduced error on $N_{b\to s\gamma}$. The corresponding reduced error on $Br(b \to s\gamma)$ is subtracted in quadrature from the full error (Δ_{fit}) to give the contribution from that parameter to the *Monte Carlo* statistical error, and this contribution is taken to be a *systematic* error. This procedure is carried out for the three background normalisation parameters in the fit. The resultant errors (Δ_2 to Δ_4) are added in quadrature to the signal Monte Carlo statistical error (Δ_1), and the remaining uncertainty in Δ_{fit} is assumed to be the statistical error on $Br(b \to s\gamma)$ due to the finite *data* statistics (Δ_{stat}).

There are also systematic errors due to uncertainty in the branching ratios for background processes which are not varied in the fit:

- The number of 'other' background processes, N_{other}, which was a fixed parameter in the fit, is varied within its statistical errors to see how the fit results change. The biggest resultant shift in the $Br(b \to s\gamma)$ measurement away from the 'central' value is then taken to be a systematic error (Δ_5).

- The $b \to u$ decay rate used in the fit (1.5%) is first set to zero and then to 3%, with the fit performed for both of these extreme cases. The largest resultant change in the fitted $b \to s\gamma$ branching ratio is then taken as a conservative systematic error (Δ_6).

- As can be seen from figure 6.9 there is no evidence of any unsimulated $B \to X\pi^0$ two-body decays in the data which would resemble, and be a background to, $b \rightarrow s\gamma$. Thus, it is assumed that *no systematic error* is associated with the uncertainty in $B \rightarrow X\pi^0$ two-body decays.

There are systematic errors due to theoretical uncertainty in the signal Monte Carlo composition which was described in chapter 3:

- The systematic error due to theoretical uncertainty in the relative fractions of *exclusive* penguin decays in the *inclusive* $b \rightarrow s\gamma$ model (Δ_7) is calculated by repeating the fit with two extreme signal Monte Carlo compositions and taking the largest shift in the branching ratio measurement to be the error. Firstly the fractions of resonant penguins are all increased to their upper limits — as shown in table 3.1 — while the numbers of non-resonant penguins are reduced to compensate; then the fractions of resonant penguins are all decreased to their lower limits while the numbers of non-resonant penguins are increased to compensate.

- The fit is also repeated with the fraction of baryonic $b \rightarrow s\gamma$ decays set to zero and the resulting shift (Δ_8) taken as a conservative estimate of the uncertainty in the production rate of such decays.

- The uncertainty in the production fraction of B mesons [1] is taken into account by reweighting B_u penguin decays upwards and downwards in the model — to the production fraction limits — while varying B_d penguin decays downwards and upwards, respectively, to compensate. The largest shift in the measured branching ratio is then taken as a systematic error. Similarly, B_s penguin decays are reweighted upwards and downwards while both B_u and B_d penguin decays are varied in equal proportion to compensate, and, again, the largest shift in the measured branching ratio is taken as a systematic error. These two errors are then combined in quadrature to give the systematic error due to B meson production fraction uncertainties (Δ_9).

- The photon energy spectrum in the non-resonant $B \rightarrow K(n\pi)$ decays depends on the value of the b quark Fermi momentum, P_F, used in their simulation. The central value used, 265 MeV, is changed by its error, ± 25 MeV [34], and the fit repeated. The larger change in the fitted branching ratio is then taken as a systematic error (Δ_{10}).

- A systematic error is calculated for the assumption that the exclusive B_s penguin decays are produced in the same relative fractions as the exclusive $B_{u(d)}$ penguin decays. The branching ratio is recalculated using B_s penguin decay branching fractions weighted according to their spin multiplicity [45] and the resulting shift taken as the systematic error (Δ_{11}).

In summary, the *statistical* error due to the finite data statistics (Δ_{stat}) is 0.83×10^{-4}, while adding each of the systematic errors in quadrature gives a total *systematic* error (Δ_{sys}) of 0.53×10^{-4}. It is clear from table 6.5 that the statistical uncertainties for both data and Monte Carlo dominate the result.

6.7 Stability of the $Br(b \rightarrow s\gamma)$ measurement

The stability of the branching ratio measurement is tested by repeating the analysis with a range of different cut values. The fit is repeated for three values above and three below the chosen cut value for each of the following variables: $\cos\theta^{\star}_{\gamma}$, S_b, E_γ and $-\log P^{opp}_{hem}$, which were described in section 6.2 and shown in figure 6.3. The variation about the central value of the fitted $Br(b \rightarrow s\gamma)$ for each of these cuts is shown in figure 6.12. For three of the plots only small systematic trends are visible and any change in the fitted branching ratio is much less than the quoted statistical error. The E_γ cut plot shows a more significant systematic trend over the range shown ($\pm$ 3 GeV). However, within the two sigma photon energy resolution range for 10 GeV photons of $\pm$ 1.6 GeV — see section 2.5.4 — there is an insignificant variation in $Br(b \rightarrow s\gamma)$. Thus, it is assumed that the systematic error associated with the choice of cuts is negligible.

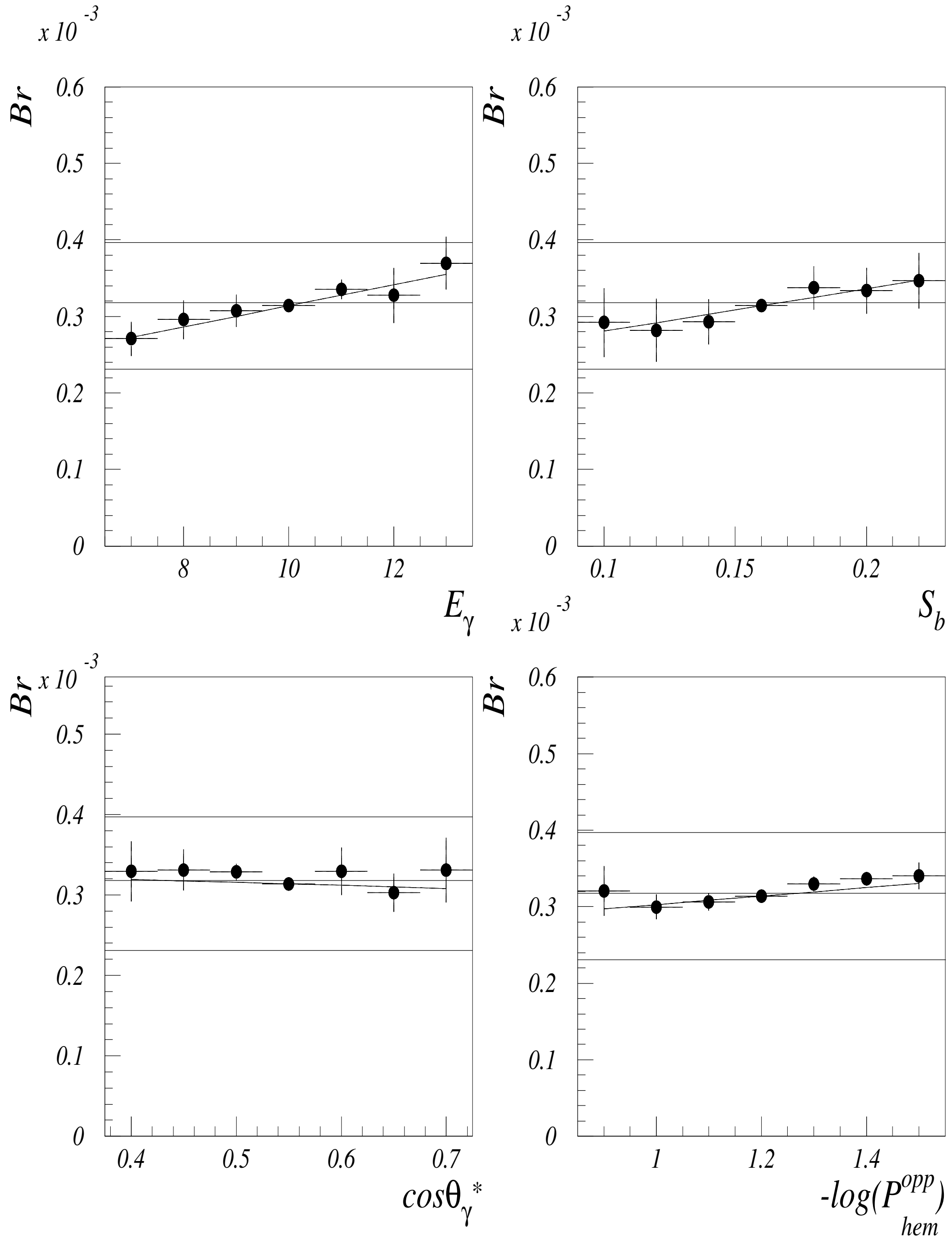

Figure 6.12: *The stability of the branching ratio measurement. The horizontal lines define the statistical error on the central measurement. The data points correspond to measurements made using different cut values. The error bars shown correspond to the fractional change in the number of signal Monte Carlo events relative to the adjacent data point multiplied by the error from the fit which produced the data point. A straight line fit is performed in each of these distributions, where the line is forced to go through the central value, and each of the other points is given equal weight.*

6.8 Supporting evidence

6.8.1 "The smoking gun"

Some supporting evidence is now given to support the assertion that the signal seen in the $E^\star_\gamma$ distribution is actually $b \to s\gamma$. Each of the three main particles involved in the decay are addressed in turn: the b, the s, and the γ:

- In sub-sample no. 4, which is expected to be the purest sample of $b \to s\gamma$ events, and in the signal region, 2.2 GeV $< E^\star_\gamma <$ 2.8 GeV, there is evidence in the remaining data events, after subtraction of the corrected background, of a secondary vertex (that is 'lifetime') in the *same* hemisphere as the photon. Figure 6.13(a) shows the $-\log P^{same}_{hem}$ distribution in data and the corrected background Monte Carlo, where P^{same}_{hem} is the hemisphere probability in the same hemisphere as the photon. The $-\log P^{same}_{hem}$ distribution, and therefore the lifetime, for the Monte Carlo background is consistent with being due to $b \to c$ decays, but the corresponding data distribution does not resemble this background and seems to contain decays with less lifetime on average.[2] Now, the lifetime in $b \to s\gamma$ decay hemispheres is *less* than in the more typical $b \to c$ decay hemispheres because there is no tertiary decay vertex. The excess of data is shown in figure 6.13(b) with the $-\log P^{same}_{hem}$ distribution for signal events plotted upon the excess data distribution, where the $b \to s\gamma$ normalisation comes from the multivariate fit. The lifetime signal in the data is seen to be consistent with that expected from $b \to s\gamma$.

- Again in sub-sample no. 4, and in the signal region of $E^\star_\gamma$, the momentum of the leading (highest momentum) identified kaon in the reconstructed jet is shown for data and the corrected background Monte Carlo in figure 6.13(c). There is seen to be an excess of high momentum kaons in the data, and, as shown in figure 6.13(d), the distribution is consistent with the expecta-

[2] According to the background Monte Carlo, the b purity in the signal region of sub-sample no. 4 is 90.4%.

tions of $b \to s\gamma$, where, again the $b \to s\gamma$ normalisation comes from the multivariate fit [3].

- Finally, on combining sub-samples no. 4 and no. 8, and once more considering only events contained within the signal region of $E^{\star}_{\gamma}$, there is seen to be a clear excess of photons in the data while there is no excess of π^0 mesons. The σ_l distribution is shown for data and the corrected background Monte Carlo in figure 6.13(e), while the excess in data is shown to be well modelled by the fitted signal Monte Carlo.

6.8.2 Exclusive channels

As well as the *inclusive* analysis described in this thesis, ALEPH has performed searches for *exclusive* $b \to s\gamma$ channels. Five $B \to K^*\gamma$ candidates [46] and one $B_s \to \phi\gamma$ candidate [47] have been isolated. All six events are correctly reconstructed using the jet reconstruction algorithm described in chapter 5. Furthermore, four of the six events (including the $B_s \to \phi\gamma$ candidate) are to be found in the 1560 data events which pass the final event selection and enter the multivariate fit. This agreement with the independent exclusive analyses shows that the reconstruction algorithm is pretty good at picking up penguins.

[3] As described in chapter 5, ${K_s}^0$ mesons are reconstructed and identified by combining pairs of oppositely charged pions. Charged kaons of high momentum are much more difficult to identify, however, as the trails of ionisation they leave in the TPC are very similar to those of electrons and charged pions. For this reason the identified charged kaons in figure 6.13(c) are required to have an ionisation trail within one standard deviation of the kaon hypothesis and greater than two standard deviations away from either the electron or pion hypothesis.

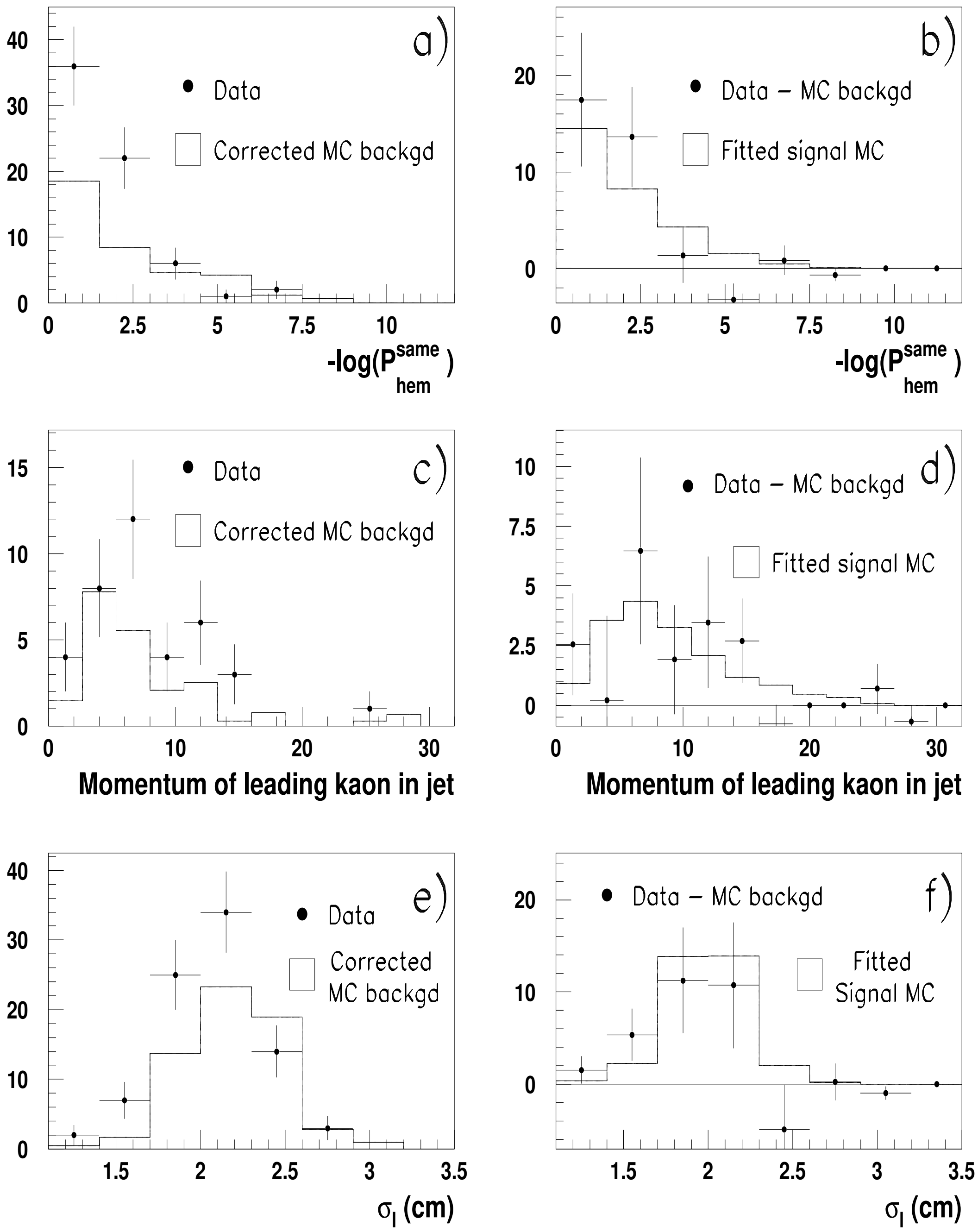

Figure 6.13: *The smoking gun plots: (a) displays the impact parameter hemisphere probability in the same hemisphere as the candidate photon for data and the corrected background Monte Carlo, while the excess of data above the background, along with the fitted signal distribution, are shown in (b). (c) and (d) show the leading kaon momentum distributions for data, background Monte Carlo and signal Monte Carlo. (e) and (f) show the* ECAL *cluster width distributions for data, background Monte Carlo and signal Monte Carlo. The events were selected as described in the text.*

6.9 Summary

In the analysis described above, an optimised event selection is used, along with a multivariate fit, to isolate a signal for $b \to s\gamma$ and measure its branching fraction. The normalisations of the major background processes are also fitted for and various systematic errors are evaluated and attached to the result. The branching ratio is found to be stable and the isolated signal is seen to be consistent with the $b \to s\gamma$ Monte Carlo predictions. The resulting branching ratio and its errors are:

$$Br(b \to s\gamma) = (3.14 \pm 0.83_{\mathrm{stat}} \pm 0.53_{\mathrm{syst}}) \times 10^{-4},$$

and the implications of this result are discussed in the next, and concluding chapter.

Chapter 7

Summary and conclusions

7.1 Summary of the $b \to s\gamma$ analysis

The inclusive branching ratio for $b \to s\gamma$, a rare electromagnetic decay of the b quark, has been measured using data taken with the ALEPH detector between 1991 and 1995. Theoretical predictions for the exclusive branching fractions and the inclusive $b \to s\gamma$ photon energy spectrum formed the basis of a model for this process, and standard Monte Carlo techniques were used to simulate $b \to s\gamma$ signal events and background $q\bar{q}$ events as they would appear in the detector (chapters 2 and 3). An initial preselection was carried out, resulting in a reduced data sample enriched in $b\bar{b}$ pairs, and containing high energy candidate photons (chapter 4). A jet reconstruction algorithm was applied to these events, with tracks being added on to the candidate photons in order of $b \to s\gamma$ probability — where the probabilities are a function of a track's energy, its rapidity with respect to the thrust axis, and, if charged, its impact parameter significance (chapter 5). A final event selection was performed using topological cuts optimised with Monte Carlo events, and the remaining data was split into eight sub-samples which were then fitted simultaneously to extract the fractions of data which are due to background processes, and the fraction which is $b \to s\gamma$. Finally, the statistical error on $Br(b \to s\gamma)$ was calculated along with various systematic uncertainties.

The result is:

$$Br(b \to s\gamma) = (3.14 \pm 0.83_{\rm stat} \pm 0.53_{\rm syst}) \times 10^{-4}.$$

This measurement is in good agreement with the Standard Model prediction for the $b \to s\gamma$ branching ratio of $(3.28 \pm 0.33)\times 10^{-4}$ and the CLEO measurement of $(2.32 \pm 0.57 \pm 0.35)\times 10^{-4}$. It is the first measurement of $Br(b \to s\gamma)$ at LEP.

7.2 Theoretical implications of the result

There are many theoretical models which are constrained by an inclusive $b \to s\gamma$ branching ratio measurement [11]. For example the experimental upper limit on the result translates directly to a theoretical lower limit on the charged Higgs mass in two-Higgs doublet models. The particle spectra in Supersymmetry is also constrained by the measured $b \to s\gamma$ rate [48]. Even supergravity models — and thereby dark matter detector rates — depend on the result [49].

7.3 Future developments

Within the next decade, with an updated measurement from CLEO and new results coming from other B factories, the experimental uncertainties on $Br(b \to s\gamma)$ will be dramatically reduced. It will be up to theorists to reduce the theoretical errors on the Standard Model prediction and that of rival models, thereby enabling adequate comparisons with experiment to be made. However, until then, there are improvements which can be made to the analysis described in this thesis; such as those listed below:

- The jet reconstruction algorithm can be made more inclusive by reconstructing Λ baryons in the candidate photon hemisphere and constructing $b \to s\gamma$ probability functions for them as is done for mesons currently.

- The event selection cuts can be reoptimised using the results of the multivariate fit in an attempt to further increase the $N_{signal}/\sqrt{N_{background}}$ ratio and reduce the statistical errors on the branching ratio measurement.

- A study of the final data sample can be carried out and a search made for various exclusive decays. Furthermore, the data could be fitted for the fraction of $b \to s\gamma$ decays that is $B \to K^*\gamma$, which is a useful quantity for theorists.

- A fit for the Fermi momentum of the b quark, P_F could be carried out as was done using the CLEO data by Ali and Greub in [50].

- Upper limits on the branching ratios for two-body decays such as $B \to X\pi^0$, $b \to d\gamma$, and $b \to c\gamma$ could be determined.

Appendix A

VDET monitoring software

A.1 Introduction

A.1.1 Penguins aside

This chapter describes the software written by the author of this thesis for ALEPH's new vertex detector. The work was begun in early 1995 and completed in time for the detector's installation in October of that year [51]. The software is currently being used to monitor the detector's performance online, as data are taken during LEP 2 running.

A.1.2 VDET

The original ALEPH silicon Vertex Detector (VDET), the first ever double-sided silicon detector (see chapter 2), was in operation from 1991 [52] to September 1995. It was built to detect the motion of those charged particles nearest the e^+e^- interaction point as they pass through the detector. The two layers of detector modules, and their double-sided silicon strip readout, enable the spatial position of such tracks to be measured with high precision, and vertices to be reconstructed in three dimensions (figure 2.3). Such precision makes it possible to identify, or 'tag', short-lived particles, such as B-mesons, and also to measure their lifetimes. However, with the increase in centre-of-mass energy of the LEP accelerator (LEP 2) scheduled for late 1995, the need for a new, more efficient, VDET was foreseen.

A.1.3 The need for a new VDET

In 1993 the ALEPH collaboration decided to replace the original VDET by an improved version for LEP 2 running. The main limitations were seen to be [53]:

- The length of the original VDET (about 20 cm) was such that only tracks between 45 degrees and 135 degrees, with respect to the z-axis, crossed both detector layers.
- The readout electronics for the z strips ran down the length of the detector and placed large amounts of material in the central angular region. Furthermore, such non-uniformly distributed material leads to difficulties in simulating the detector structure which is critical for b-tagging.
- Some of the VDET components (particularly amplifiers and AC-coupling capacitors) were found to be vulnerable to radiation. It was feared that during LEP 2 a considerable fraction of the detector electronics would fail and require replacement.

A.2 Out with the old and in with the new

A.2.1 VDET II

VDET II[1] has various features that are different from the original VDET:

- The z strips in VDET II are multiplexed and read out at the end of the detector, not along its length.

[1] From now on the new VDET will be referred to as VDET II although it is actually commonly referred to as VDET as before.

- The 48 VDET II detector modules have 1024 amplifier channels instead of 512 in the $r\phi$ view and each has three wafers instead of two, with multiplexing of the 1900 silicon strips in the z view, giving 1024 amplifier channels as before.
- The extra wafers make VDET II longer than the original VDET.
- Radiation hard MX7 amplifier chips [54] are used instead of CAMEX chips, and read in 128 channels instead of 64 for the CAMEX.
- Common mode noise calculations[2] are done for each MX7 chip unlike before when it was done for blocks of 256 channels. As with the orignal VDET, the common mode is subtracted from the data when it is processed offline.

Thus, the software for VDET had to be rewritten or adapted to take into account these changes.

A.3 ALEPH online monitoring software

The figure below (figure A.1) gives an overview of the ALEPH online monitoring system [55]. A number of monitoring tasks (yyMON) process the raw data from each subdetector into histograms which can be displayed online or offline by a 'presenter'. These histograms are analysed at regular intervals by analysis tasks (yyANL) which then report any problems to an error logger (ERRLOG). Furthermore, the histograms can be compared with reference histograms so that obvious changes in the data can be spotted by the ALEPH shift crew. A histogram database (HDB) keeps a record of all the histograms being used along with details of how they are grouped into pages and by task.

VDET II has two monitoring tasks and one analysis task, with several pages of histograms being filled and analysed during data taking. These three tasks,

[2]The pedestal-subtracted pulse height of each 'good' channel in the MX7 is entered into a histogram. Channels with no signal will have nearly the same pulse height and thus form a peak in the histogram while signal channels will lie on the upper side of this peak. The mean of this peak region corresponds then to the common mode noise of this MX7 chip.

used by ALEPH to monitor the performance of VDET II online, were written by the author of this thesis and are described in the following section.

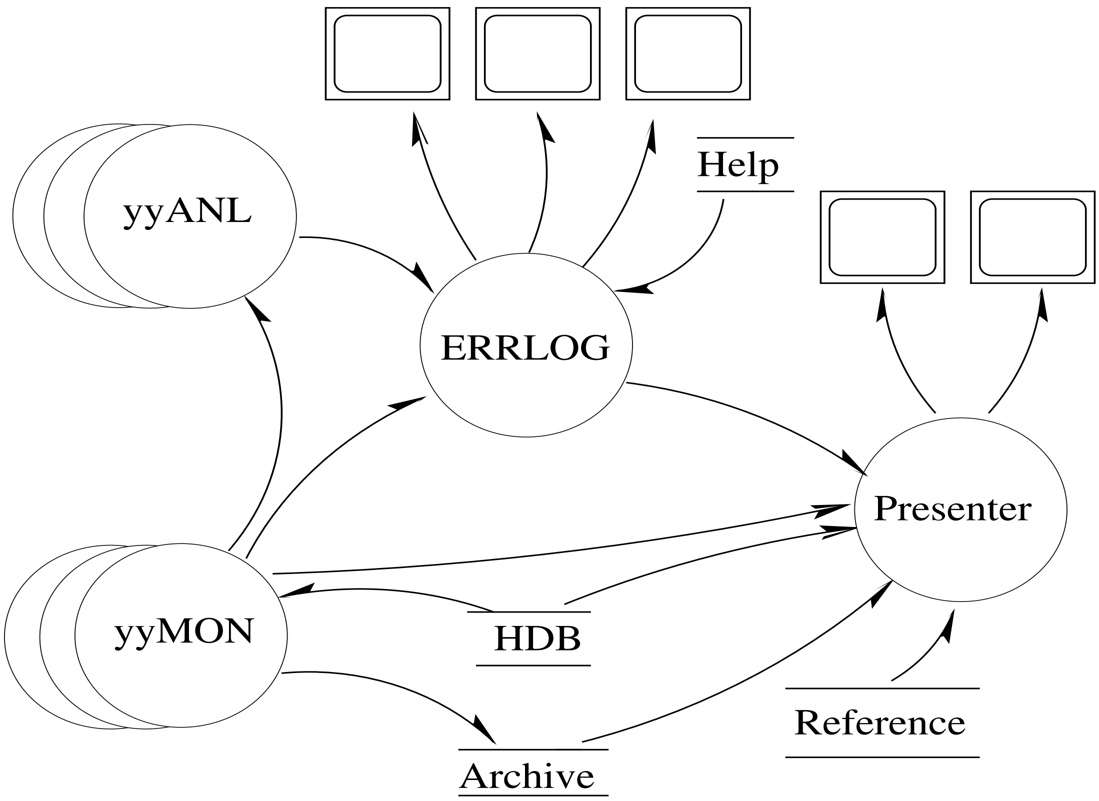

Figure A.1: *The* ALEPH *online monitoring system*

A.4 VDET online monitoring software

A.4.1 VDMON

VDMON , like all ALEPH monitoring tasks, is built upon a standard template which links to the histogram database and error logger without the programmer having to do so within his/her monitoring code. *VDMON* is designed to monitor the quality of VDET II events online; it produces histograms to be checked at the end of every run and sends error messages to the error logger console in case of any problems with the data.

When a charged particle passes through a layer of VDET II it causes electrons to flow in the silicon strips in its vicinity and this is registered by electronic pulses associated with electronic channels in a particular detector module. A group of such pulsing channels is called a cluster and data is stored for each cluster on an event-by-event basis in the form of BOS banks [56]. The important BOS banks, as far as *VDMON* is concerned, are the following:

- There is a VHLS (Vdet Hit ListS) bank available for every one of the possible 48 detector modules in VDET II where the high voltage is on. Each VHLS bank contains information pointing to where in VDET II a cluster of electronic pulses was detected if any. (VDMON ignores clusters which can not be assigned to a physical location within VDET II.)
- For each module where a cluster has been detected there is a VPLH (Vdet PuLse Heights) bank which contains information on each electronic channel in a VHLS cluster. Each electronic channel is assigned a pulse height and logical flags to say whether the channel is known to be a 'bad' one or not and whether it was in overflow or not. (VDMON ignores those channels which are flagged as 'bad' or in overflow).
- For each side of VDET II (A and B) there is a VOCM (VDET Common Mode) bank which contains the mean and root mean square values of the common mode noise for each MX7 chip.

Histograms (or NTuples) are gathered in pages available through the ALEPH presenter. There are two types of pages :

1. SHIFT PAGES — each ALEPH subdetector has one page.
2. EXPERT PAGES — each ALEPH detector can have as many pages as needed.

An example of the VDET II shift page, generated by VDMON at the end of a run, is shown in figure A.2. Each histogram has an associated help file which can be accessed through the presenter.

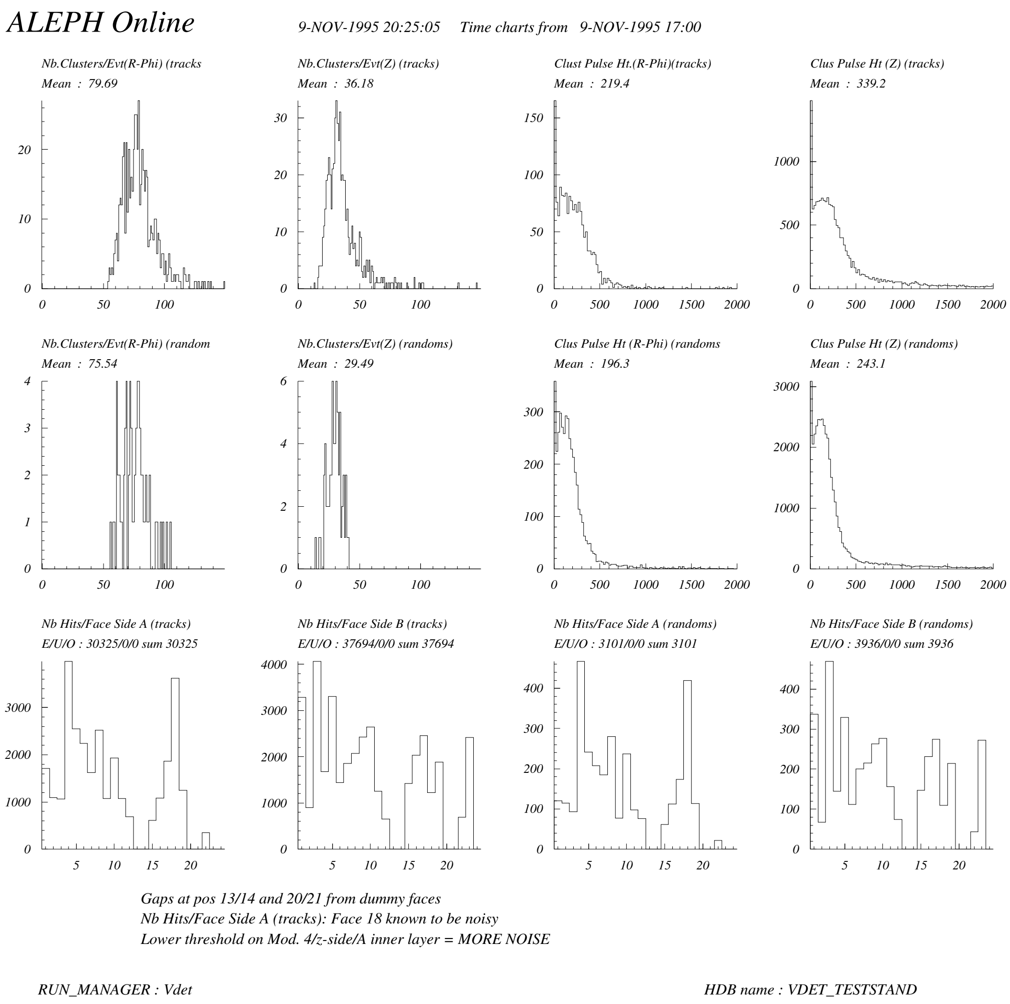

Figure A.2: *The* VDET II *shift page*

There are currently 22 expert pages defined for the VDET II detector. Basically each expert page shows the same type of distribution as in the shift page but for individual subcomponents of the detector (face, module, MX7 chip).

At the end of every run, *VDMON* creates a 'saveset' of histograms which is then analysed by VDANL.

A.4.2 VDANL

VDANL is the VDET II end-of-run analysis task. It is triggered at the end of every run by the monitoring task *VDMON* and then does simple checks, for good runs, on the histograms produced by *VDMON* which appear in the presenter.

At process initialision, *VDANL* checks the VDET II online database to see which VDET II modules are fully functioning. On the basis of this it then fills an array full of histogram identifier numbers for those which do not need to be checked. For each run, *VDANL* first checks that all the presenter histograms exist. If this is the case, *VDANL* then checks to see whether the run is good enough to be analysed. It does this by summing the number of non-zero entries in the two VDET shift page histograms which deal with the number of clusters per 'track'[3] event, in the z and $r\phi$ views. If the run contains 'track' events, *VDANL* then checks to see whether the presenter histograms are empty or not, except for those which it had decided, at initialisation, do not need checking. If some histograms are empty and there are enough 'track' events in the run, a list of all empty histogram identifiers is written to a file and an error message is sent to the error logger.

A.4.3 VDHOT

VDHOT is an ALEPH monitoring task, designed to monitor the electronic chan-

[3]A 'track' event is defined as one which is neither a random event or a TPC laser event. Before the upgrade of LEP energies, the old VDET monitoring task displayed Z^0 event histograms on its shift page but since LEP has moved away from the Z^0 resonance this is no longer as useful.

nels in VDET II and create a list of noisy, or 'hot', channels for every run.

At the start of every run, *VDHOT* creates an empty VHOT BOS bank for the run and also a VOCC occupancy bank for each readout module. There are 48 physical modules, each having 2 views (z and $r\phi$); hence there are 96 VOCC banks. Each VOCC bank has 1024 rows, one row for each electronic channel. Every time an electronic channel, which is not in overflow or flagged as 'bad' in the VPLH banks, registers a 'hit', with a pulse height greater than some minimum value, the value (initially zero) stored in the corresponding row of the corresponding VOCC bank is incremented. At the end of the run, if there were enough events, the VOCC banks are read in turn and those channels with an occupancy greater than some maximum value are declared noisy, or 'hot', and their addresses written to the VHOT bank. Finally, if there are less than 1000 'hot' channels, the VHOT bank is written out to the start of run record where it can be accessed offline.

Bibliography

[1] R.M. Barnett et al., *Phys. Rev.* **D 54**, 1 (1996).

[2] F. Halzen and A. D. Martin, 'Quarks and Leptons: An Introductory Course in Modern Particle Physics', ISBN 0-471-88741-2 (1984)

[3] D. H. Perkins,'Introduction to High Energy Physics', Addison-Wesley ISBN 0-201-12105-0 (1987).

[4] M. Neubert, Proceedings of the 1995 European School of High Energy Physics, Dubna, Russia (1995).

[5] M. Neubert, Proceedings of the 17th International Conference on lepton-photon interactions, Beijing, China (1995).

[6] A. J. Buras, *Nucl. Instr. and Meth.* **A 368** (1995) 1.

[7] D. B. Cline, Scientific American, Volume 271 Number 3, (1994).

[8] K. Chetyrkin et al., *Phys. Lett.* **B 400** (1997) 206.

[9] S. Bertolini et al., *Phys. Rev. Lett.* **59** (1987) 180.

[10] N. G. Deshpande et al., *Phys. Rev. Lett.* **59** (1987) 183.

[11] J. L. Hewett, *Phys. Rev. Lett.* **70** (1993) 1045.

[12] A. J. Buras et al., *Nucl. Phys.* **B 424** (1994) 374.

[13] A. Ali and C. Greub, *Phys. Lett.* **B 293** (1992) 226.

[14] A. Ali, DESY 97-019, (1997).

[15] M. S. Alam et al., CLEO collaboration, *Phys. Rev Lett.* **74** (1995) 2885.

[16] R. Ammar et al., CLEO collaboration, *Phys. Rev. Lett.* **71** (1993) 674.

[17] O. Adriani et al., L3 Collaboration, *Phys. Lett.* **B 317** (1993) 637.

[18] W. Adam et al., DELPHI Collaboration, *Z. Phys.* **C 72** (1996) 207.

[19] The ALEPH Collaboration, "The ALEPH Handbook volume 1", edited by C. K. Bowdery, ISBN 92-9083-072-7 (1995)

[20] The ALEPH Collaboration, "The ALEPH Handbook volume 2", edited by C. K. Bowdery, ISBN 92-9083-073-5 (1997)

[21] D. Decamp et al., *Nucl. Instr. and Meth.* **A 294** (1990) 121.

[22] D. Buskulic et al., *Nucl. Instr. and Meth.* **A 360** (1995) 481.

[23] G. Batignani et al., *IEEE Trans. Nucl. Sci.* **NS-39(4/5)** (1992) Vol. 1, p. 438.

[24] G.J. Barber et al., *Nucl. Instr. and Meth.* **A 279** (1989) 212.

[25] W.B. Atwood et al., *Nucl. Instr. and Meth.* **A 306** (1991) 446.

[26] D. Bédérède et al., *Nucl. Instr. and Meth.* **A 365** (1995) 117.

[27] J.C. Brient et al., ALEPH 93-107 (PHYSIC 93-88) (1993); A. Rougé, ALEPH 94-057.

[28] T. Sjostrand, *Comp. Phys. Commun.* **39** (1986) 347; T. Sjostrand and M. Bengtsson, *Comp. Phys. Commun.* **43** (1987) 367.

[29] J.E.Campagne and R. Zitoun, *Z. Phys.* **C 43** (1989) 469-475.

[30] R. Brun et al., CERN-DD/EE/84-1 (1987).

[31] A. Ali et al., *Phys. Lett.* **B 298** (1993) 195; Private communications with A. Ali.

[32] A. Ali and C. Greub, *Phys. Lett.* **B 259** (1991) 182

[33] Private communications with C. Greub.

[34] R. Wang, Ph.D.thesis, University of Minnesota (1994).

[35] D. Decamp et al., ALEPH Collab., *Z. Phys.* **C 48** (1992) 365-392.

[36] D. Brown and M. Frank, ALEPH 92-135 (PHYSIC 92-124) (1992).

[37] JADE colaboration, W. Bartel et al., *Z. Phys.* **C 33** (1986) 23; S. Bethke, Habilitation thesis, LBL 50-208 (1987).

[38] D. Decamp et al., ALEPH Collab., *Phys. Lett.* **B 257** (1991) 492.

[39] F. Bulos,"Resolving overlapping gammas in a modular neutrals detector", PEP report 194.

[40] D. Buskulic et al., ALEPH Collaboration, *Z. Phys.* **C 69** (1996) 365,
P. D. Acton et al., OPAL Collaboration, *Z. Phys.* **C 58** (1993) 405,
D. Buskulic et al., ALEPH Collaboration, *Z. Phys.* **C 57** (1993) 17,
P.Abreu et al., DELPHI Collaboration, *Z. Phys.* **C 69** (1996) 1,
O. Adriani et al., L3 Collaboration, *Phys. Lett.* **B 292** (1992) 472.

[41] R. Barate et al., ALEPH Collaboration, *Z. Phys.* **C 74** (1997) 451.

[42] R. Barlow and C. Beeston, Comp. Phys. Comm., 77:219 (1993).

[43] F. James, 'MINUIT', CERN program library long writeup **D506** (1994).

[44] 'Precision Calculations for the Z resonance', Eds. D. Bardin, W. Hollik and G. Passarino, Report CERN-95-03 (1995).

[45] Private communications with T. Ohl.

[46] M. Corden, forthcoming ALEPH note; C. Benchouk and K. Trabelsi, forthcoming ALEPH note.

[47] A. Wagner, ALEPH 96-143 (PHYSIC 96-131) (1996)

[48] J. L. Hewett and J. D. Wells, *Phys. Rev.* **D 55** (1997) 5549.

[49] P. Nath and R. Arnowitt, *Phys. Rev. Lett.* **74** (1995) 4592.

[50] A. Ali and C. Greub, *Phys. Lett.* **B 361** (1995) 146

[51] D.Creanza et al., ALEPH 96-42, PHYSIC 96-38, 20 (1996).

[52] B. Mours et al., *Nucl. Instrum. Meth.* **A 379** (1996) 101.

[53] ALEPH collaboration, “Proposal for a new Vertex Detector for ALEPH”, CERN/LEPC 93-8 (1993)

[54] J. Carr et al., ALEPH 94-168 (1994)

[55] M.Cattaneo et al., CHEP 92 (1992)

[56] V. Blobel, DESY R1-88-01, (1988)